Thermal Modeling of the Laser-Powder Bed Fusion Process

by

Mohammad Masoomi

A dissertation submitted to the Graduate Faculty of
Auburn University
in partial fulfillment of the
requirements for the Degree of
Doctor of Philosophy

Auburn, Alabama
August 4, 2018

Keywords: additive manufacturing, heat transfer, numerical simulation,
laser-powder bed fusion

Approved by

Scott Thompson, Chair, Associate Professor of Mechanical Engineering
Nima Shamsaei, Co-Chair, Associate Professor of Mechanical Engineering
Roy Knight, Associate Professor of Mechanical Engineering
Lorenzo Cremaschi, Associate Professor of Mechanical Engineering

Abstract

Parts fabricated using laser-based additive manufacturing (AM) methods, such as laser-powder bed fusion (L-PBF) receive very high, localized heat fluxes from a laser within a purged, shielding gas (i.e. argon) environment during manufacture. To aid the development/design of AM processes, it is important to have some form of predictive simulation capability in order to reduce trial-and-error experimentation and build iterations. In this work, a continuum-scale modeling approach is generated and employed with three-dimensional finite element analysis (FEA), for simulating the temperature response of parts during L-PBF. Additionally, using computational fluid dynamics (CFD), the local heat transfer between the adjoining shielding gas, laser-induced melt pool and surrounding heat affected zone (HAZ) is estimated. The model has been validated using experimental measurements from the literature and in-house experiments. Validated simulations have been performed for the L-PBF of stainless steel (SS) 17-4 precipitation hardened (PH) and Ti-6Al-4V parts.

Results demonstrate that the temperature response of and around the part, for constant laser power and scan speed, is dependent on part volume, substrate size and scan pattern. Since the heat transfer during L-PBF is directly coupled with encumbered part microstructural properties, the presented results demonstrate the importance of process-parameter and geometry/size-coupling. Properties of fabricated parts are not only a function of process parameters, but also of scan pattern, part volume, substrate size and intra-layer time interval.

The discretized temperature, temperature time rate of change (i.e. cooling rate) and local temperature gradient have been investigated for various scan strategies and number of lasers, i.e. one, two or four. The number of sub-regional areas of the powder bed dedicated to individual lasers, or 'islands,' was varied. The average maximum cooling rate, the average maximum temperature gradient per layer, and the spatial standard deviation, or uniformity, of such metrics are presented and their implications on microstructure characteristics and mechanical traits of Ti-6Al-4V are discussed. Results demonstrate that increasing the number of lasers will reduce production times, local cooling rates and residual stress magnitudes; however, the anisotropy of the residual stress field and microstructure may increase based on the scan strategy employed. In general, scan strategies that employ reduced track lengths oriented parallel to the part's shortest edge, with islands 'stacked' in a unit-row, prove to be most beneficial for L-PBF.

The generated model was also used to study the effects of convection on thermal response during fabrication of Ti-6Al-4V. Results indicate that by increasing the speed of argon, effects of convection become more prominent and that the convective heat flux is highest when the laser and gas are moving in the same direction. The direction of the laser scan path relative to the gas flow direction clearly impacts local convection heat transfer. Results suggest such variation can impact the prior β grain size in Ti-6Al-4V material by up to 10%. When the laser and gas are moving in the same direction, there also exists a 'leading boundary layer' that can preheat upcoming powder to reduce residual stress. Presented results can aid ongoing L-PBF modeling efforts and assist manufacturing design decisions (e.g. scan strategy, laser power, scanning speed, etc.) – especially for cases where homogeneous or controlled material traits are desired.

In order to learn how to modify AM designs and processes to ensure lab-scale specimens and final components have similar properties, it is important that process-property relationships be

established through thermal simulations. In this study, a unique numerical method for efficiently predicting the thermal history of additively manufactured parts via simulation is presented and validated. The numerical method makes use of an idealized, constant/uniform heat flux which is applied at each new layer and 'bulk-layers' which consist of several layers and allow the use of coarser meshes and longer time steps. To demonstrate and test the numerical methods, they are used to simulate the L-PBF of SS 17-4 PH parts with different volumes. Simulations indicate how to modify L-PBF process parameters, specifically time intervals, to better ensure a similar thermal history, temperature, temperature gradient and cooling rate, of different sized/shaped parts.

Finally, the effects of thermal response on mechanical properties of fabricated parts were studied. Neutron diffraction was employed to measure internal residual stresses at various locations along SS 17-4 PH specimens additively manufactured via L-PBF. Of these specimens, two were rods (diameter = 8 mm, length = 80 mm) built vertically upward and one a parallelepiped (8×80 x 9 mm^3) built with its longest edge parallel to ground. One rod and the parallelepiped were left in their as-built condition, while the other rod was heat treated. Data presented provide insight into the microstructural characteristics of typical L-PBF SS 17-4 PH specimens and their dependence on build orientation and post-processing procedures such as heat treatment. Results indicate that residual stress in parts with horizontal orientation are higher compared to parts with vertical orientation.

Acknowledgments

I would like to express my deep gratitude to my advisors, Dr. Thompson and Dr. Shamsaei. I have learned many things since I started working under their supervision. Dr. Thompson spent much time guiding me through the project and helped me to find the right path. Dr. Shamsaei's technical guidance and insight about the project was extremely helpful. Also, I am grateful to Dr. Knight, Dr. Cremaschi, and Dr. Silva for serving on my committee, and providing oversight on this dissertation.

I also need to acknowledge the Mechanical Engineering Graduate Program. Not only did I learn many new things, but also I was able to do my experiments in their facilities. During my two-year period at Auburn University, I made many friends who added color to my life. I have to acknowledge all my lab mates in the National Center for Additive Manufacturing Excellence (NCAME) for their assistance with many aspects of my research, which are too numerous to list here. In particular, I want to give special thanks to Dr. Jonathan Pegues, Mr. Arash Soltani-Tehrani, and Mr. Basil Paudel for their help in conducting experiments in support of my dissertation research.

Last but not least, I owe more than thanks to my family members including my wife, my parents and my sister, for their support and encouragement throughout my life. Without their support, it would have been impossible for me to finish my college and graduate education seamlessly.

Table of Contents

List of Tables

List of Figures

CHAPTER 1

Introduction

1.1. Additive Manufacturing

Additive manufacturing (AM) is an appealing means for generating complex-shaped, metallic components conforming to specific applications. A metallic feedstock, typically in the form of powder or wire, is processed to generate a target volume from the ground up using solid model data, directed energy, computer numerical control (CNC), and an inert or evacuated atmosphere. Many industries, ranging from aerospace to biomedical, have taken interest in employing AM for the production of application-tailored components [1,2]; however, before such parts can be used reliably, their quality and mechanical strength must be verified and assured [3–5]. By determining 'feedstock-process-property-performance' relationships inherent to a specific material/feedstock and process, such efforts can be expedited. Since the macro/microstructure of many metallic AM parts is directly coupled with the heat transfer experienced during their manufacture, process-property relationships can be elucidated by observing and quantifying part temperature and other thermal phenomena during its AM.

Powder Bed Fusion (PBF) is an AM method used for fabricating metallic (or ceramic) components via directed energy and a pre-deposited layer (or 'bed') of powder feedstock [6]. The energy source can be in the form of a focused electron beam or laser. When a laser is used as the energy source, the process is referred to as Laser-PBF (L-PBF). The localized laser irradiation results in a very high heat flux that overcomes the powder latent heat of fusion, forming a micro-

sized pool of molten material, such as the melt pool. As the laser beam moves away from the irradiated location, the melt pool solidifies very rapidly, forming a track of solid material. This process is repeated to form multiple tracks within a single layer based on a user-defined laser scan strategy. Upon finishing the build, the structure is detached from the substrate and excess powder is removed. In general, the PBF part will possess a net shape due to partially melted powder along its surface. Post-PBF, subtractive machining procedures are often employed for achieving target surface quality and tolerances.

A schematic of the L-PBF process is shown in Figure 1.1. A moving laser, melt pool, powder bed, part, substrate, and a recently solidified track are depicted, as well as all modes of local heat transfer, e.g., conduction, convection, and thermal radiation. The heat transfer process is initiated upon the selective laser irradiation of the pre-deposited powder bed. The solid region in the neighborhood of the melt pool is the heat affected zone (HAZ). A portion of the incident energy delivered from the laser, typically at constant wavelength, is absorbed and this ratio of energy, or absorptivity, depends on powder surface properties which are dictated by its phase (solid or liquid), temperature, cleanliness, oxidization, material type, shape, etc. Absorbed thermal energy is primarily used for melting the powder by overcoming its latent heat of fusion. Thermal energy not used for melting is utilized for sensible heating of the melt pool, surrounding the solidified tracks and/or powder bed [7,8]; evaporation of the melt pool can also occur [9,10]. The non-isothermal melt pool can circulate due to density and surface tension gradients [11], and local mass transfer is also possible [12]. The high heat fluxes inherent to L-PBF allow parts to experience localized, extreme temperature gradients near their HAZ and heating/cooling and solidification rates that are highly dynamic, as well as high magnitude, during their manufacture [9,10]. These temperature gradients and cooling rates can result in adverse material side effects

such as residual stress or pore/defect formation, respectively [13,14]. Due to cyclic, laser-induced conduction with previously-deposited layers and adjacent tracks, the microstructure of the part continues to evolve even after its initial solidification. Cooling rates are driven by conduction through the HAZ, as well as heat loss to the process/shielding gas and enclosure walls via convection and thermal radiation, respectively.

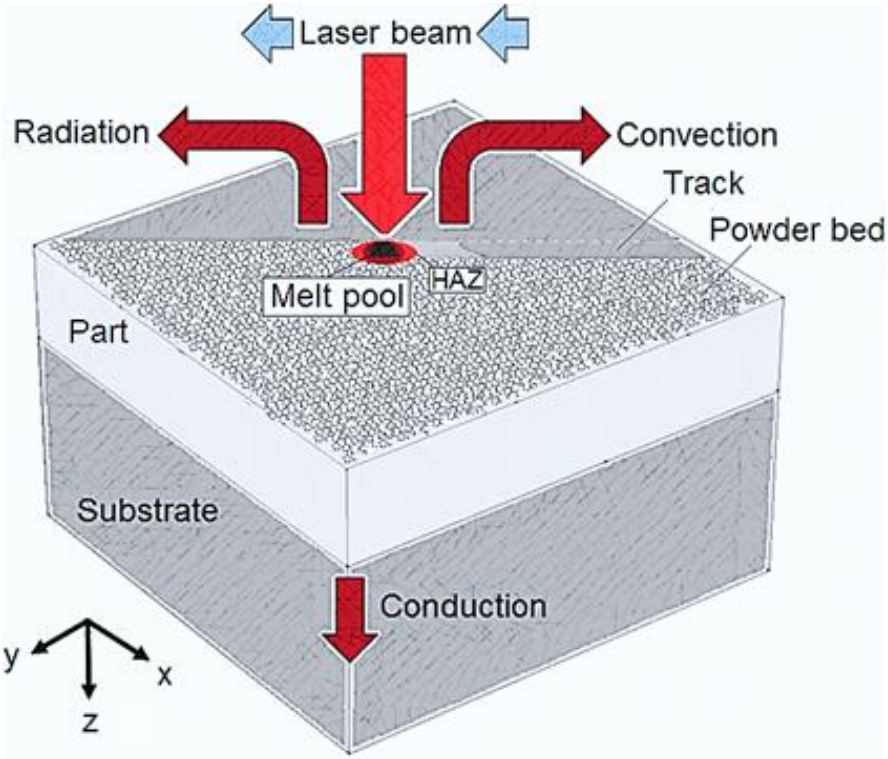

Figure 1.1 - Schematic of a typical L-PBF process consisting of a single moving laser beam, powder bed, solidified tracks, part and substrate. The modes of heat transfer in proximity to the melt pool and HAZ are shown.

Unlike traditional manufacturing methods, L-PBF provides the ability to produce parts that are more complex and/or integrated assemblies. For example, parts with functionally-graded porosity and/or embedded structures (e.g. mini-channels) can be built with less difficulty [15–17]. The ability to manufacture products on-site via L-PBF also appeals to biomedical and aerospace industries as several supply chain dependencies can be eliminated for reducing costs and turnaround times [18]. Being able to generate more conformal, customized products via L-PBF is

especially of interest to the biomedical industry. Patient/injury-specific implants can be fabricated on demand and on-site via L-PBF using materials such as Ti-6Al-4V or stainless steel (SS) 316L [16,19]. For instance, porous implants can be fabricated for more optimal, rapid patient integration by matching the stiffness of such implants to that of bone. Wauthle et al. [20] demonstrated that L-PBF is a feasible option for producing highly porous, pure Ti orthopedic implants based on the mechanical properties of the manufactured parts and the high repeatability of the process.

Inert shielding gas is employed during welding and laser-based AM processes in order to reduce oxide formation on part/powder surfaces, to protect the melt pool against outside contamination, and to aid in expelling so-called 'spatter' debris. Ly et al. [21] experimentally studied spatter generation during the L-PBF process. They showed that presence of flow of argon gas can decrease the spatter significantly compared to when the process is performed in a vacuum. Wang et al. [22] studied the effects of shielding gas during laser deep penetration welding. It was shown that the shielding gas helped stabilize the laser welding process due to heat transfer via convection enhanced ionization–recombination. Philo et al. [23] simulated the flow inside an L-PBF (Renishaw AM 250) chamber. The flow was shown to be non-uniform and it was concluded that flow non-uniformities can increase spatter generation. Kah et al. [24] experimentally studied the effects of shielding gases in the welding of metals. They discussed effects of various shielding gas on the microstructure and mechanical properties of different materials including steel, aluminum, and their alloys. It was reported that for ferritic SS, increasing the amount of carbon dioxide in shielding gases can increase the martensite content at the grain boundary. While for austenitic SS, increasing the amount of nitrogen in the shielding gas increases the ductility and improves the tensile strength, hardness, and pitting corrosion resistance of the weld [24]. The

mechanism behind these changes is not known and more modelling needs to be done in order to reveal it.

1.2. Effects of Process Parameters on Manufactured Parts

Many free L-PBF (and PBF in general) process parameters exist, including laser power, laser heating area, scan speed, inter-layer time interval, and hatching distance. There are also free design parameters, such as type of material, laser scanning pattern, build orientation, powder size, powder distribution, etc. Utilization of various process/design parameter combinations results in a part that is possessing a unique spatiotemporal temperature field, or thermal history, during fabrication. Since thermal history directly affects the microstructure, residual stress and pore/defect distribution within L-PBF parts, its quantification allows one to better select process/design parameters for a desired quality tolerance and microstructure. This is the motive for understanding process-property relationships inherent to L-PBF.

If an operator aims to minimize the variation in PBF process parameters throughout a build, quality control is perhaps easiest achieved by strategically determining optimal scan patterns a priori, such that adverse thermal effects associated with part size, geometry, and complexity are minimized. Such scan patterns are at the full discretion of the part designer/manufacturer and implementable on a per-layer basis. A part layer can be built on a sub-regional basis, each with a dedicated scan path, in a specific sequence; or the entire layer can be built using a single scan path that 'sweeps' across the layer in a single direction. Each sub-region, or 'island,' can possess its own laser scan sweep direction. Many possible options exist for island division per layer and path strategy per island, as well as for the island formation sequence per layer (i.e., the order in which islands are solidified). Recent work has demonstrated that island scan strategies are effective in reducing residual stress within PBF parts [25,26].

Due to the locality and speed of fusion during L-PBF, residual stress formation within the fabricated materials can be high. Various residual stress distributions within the part can lead to delamination [27], as well as observable geometric intolerances, such as bowing or warping [28]. The HAZ temperature field conducive to residual stress formation is typically characterized by highly-localized spatial variation in temperature, i.e., temperature gradients in HAZ, and/or the rapid temperature time rates of change. For PBF [28–32] residual stress can be mitigated via proper support structuring at the part/substrate interface and/or assigning more appropriate laser scan directions per layer; appropriate scan planning also has been found to mitigate residual stress in parts fabricated via Directed Energy Deposition (DED) methods [33]. Parry et al. demonstrated via thermo-mechanical simulation that residual stresses in PBF parts are anisotropic due to non-uniform thermal history and they typically increase with longer tracks [31]. Hussein et al. [34] numerically demonstrated, for the L-PBF of SS 316L, that temperature gradients are highest at the beginning of each track and subsequently decrease along the track length. Nickel et al. [35] and Cheng et al. [36] demonstrated, via simulation of the PBF process, that the use of islands with scan paths that vary in direction for each new layer (i.e., rotating directions) can result in parts possessing more uniform residual stress distributions.

Kruth et al. [37] experimentally studied the effects of scan direction on part temperature gradients during L-PBF of Ti-6Al-4V. Shorter scan vectors, or tracks, were found to result in the part experiencing smaller temperature gradients and thermal stress. It was also found that preheating the substrate generally reduces intra-part temperature gradients during manufacture. In another study, Kruth et al. [38] fabricated parts with dimensions of 35×15 mm^2 from iron-based powder via four different scan patterns. Two patterns consisted of the laser moving along the regular X and Y directions; the other two scan patterns employed 21 islands, each 5×5 mm^2, or

42 islands, each 2.5 × 2.5 mm^2. The results suggested that samples fabricated using an island-based scan strategy deformed less relative to samples fabricated with no sub-regions/islands (i.e., one 'island'). Nickel et al. [35] made similar conclusions via finite element methods (FEM) and numerical simulation.

Thijs et al. [39] studied the effects of scan strategies on the microstructure of AlSi10Mg and found that part texture can be controlled by rotating the scanning direction 90º between neighboring islands for a given layer. Lu et al. [40] built 10 × 10 × 10 mm^3 Inconel 718 parts using L-PBF while employing an island-based scan strategy consisting of various island sizes. It was found that scan strategies employing larger islands resulted in parts having higher density, while microstructure, ultimate tensile strength, and yield strength demonstrated only a slight dependence on the number of islands employed. The residual stress within the part was found to increase with island size. Bo et al. [41] studied the effects of swirl/helix-type scan patterns on the mechanical response of SS 316L parts during L-PBF. Parts fabricated using this scan pattern were found to possess a relatively rougher surface consisting of ravines between tracks. Part dimensional accuracy was also found to be less relative to parts fabricated using unidirectional scan patterns. Li et al. [28] demonstrated that part distortion in the laser scan direction is lowest relative to other directions, and that using island scan strategies can result in decreased deformation of the final part. Bending of the part away from the substrate, in the height-wise direction, was also reported as the most prevalent form of distortion for the unidirectional scan strategies investigated.

Use of L-PBF for processing Ti-6Al-4V has been demonstrated extensively. Parts made from Ti-6Al-4V alloy typically possess acceptable mechanical properties and corrosion resistance [42] making them appealing for use in biomedical, chemical, marine and industrial applications. Thijs et al. [43] experimentally investigated the microstructure evolution of Ti-6Al-4V during L-

PBF. It was found that the inherently fast cooling rates can result in the formation of the martensitic phase in the material. Additionally, it was observed that the direction of elongated grains depends on scan strategy. Qiu et al. [44] experimentally investigated the effects of process parameters on the porosity of Ti-6Al-4V parts fabricated via L-PBF. It was observed that melt pool flow dynamics can affect pore formation in parts. Masoomi et al. [45] investigated the effects of scan strategies and number of lasers used during L-PBF on the thermal response of Ti-6Al-4V parts – including local temperature, temperature gradients and temperature time rates of change. It was shown that by using multiple lasers and the appropriate island scan strategies, the temperature gradients and cooling rates can decrease.

SS 17-4 precipitation hardened (PH) consists of good mechanical properties and corrosion resistance. These properties make it good candidate for use in marine environment, power plants and chemical industries [46]. LeBrun et al. [47] investigated the mechanical properties of bulk materials of SS 17-4 PH produced by L-PBF. Effects of additional thermal processing was investigated too. L-PBF is capable of producing refined microstructure, which result in parts with higher tensile strength. The heat treatment enhances the strength of the parts. Facchini et al. [48] observed that microstructure of SS 17-4 PH parts made by L-PBF, are composed of metastable austenite or mixtures of austenite (fcc, a=0.357 nm) and martensite (bcc α-ferrite (Fe), a=0.286 nm). Murr et al. [49] reported that changing gas inside the chamber from argon to nitrogen would result in different microstructure for the fabricated parts.

Yadollahi et al. [50] investigated the effects of building orientation on the volume fraction of martensite and retained austenite phases of SS 17-4 PH fabricated via L-PBF. Based on the experimental results, they reported that horizontal samples have higher amount of retained austenite compared to vertical counterparts due to these parts experiencing higher cooling rates.

Mahmoudi et al. [51] studied the effects of inter-layer time intervals on mechanical properties and microstructural features of SS 17-4 PH fabricated via L-PBF. The experimental results indicated that changing the inter-layer time interval (from 10 s to 50 s) has insignificant effects on yield strength and elongation to failure on parts. This indicates that inter-layer time intervals have only a slight effect on the thermal history of the fabricated parts. Huang et al. [52] studied the effects of track length on the thermal response of the part. They concluded that shorter tracks tend to have higher temperature and lower thermal gradient. That would improve wetting condition and result in denser parts.

1.3. Simulation of the Additive Manufacturing Process

The L-PBF process may be numerically modeled and simulated using FE methods [53–56]. Such approaches have been performed with varying degrees of fidelity for learning process-structure-property relationships while minimizing the need for repetitious, costly experimentation. In general, a continuum or powder-scale approach can be utilized, with the latter requiring significantly more computational resources. In powder-scale approaches [11,57], thermofluidic phenomena, such as melt pool fluid dynamics, melt pool wetting/spreading/wicking, powder distribution/size effects, solidification, and microstructural-coupling can be more accurately modeled, as the L-PBF process is better represented. However, in many cases, such effects can be secondary or tertiary in nature relative to the impactful phenomena driven by the bulk temperature response (e.g., cooling rates, temperature gradients, peak temperatures, etc.) of the participating media (e.g., powder, part, and substrate). In these cases, participating media can be modeled as continua, and the effects of powder bed porosity can be indirectly accounted for through use of effective bulk properties. In order to model powder melting and melt pool solidification during L-PBF, the latent thermal energy transfer can be idealized and/or incorporated into the model.

There are two common FE methods that may be used for modeling the continuum scale heat transfer inherent to the additive manufacture of a part, in which mass addition occurs: the quiet or inactive methods [58,59]. In both cases, the governing equations for energy transport and mass conservation are solved via spatial/temporal discretization and accomplished by meshing media in which the solution is sought. For the quiet method, all elements are available throughout simulation. However, they are assigned specific properties, so they do not affect the solution in real time. For inactive methods, each element is activated only when needed. Michaleris et al. [55] investigated the accuracy of both methods and demonstrated they each provide for similar results (less than 0.5% difference). However, the computational time investment for the inactive method is longer than that for the quiet method.

Dong et al. [60] used the FE method to study the effects of phase transformation as well as to determine the influence of scanning speed, laser intensity, and beam spot diameter on Selective Laser Sintering (SLS) parts during manufacturing. They predicted a linear relationship between laser power and maximum temperature. They showed that reducing laser beam diameter, reducing scan speed, and increasing preheating temperature would result in higher heat diffusion in the powder bed. Riedlbauer et al. [54] investigated the melt pool temperature profile and its size by using a nonlinear FE method. They showed that increasing the laser power or decreasing the scanning velocity increased the width and depth of the molten pool. Mukherjee et al. [61] studied the role of a non-dimensional heat input number, the Peclet number, the Marangoni number, and the Fourier number on temperature and velocity distribution, cooling rate, solidification parameters, hardness, amount of porosity, size of intermetallic compounds, and thermal distortion. They concluded that a higher heat input will increase the peak temperature and melt pool

dimension while decreasing the cooling rate. They showed high Marangoni numbers will result in an improved interlayer bonding.

Since the typical PBF process employs a relatively small directed energy area, powder size, and layer thickness, and due to the fact that many PBF machines take time to deposit/remove powder for each new layer ('coating' procedure and post-fusion clean-up), today's PBF process can take multiple hours to complete [62], and this provides a challenge to manufacturers targeting fast production rates. Further, in a typical PBF process, each new powder layer is 'over-sized' and spans the entire width and length of the chamber, and this can add significant time to production of small-sized parts. Hence, in order for the PBF process to be more attractive for high volume production, in terms of both component size and quantity, it is of interest to decrease the time associated with part manufacture. One solution is to employ multiple directed energy sources, such that the cross-sectional geometry of the part can be divided into islands each possessing their own dedicated directed energy source. In this way, parts can be fabricated by densifying multiple islands in parallel, with each island having its own scan strategy and build sequence. The directed energy source can be split (diffracted) or multiple energy sources [45,63–65] can be utilized. A potential challenge for multi-laser PBF (ML-PBF) lies in the fact that using multiple islands may impact the quality of manufactured parts. As shown for single-laser PBF, such island strategies can introduce porous/unmelted regions concentrated between islands [40,66]. In addition, the effective scan strategies for ML-PBF, and the degree in which such strategies deviate from those used for single-laser PBF, have not been clearly identified.

In order to produce realistic boundary conditions for performing more accurate laser-based AM simulations, the convection and radiation heat transfer modes should be rightfully considered along the surfaces of as-manufactured parts and surrounding powder. As part sizes and/or number

increase within L-PBF chambers, and as AM systems seek to produce parts faster, the bulk temperature of the chamber-enclosed assembly will increase, therefore making heat transfer from the HAZ and melt pool to the adjoining gas (which is typically at constant inlet temperature) more significant. However, there is little consensus in the literature on how to take these into account. Radiation and convection are assumed to be negligible during L-PBF in some studies [67–69]. Others have assigned a heat transfer coefficient over all free surfaces. Peyre et al. [70] used constant heat transfer coefficient, 20 $W/m^{2}\cdot{}^{o}C$, Dong et al. [60] used 25 $W/m^{2}\cdot{}^{o}C$, Espana et al. [71] used 10 $W/m^{2}\cdot{}^{o}C$, Denlinger et al. [8] and Parry et al. [31] used 15 $W/m^{2}\cdot{}^{o}C$. Michaleris [55] assumed free convection around the powder bed and forced convection around the HAZ. In their study, the heat transfer coefficient was considered 10 $W/m^{2}\cdot{}^{o}C$ and 21 $W/m^{2}\cdot{}^{o}C$, respectively. It was concluded that neglecting the effects of convection and radiation will result in over-predicting the temperature. Zekovic et al. [72] modeled the convection around the melt pool using computational fluid dynamics (CFD) for Direct Laser Metal Deposited (DMD) of H13 tool steel. Additionally, Heigel et al. [33] modeled convection using a measurement-based method for DMD of Ti-6Al-4V. They showed that using a more accurate heat transfer coefficient will reduce the error in predicting the temperature by up to 30%. It was shown in the study that either using free or forced convection will result in over-prediction of the temperature. Finally, Bannour et al. [73] numerically modeled the effects of shielding gas velocity on maximum temperature of the melt pool during continuous laser welding of AZ91 magnesium alloy. It was shown that by increasing the velocity of the shielding gas, maximum temperature of the melt pool will decrease.

A major challenge in simulating the AM process is developing an efficient model that can produce information and knowledge at the overall scale of the desired part and build-process to inform engineering decisions [74,75]. Quantities of interest at the part scale include: distortions

that can halt machine operation or place the completed part outside the desired geometric envelope; residual stresses that can create initial conditions detrimental to service-life concerns such as failure and fatigue; and local effective material properties, or at least indicators of where they might significantly deviate from the nominal properties expected from the process. There can be kilometers of laser travel length and thousands of powder layers in a single build, thus presenting a computational challenge. To be useful, part-scale simulations must be executable in a reasonable amount of time while retaining sufficient physical fidelity as to yield trustworthy results. An eventual goal is to have process models that are so efficient they could be included as part of an automated process optimization. Moran et al. [76] used a superposition-based approach to simplify and expedite the simulation process. By modeling a single track and using data from that line and applying it as a line heat source for each track, the simulation time decreased by an order-of-a-magnitude.

At the part scale, one neglects the details of local laser-powder interaction. Instead, the goal is to describe part thermomechanical behavior both during and after the build is complete. In this approximation, the powder can be represented as a reduced-density, low-strength solid. The deposition of the laser energy into the powder can then be represented by a volumetric energy source term such as that derived by Gusarov et al. [77]. Melting can be represented thermally through a latent heat parameter and mechanically as a near-total loss of strength. The “mushy zone” at the melt pool boundary can be represented by having its temperature-dependent strength rise as temperature falls below the solidus temperature.

Monitoring AM processes using thermal sensors allows one to validate and benchmark numerical models by providing actual spatiotemporal temperature field measurements of media within the process chamber. Thermocouples provide a means to measure temperature response

with high temporal resolution at specific points and have successfully been used for measuring and recording temperature responses during methods such as SLS and Laser Engineered Net Shaping (LENS) [71,78–80]. Shishkovsky et al. [81] measured the temperature response around the melting area during the fabrication of metal-polymer, intermetallic and ceramic materials using five thermocouples (temperature range 400-2800 ºC). Taylor [82] proposed a model to predict the effective thermal conductivity and absorptivity of a sintering surface and benchmarked the model with experimental data obtained via thermocouples exposed to either air or argon atmospheres. Griffith et al. [80] have reported meaningful temperature responses as provided via thermocouples even after 42 layers of deposition during LENS. In these experiments, the thermocouple bead was exposed while atop the substrate and the deposition occurred above and around it. Results of these studies indicate that, due to fast solidification process of the melt pool (which happens in milliseconds); it is hard to monitor its temperature by thermocouples alone. However, knowledge of the temperature distribution outside the melt pool area allows one to better understand the microstructure evolution and to obtain relevant data for validating numerical simulations.

1.4. Novelty of Work

L-PBF offers numbers of benefits over traditional manufacturing techniques; however, it also brings new difficulties that must be overcome to master the process. Parts fabricated via L-PBF experience high cooling rates and temperature gradients, and this will adversely affect their microstructure and residual stress, respectively. Additionally, fabricated parts can have many pores and defects which cause delamination and failures during mechanical loading. Numerical simulation tools can help engineers design and fabricate better parts. Although there are some efforts that have laid the foundation for developing tools that can simulate the L-PBF process

[55,83], there are still many aspects of AM that have not received enough attention. The main challenge is the complexity of the L-PBF process. Although welding and L-PBF have similarities, L-PBF brings unique challenges that make it extremely difficult to simulate. Additionally, L-PBF continues to be adopted by different industries including aerospace, automotive, and biomedical [84,85], and makes the need for software capable of helping researchers and engineers to design and fabricate better parts more urgent. This work has aimed at formalizing and understanding the physical problem with governing equations and scale idealization.

This study aims to elucidate relationships between scan strategies and mechanical properties of Ti-6Al-4V for both single and multi-laser PBF for aiding process and product design decisions. Although the use of multiple lasers during welding and cladding has been investigated [62,86–89], the effects of ML-PBF on material properties and residual stress still needs attention.

Since determination of the appropriate scan strategy for ML-PBF can be challenging, as more free design/process variables are introduced, the problem herein is reduced to synchronous, orthogonal multi-laser scan strategies. The ML-PBF process is modeled and then simulated for various scan strategies as to determine effects of laser number, scan pattern, and part size on the spatiotemporal temperature distribution of Ti–6Al–4V material during its first few layers of densification. A titanium alloy is selected for demonstration purposes only, while the model is applicable to various other materials. Ti-6Al-4V has commercial appeal in various industries, including chemical [90] and biomedical [91], and its microstructure is relatively sensitive to cooling rate [92], allowing it to be a suitable material for consideration herein.

Additionally, this study focuses on modeling the thermal response of a single track during typical L-PBF conditions while considering convection heat transfer with the inert shielding gas. The gas momentum and energy fields are found numerically while referencing temperature-

dependent properties. Effects of convection and radiation heat transfer, gas flow speed, and scan-to-gas-flow direction on the temperature distribution, temperature gradient, and local heating/cooling rates of Ti-6Al-4V during L-PBF for various cases are investigated. The difference between simulating L-PBF with an assumed constant heat transfer coefficient versus locally-variable heat transfer coefficients, found via CFD of surrounding fluid flow in the chamber, are also elucidated.

To expedite the simulation process and gain the ability to perform simulation on large-scale parts, new techniques are proposed herein. Bundles of layers are combined prior to simulating layer-wise AM in which an effective, uniform heat flux is employed. The goal is to decrease the total number of layers simulated for large-scale parts, thus reducing computational demand and time investment. The methods herein can aid research into AM process/design offsetting to ensure lab-scale specimens and real-life components have similar thermal histories. Numerical results are compared to experimental findings from the literature.

Finally, the effects of thermal response on microstructure and the mechanical response of fabricated parts are investigated. Experiments are performed to demonstrate and validate the effects of scan-direction-dependent convection heat transfer on the microstructure of Ti-6Al-4V. Effects of geometry on residual stress are presented by conducting unique experiments via neutron diffraction.

CHAPTER 2

Physical Model

2.1. Introduction

The transient heat transfer during the L-PBF of metals is complex; exhibiting dense heat flux transport, inhomogeneous phase change, short length/time scales, melt pool instability, surface/fluid interaction, microstructural coupling, anisotropic microstructural growth and more [3,93]. Utilizing a physical model that reduces this complexity can be advantageous for minimizing computational investment and for providing general insight into the process-property relationships inherent to parts fabricated via PBF. One such approach is to model the heat diffusion in all participating media while neglecting, or creatively accounting for, secondary/tertiary effects such as melt pool flow dynamics, powder bed mechanics, powder heterogeneity and microstructural evolution (i.e. solid-phase transformations). Then, the melt pool, powder bed and solidified part may be represented as continua with effective density and transport properties, and this approach is adopted herein.

As shown in Figure 1.1, all modes of heat transfer, i.e. conduction, convection and thermal radiation are present during L-PBF. For modeling purposes, melt pool convection and phase-change can be accounted for by employing an effective melt pool thermal conductivity and by estimating the latent heat transfer due to melting. More advanced solidification phenomena such as solid-phase nucleation, liquid-solid wetting behavior, pore generation, and more, can be

neglected while understanding that the predicted temperature response is only an estimation. Such temperature response provides insight to the process-property relationships for that given material.

In this section, For the sake of mathematical formulation, and in an attempt to formalize scan planning, a simplified ML-PBF process is described. This particular process involves the manufacture of a rectangular part with uniform cross-sectional area and single material type; fabricated using P identical lasers (i.e. same wavelength, intensity profile, etc.), each operating at the same scan speed and power. Each laser may have its own scan strategy and, any group of lasers are assumed to not intersect, operate synchronously (i.e. starting and ending at the same time) and have time-invariant power and scan speeds. Consistent with literature to date, the region of the powder bed dedicated to a single laser scan pattern is referred to as an 'island', J. Islands are constrained to have rectangular shapes distributed along a layer uniformly.

Each layer consists of $J \geq 1$ identical islands, and each island may consist of $K \geq 1$ identical sub-islands built sequentially by each island-dedicated laser. An island is defined as a sub-region dedicated to a single laser, while a sub-island is defined as a sub-region within an island dedicated to the same laser; hence, $P = J$ herein. The number of sub-islands per island follows the rule: $K \geq J$ and the number of sub-islands for each island is assumed constant. Sub-islands may consist of sub-islands, and so forth, indefinitely; however, these scenarios are not examined in this study. One may quantify the 'order' of island division on a per layer basis using a 'level of island planning' (LIP) metric which describes the number of lasers and the parallelism of island building. A LIP of zero order, i.e. LIP-0, indicates that the entire powder bed functions as a single island and that a single laser is used (i.e. $J = K = 1$), a LIP-1 indicates sequenced, sub-island scanning for a single laser (i.e. $J = 1$, $K > 1$), a LIP-2 indicates 'all at once' ML-PBF, in which a layer is divided into separate islands with 1 sub-island per island (i.e. $J > 1$, $K = 1$), finally, a LIP-3 indicates that

the powder layer is divided into islands that consist of sub-islands, to be built in a prescribed sequence, per island (i.e. $J > 1$, $K > 1$). An individual layer may be fabricated on an island-by-island basis with a single laser, i.e. in-series island building corresponding to LIP-1 (single laser) or LIP-3 (multi-laser), or with all islands built at once, i.e. in-parallel island building, corresponding to LIP-0 (single laser) or LIP-2 (multi-laser). An aerial view of the ML-PBF domain, for an arbitrary case of $P = J = K = 4$, is shown schematically in Figure 2.1.

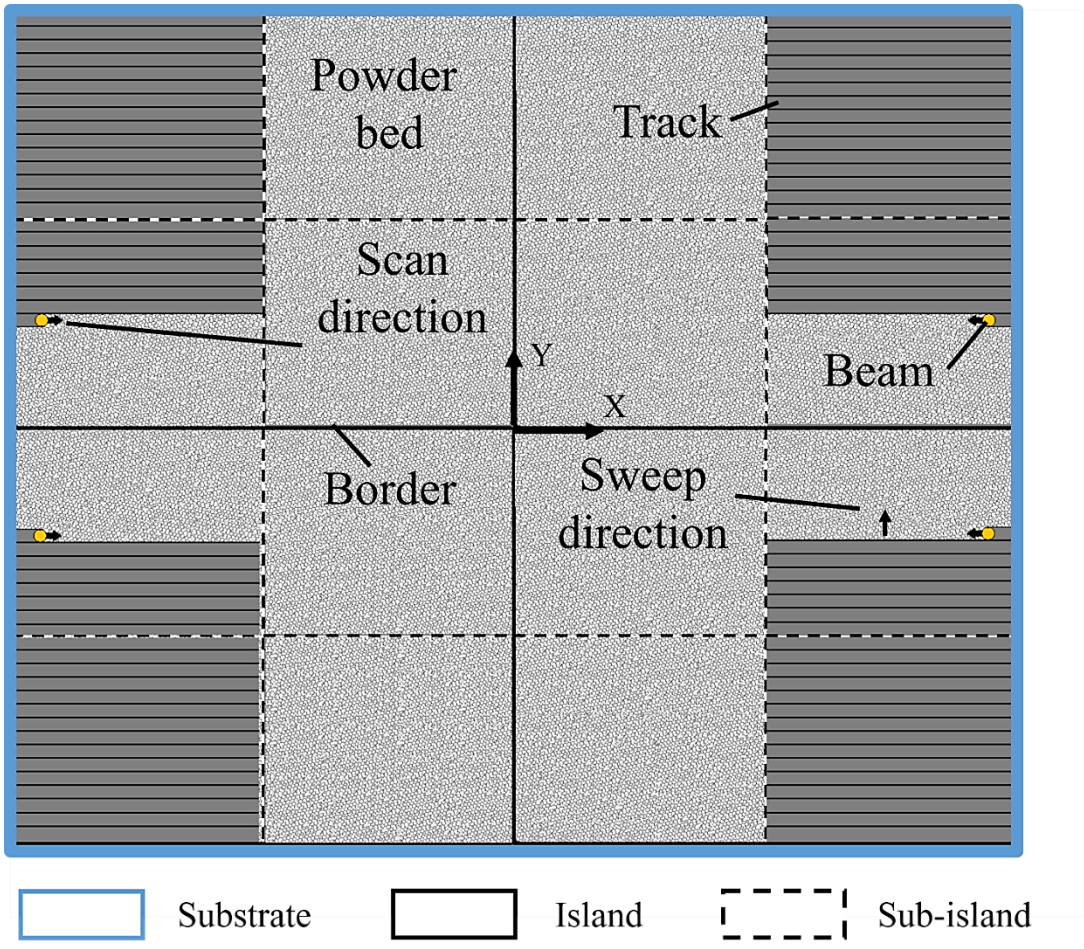

Figure 2.1 - Aerial view of a LIP-3 ML-PBF process for building a single part atop a powder bed while employing a scan strategy involving four islands ($J = 4$), 4 sub-islands per island ($K = 16$) and four synchronized lasers ($P = 4$). The island/sub-island borders and track scan/sweep directions are also shown.

The LIP for each layer of powder requires a description of the island division scheme (IDS), which provides how sub-islands and islands are divided. One can impose an IDS with the aid of

island border lines as shown in Figure 2.1. Herein, these border lines are constrained to be collinear with the edges of the part. In addition, a uniform IDS is employed such that all islands (and sub-islands) have identical area. The number of lasers used per layer does not necessarily have to equal the number of lasers available; hence, in general, each laser must be assigned specific islands for each new layer. For instance, a laser may have a different angle-of-attack, intensity and/or wavelength more desirable for a given island in some cases. The laser assignment per layer follows a matrix $\boldsymbol{J}_{\mathrm{P}}$ where each island is labeled.

Each sub-island, consisting of $N \geq 1$ tracks, consists of a scan plan that dictates laser motion during its fabrication. If the rectangular part consists of M, equal-LIP layers of height, Δl, then the final part consists of M x J x K x N total tracks. Herein, scan plans are constrained to form tracks collinear with the width (x) and/or length (y) of the layer. Note that the general direction in which tracks are added (i.e. perpendicular to tracks) is referred herein as the track sweep direction. For in-series PBF, i.e. LIP-1 and LIP-3, the sub-island sequence or order must be specified. The employed L-PBF/ML-PBF process then consists of a per-layer build plan consisting of the: LIP, IDS, laser-to-island assignments and sub-island scan plans.

2.2. Material Processing and Heat Transfer

Absolute temperature, $\mathrm{T_i}$, within bounded i^{th} continuum region, which may be the solid phase (part), liquid phase, mixed solute phase (i.e. mushy zone), or powder bed, abides conservation of energy for a given time, t_0, i.e. Eq. (2.1), during the selective laser irradiation of arbitrary layer M, i.e.:

$$\rho c_{\mathrm{i}}(\mathrm{T_i})|_{t_{\mathrm{o}}-\Delta t} \left.\frac{\partial \mathrm{T_i}(x,y,z,t)}{\partial t}\right|_{t_{\mathrm{o}}} = \nabla k_{\mathrm{i}}(\mathrm{T_i})|_{t_{\mathrm{o}}-\Delta t} \nabla \mathrm{T_i}(x,y,z,t)\big|_{t_{\mathrm{o}}} \tag{2.1}$$

where c_i is specific heat capacity and k_i is continuum thermal conductivity. The continua distribution/phase during L-PBF is coupled with the unknown temperature field; therefore, it is evaluated at a previous time, t_0-Δt, and updated based on local temperature, T_i. Temperature gradients at the boundaries of each continuum region are assumed differentiable. The x-z and y-z planes of island borders in contact with the edge of the build chamber are assumed insulated, while interior island borders are assumed to have zero interfacial thermal resistance. Note that the process of adding more powder to the PBF build chamber results in elapsed time, Δt_M, between the final sinter(s) on layer M-1 and the start of laser scanning on layer M.

The rate of energy delivered by the laser ensemble is used for either quickly overcoming the latent heat of fusion of powder for melting, q_{melt}, or is transferred via conduction through the melt pool, $\boldsymbol{q}_{mp}$, gas-entrapped powder, $\boldsymbol{q}_{pb}$, or non-powder solid material (i.e. built part), $\boldsymbol{q}_s$. Heat exchange also occurs with the surroundings via thermal radiation, $q_{rad,net}$, and/or convection, $q_{conv,net}$. Thermal radiation between melt pools and neighboring islands is neglected. For a given time and control surface atop an arbitrary layer, M, atop the J^{th} island, the energy balance can be represented as:

$$q_j - q_{melt} = \|\boldsymbol{q}_{pb}\| + \|\boldsymbol{q}_s\| + \|\boldsymbol{q}_{mp}\| + q_{conv,net} + q_{rad,net} \tag{2.2}$$

where q_j is the island surface heat flux due to laser irradiation. With respect to a growing control volume, $V_t(t)$, that encapsulates the entire part and powder bed, and by accounting for the phase change heat transfer within the melt pool via an effective specific thermal capacitance, the heat exchange between the total volume and surroundings is conserved following:

$$\iint_{A_{c,pb}} \left(Pq_j - q_{conv,net} - q_{rad,net}\right) dA_{c,pb} \cong \iiint_{V_t(t)} \rho_i(T_i) c_i(T_i) \frac{\partial T_i(x,y,z,t)}{\partial t} dV_t(t) \tag{2.3}$$

where $A_{c,pb}$ is the initial, exposed cross-sectional area of the powder bed.

The laser position relative to the imposed coordinate system, (x, y), as dictated by the scan strategy/path assigned to each island, $X_J(t)$, results in a temporal heat flux distribution at the exposed boundary of each island. The laser power absorbed the melt pool and surrounding powder is assumed to have a Gaussian intensity profile. As a result, each laser-sourced heat flux penetrates through the melt pool and powder bed following:

$$\mathrm{q}_{laser}\left(X_j(t), z\right) \cong \alpha_\lambda \frac{2P}{\pi R^2} \exp\left(-\frac{2[(x-x_c)^2 + (y-y_c)^2]}{R^2}\right) \mathrm{I}(z) \tag{2.4}$$

where α_λ is the hemispherical, spectral (at λ = 1040 nm) absorptance of the irradiated, two-phase powder bed region, R is the effective laser beam radius at which intensity reduces to the constant $1/e^2$, and (x_c, y_c) is the laser spot center location [53]. The absorptance corresponding to irradiation of the melt pool is assumed to be temperature independent and near-equal to that of the solid part and powder during the heating and cooling processes [94,95], i.e.: $\alpha_\lambda \cong \alpha_{pb} \cong \alpha_{mp} \cong \alpha_s$. Laser energy is assumed to transmit through the melt pool and adjoining powder via Beer-Lambert attenuation [96], I(z), i.e.:

$$\mathrm{I}(z) = \exp(-\tau_\lambda(z + M\Delta l)) \tag{2.5}$$

where τ_λ is the absorption coefficient of the irradiated region.

During L-PBF, temperature variation within the powder bed and part drives conduction of local magnitude and direction through various continua. Due to the ultra-high heat flux delivered by each laser, significant temperature gradients exist due to thermal spreading resistance [97] in vicinity of the superheated melt pool, i.e. within the powder bed, previous layers, neighboring tracks and substrate. Via Fourier's law, these temperature gradients, combined with an effective thermal conductivity, define a local heat flux vector within the powder bed, $\boldsymbol{q}_{pb,i}$, superheated melt pool, $\boldsymbol{q}_{mp,i}$, and surrounding (non-powder) solid media, $\boldsymbol{q}_{s,i}$, i.e.:

$$\boldsymbol{q}_{\mathrm{pb,i}} = -k_{\mathrm{pb}}\big|_{T_{\mathrm{pb,i}}} \nabla T_{\mathrm{pb}} \tag{2.6}$$

$$\boldsymbol{q}_{\mathrm{mp,i}} = -k_{\mathrm{mp}}\big|_{T_{\mathrm{mp,i}}} \nabla T_{\mathrm{mp}} \tag{2.7}$$

$$\boldsymbol{q}_{\mathrm{s,i}} = -k_{\mathrm{s}}|_{T_{\mathrm{s,i}}} \nabla T_{\mathrm{s}} \tag{2.8}$$

The effective thermal conductivity of the powder bed, k_{pb}, is calculated for a given $T_{\mathrm{pb,i}}$ using [98]:

$$\frac{k_{\mathrm{pb}}}{k_{\mathrm{g}}} = \left(1 - \sqrt{1-\phi}\right)\left(1 + \frac{\phi k_{\mathrm{r}}}{k_{\mathrm{g}}}\right) + \sqrt{1-\phi}\left\{\frac{2}{1-\frac{k_{\mathrm{g}}}{k_{\mathrm{s}}}}\left[\frac{1}{1-\frac{k_{\mathrm{g}}}{k_{\mathrm{s}}}}\ln\left(\frac{k_{\mathrm{s}}}{k_{\mathrm{g}}}\right) - 1\right] + \frac{k_{\mathrm{r}}}{k_{\mathrm{g}}}\right\} \tag{2.9}$$

where k_{g} is the thermal conductivity of the entrapped gas (e.g. argon), and ϕ is the porosity of the powder bed, i.e.:

$$\phi = \frac{\rho_{\mathrm{s}} - \rho_{\mathrm{p}}}{\rho_{\mathrm{s}}} \tag{2.10}$$

The effective thermal conductivity of the irradiated powder, k_{r}, which depends on thermal radiation exchange between neighboring powder particles and the powder distribution/size [98], is found using:

$$k_{\mathrm{r}}|_{\mathrm{T}_{i,o}} = 4F_0\sigma \mathrm{T}_{i,o}^3 d_{\mathrm{p}} = \frac{4\varepsilon\sigma \mathrm{T}_{i,o}^3 d_{\mathrm{p}}}{1 - 0.132\varepsilon} \tag{2.11}$$

where F_{o} is the radiation view factor, σ is the Stefan-Boltzmann constant, d_{p} is the mean powder diameter and ε is the constant emissivity for a typical, spherical powder arrangement [98]. The effective thermal conductivity of the melt pool, k_{mp}, is estimated using:

$$k_{\mathrm{mp}}\big|_{\mathrm{T_{mp,i}}} = (1-\theta)k_{\mathrm{l,eff}} + \theta k_{\mathrm{s}}|_{\mathrm{T_{mp,i}}} \tag{2.12}$$

where θ is the solid-phase volume fraction during melt pool formation; varying between 0 and 1, i.e.:

$$\theta = \frac{V_{\mathrm{s}}}{V_{\mathrm{s}} + V_{\mathrm{l}}} = \frac{V_{\mathrm{s}}}{V_{\mathrm{mp}}} \tag{2.13}$$

and $k_{\mathrm{l,eff}}$ is an effective, temperature-independent liquid thermal conductivity that accounts for heat transfer due to Marangoni and natural convection within the superheated melt pool [99,100]. Evaporation heat transfer within the melt pool is neglected herein.

Each continuum is assigned its own temperature-dependent specific thermal capacitance, c_{i}, relating heat flux to temperature rise. For the case of the melt pool, which is a mixed-phase alloy, an effective specific thermal capacitance, $c_{\mathrm{mp,eff}}$, is defined for relating heat flux to both temperature rise and phase change. The effective melt pool specific thermal capacitance considers melt pool regions exceeding sintering temperature, T_{s}, and below melting temperature, T_{m}, found using:

$$\rho_{\mathrm{mp}} c_{\mathrm{mp,eff}}\big|_{\mathrm{T_{mp,i}}} = [(1-\theta)\rho_{\mathrm{l}}\, c_{\mathrm{l}} + \theta\rho_{\mathrm{s}} c_{\mathrm{s}}\,] + \rho_{\mathrm{mp}}\, c_{\mathrm{L}}\big|_{\mathrm{T_{mp,i}}} \tag{2.14}$$

where melt pool density, ρ_{mp}, is found using:

$$\rho_{\mathrm{mp}}\big|_{\mathrm{T_{mp,i}}} = (1-\theta)\rho_{\mathrm{l}}|_{\mathrm{T_{mp,i}}} + \theta\rho_{\mathrm{s}}|_{\mathrm{T_{mp,i}}} \tag{2.15}$$

and the effective latent heat capacity is approximated by:

$$c_{\mathrm{L}}|_{\mathrm{T_{mp,i}}} = L\frac{d\Gamma_{\mathrm{m}}(\theta)}{dT} \tag{2.16}$$

where Γ_{m} is the mass fraction function defined as:

$$\Gamma_{\mathrm{m}} = \frac{1}{2}\frac{(1-\theta)\rho_{\mathrm{l}} - \theta\rho_{\mathrm{s}}}{\theta\rho_{\mathrm{s}} + (1-\theta)\rho_{\mathrm{l}}} \tag{2.17}$$

Note that the mass fraction function equals -0.5 before phase change and 0.5 afterwards. Total thermal energy released during phase transformation, between solid and liquid, is then:

$$L|_{\mathrm{T_{mp,i}}} = \int C_{\mathrm{L}}|_{\mathrm{T}_{i,o}} dT_{\mathrm{mp}} \tag{2.18}$$

The specific thermal capacitance of the powder bed is found using:

$$c_{\mathrm{pb}}\big|_{\mathrm{T_{pb,i}}} = (1-\emptyset)c_{\mathrm{s}}|_{\mathrm{T_{pb,i}}} \tag{2.19}$$

where c_{s} is the specific thermal capacitance of the solid phase material.

2.3. Gas Momentum and Energy Equations

The unsteady momentum and energy transfer within the pumped/supplied argon gas during a typical L-PBF process, were predicted by solving their governing equations as defined for three-dimensional Cartesian space. To predict the convective heat flux between the HAZ and argon gas, a detailed description of the flow field is necessary. The temperature, in turn, affects the fluid properties and can alter the flow field. These two problems need to be solved simultaneously. The employed domain is shown schematically in Figure 2.2.

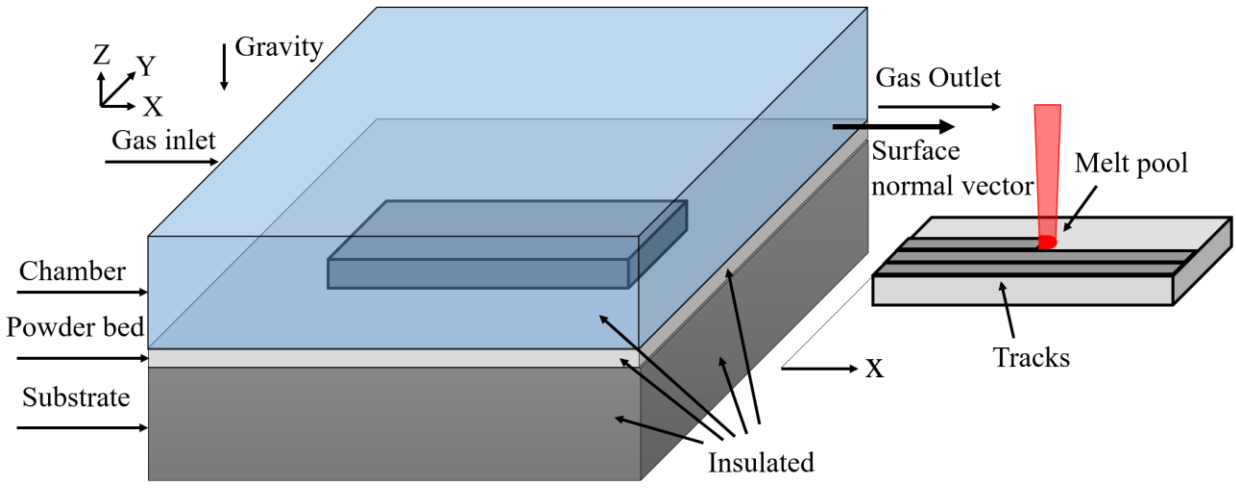

Figure 2.2 - Schematic view of substrate, powder bed, solidified tracks, and chamber including coordinate axes.

The argon density, velocity and temperature fields were found by numerically solving their appropriate governing equations, i.e. Eqs. (2.20) - (2.22), respectively. The governing equations, which include the continuity and Navier-Stokes equations, in their most general form are formulated as:

$$\frac{\partial \rho}{\partial \mathrm{t}} + \nabla \cdot (\rho \mathbf{u}) = 0 \tag{2.20}$$

$$\rho \frac{\partial \mathbf{u}}{\partial \mathrm{t}} + \rho(\mathbf{u} \cdot \nabla)\mathbf{u} = \nabla \cdot [-p\mathbf{I} + \boldsymbol{\tau}] + \mathbf{F} \tag{2.21}$$

$$\rho c_p \left(\frac{\partial T}{\partial t} + (\mathbf{u} \cdot \nabla)T\right) = -(\nabla \cdot \mathbf{q}) + \boldsymbol{\tau} : \mathbf{S} - \frac{T}{\rho}\frac{\partial \rho}{\partial T}\bigg|_p \left(\frac{\partial p}{\partial t} + (\mathbf{u} \cdot \nabla)p\right) + Q \tag{2.22}$$

where μ is the dynamic viscosity and ρ the local density of the argon gas, $\mathbf{u}$ is the local velocity vector, p is local pressure, c_p is the isobaric specific heat capacity, T is local absolute temperature, $\mathbf{q}$ is the local heat flux vector, $\boldsymbol{\tau}$ is the viscous stress tensor, Q is the volumetric heat source, $\mathbf{S}$ is the strain-rate tensor and $\mathbf{F}$ is the external volumetric force. Energy transfer to the argon, Q, via the laser beam was neglected. For the current model, flow near the powder bed was assumed to be Newtonian, while local disturbances to the argon flow field via plasma formation and/or spatter/vapor ejected from the melt pool were neglected. Effects of pore formation and melt pool dynamics on heat transfer were neglected. Argon viscosity and density were allowed to vary with local temperature. The strain-rate tensor can be written as:

$$\mathbf{S} = \frac{1}{2}(\nabla \mathbf{u} + (\nabla \mathbf{u})^T) \tag{2.23}$$

For a Newtonian fluid, with a linear relationship between stress and strain, the stress tensor reduces to:

$$\boldsymbol{\tau} = 2\mu\mathbf{S} - \frac{2}{3}\mu(\nabla \cdot \mathbf{u})\mathbf{I} \tag{2.24}$$

Uniform velocity was assigned as the boundary condition at the inlet, i.e.:

$$\mathbf{u} = -\mathbf{n}U_0 \tag{2.25}$$

where **n** is a unit surface normal pointing out of the domain at the inlet boundary as shown in Figure 2.2 and U_0 is the normal inflow speed. The gas flow outlet in the chamber was set as an open boundary condition, i.e. a pressure outlet, which implies normal stress and no viscous stress. The wall boundary condition was used for setting a no-penetration condition at the powder-bed/gas interface:

$$\boldsymbol{u} \cdot \boldsymbol{n} = 0 \tag{2.26}$$

The local heat transfer coefficient was calculated using:

$$\mathrm{h}_x = -\frac{k_\mathrm{g} \left.\frac{\partial T}{\partial z}\right|_{z=0}}{\left(T_{\mathrm{s,x}} - T_\infty\right)} \tag{2.27}$$

where $T_{s,x}$ is the local surface temperature. The convective heat flux from the powder bed to the adjoining gas is then defined as:

$$q_x = \mathrm{h}_x\left(T_{\mathrm{s,x}} - T_\infty\right) \tag{2.28}$$

where $\mathrm{h_x}$ is local heat transfer coefficient. Thermal radiation between the exposed powder bed area and the surrounding chamber wall was estimated using:

$$q_{\mathrm{rad,net}} \cong \sigma \varepsilon_{\mathrm{pb}}\left(\overline{T}_{\mathrm{s,x}}^4 - T_\infty^4\right) \tag{2.29}$$

2.4. Dimensionless Numbers

The local Reynolds number, $\mathrm{Re_x}$, for argon flow was defined as:

$$\mathrm{Re}_x = \frac{\rho_\mathrm{g}|\mathbf{u}|x}{\mu_\mathrm{g}} \tag{2.30}$$

where x is the distance from the beginning of the track. In general, Re_x is a ratio comparing inertial and viscous flow forces and can indicate whether a flow is laminar or turbulent. For flow across a smooth, flat surface, the critical Re_x in which the laminar to turbulence transition occurs is $\mathrm{Re}_{x,c} \approx 5 \times 10^5$. Other important non-dimensional numbers used herein for describing the argon momentum and energy transfer are the local Rayleigh, Ra_x, and Richardson numbers. Ri_x and Ra_x are described, respectively, as:

$$\mathrm{Ra}_x = \frac{g\beta_\mathrm{g}}{\nu_\mathrm{g}\alpha_\mathrm{g}}\left(T_{\mathrm{s,x}} - T_\infty\right)x^3 \tag{2.31}$$

$$\mathrm{Ri}_x = \frac{\mathrm{g}\beta_\mathrm{g}\left(T_{\mathrm{s,x}} - T_\infty\right)x}{|\boldsymbol{u}|^2} \tag{2.32}$$

where x is the characteristic length from the start of the track, g is the local acceleration due to gravity, β is the thermal expansion coefficient, ν is the gas kinematic viscosity, α is the gas thermal diffusivity, $T_{\mathrm{s,x}}$ is the local surface temperature (i.e. at location x), T_∞ is the fluid temperature far from the surface of the object, and $|\mathbf{u}|$ is the local gas speed. The Rayleigh number can indicate whether local heat transfer in the gas is dominated more by convection or by conduction as determined via a critical Ra. For Ra $\gtrsim 10^3$ [101] the heat transfer is driven more by convection. For the Richardson number, if it is much less than unity, then buoyancy is negligible in the flow. If it is much greater than unity, buoyancy is dominating.

Non-dimensional groups describing local heat transfer are the Prandtl, Nusselt, and Biot numbers, as defined below, respectively:

$$\mathrm{Pr}_\mathrm{x} = \frac{C_{\mathrm{p,g}}\mu_\mathrm{g}}{k_\mathrm{g}} \tag{2.33}$$

$$\mathrm{Nu}_\mathrm{x} = \frac{h_\mathrm{x}x}{k_\mathrm{g}} \tag{2.34}$$

$$\mathrm{Bi}_\mathrm{x} = \frac{h_\mathrm{x}x}{k_\mathrm{pb}} \tag{2.35}$$

where h_x is the local heat transfer coefficient. For small Prandtl numbers, i.e. Pr << 1, thermal diffusivity plays a larger role relative to momentum diffusivity. The Nusselt number is a dimensionless heat transfer coefficient expressed as a ratio of convective to conductive heat transfer. The Biot number represents the ratio of the heat transfer resistance of the powder bed (i.e. solid body) to that of the convection at the exposed powder bed surface.

CHAPTER 3

Numerical Methodology and Validation

3.1. Numerical Methodology

The governing equations, i.e. Eqs. (2.1) - (2.3), were solved numerically via the finite difference method to estimate argon density, motion, and heat transfer. Heat transfer in the substrate, powder bed, built part (i.e. solidified track) and melt pool were solved using Eqs. (2.6) - (2.8). To ensure meaningful physical simulations, each medium was discretized using appropriately-sized tetrahedral meshes. As shown in Figure 3.1, the tetrahedral meshes used for the powder bed were uniformly dispersed and ~3800 μm^3 in size (mesh lengths of ~35 μm) – providing for approximately 60 cells within the melt pool during simulation. The substrate consisted of elements ranging in size; from 12,000 μm^3 (mesh lengths of ~100 μm) at the top of the substrate, to larger elements of 25,000 μm^3 (mesh lengths of ~200 μm) toward the bottom of the substrate. An inflating boundary-layer mesh scheme – with ~50 μm cells near the powder bed/gas boundary and ~200 μm cells near the center of the chamber – was used for simulating gas momentum/energy transfer in the L-PBF chamber. Time was discretized into equal time steps of Δt = 8 ms. Simulations were performed using the COMSOL Multiphysics® 5.1 commercial software in conjunction with custom coding scripts.

Since the local temperature gradient consists of three spatial components, i.e. parallel-to-track (x), perpendicular-to-track (y), and normal-with-substrate (z) directions, its magnitude was calculated herein. The magnitude of the temperature gradient (for a given time) between

neighboring elements separated by $<\Delta x, \Delta y, \Delta z>$ was estimated using a second-order central difference, i.e.:

$$\|\nabla T\| \cong \left\| \left\langle \frac{T(x+\Delta x,y,z)-T(x-\Delta x,y,z)}{2\Delta x}, \frac{T(x,y+\Delta y,z)-T(x,y-\Delta y,z)}{2\Delta y}, \frac{T(x,y,z+\Delta z)-T(x,y,z-\Delta z)}{2\Delta z} \right\rangle \right\| \quad (3.1)$$

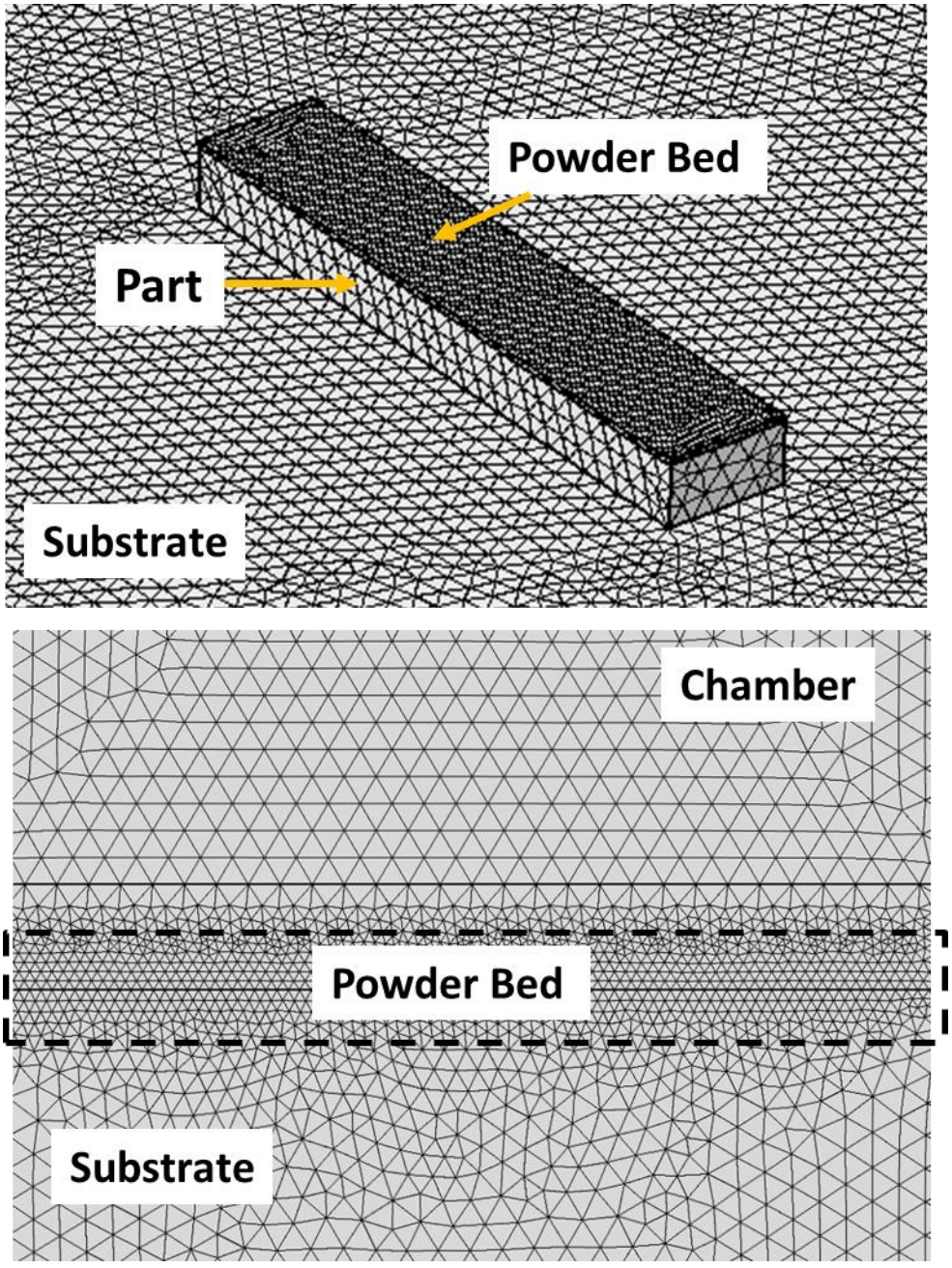

Figure 3.1 - (Top) isometric view of meshed powder bed, substrate and part (part height not to scale) and (bottom) side view of meshed substrate, powder bed and chamber.

To calculate the local heat transfer coefficient used in Eq. (2.27), the z-wise temperature gradient within the argon boundary layer near the surface was found by finite difference as:

$$\left.\frac{\partial T}{\partial z}\right|_{z=0} = \frac{T(x,y,z+\Delta z) - T(x,y,z)}{\Delta z} \tag{3.2}$$

The local temperature time rate of change, i.e. the heating or cooling rate at a given point, was estimated using:

$$\frac{\partial T_i}{\partial t} \cong \frac{T_i(t+\Delta t) - T_i(t)}{\Delta t} \tag{3.3}$$

The utilized temperature-dependent properties of argon [102], as well as solid and liquid properties of Ti-6Al-4V [103], are presented in Figure 3.2 and Figure 3.3, respectively. For all simulations it was assumed that there was zero oxygen content in the chamber. In addition, vaporization heat transfer and mass transfer in the melt pool were neglected. Finally, as discussed, the powder bed was assumed to behave as a continuum modeled using effective properties.

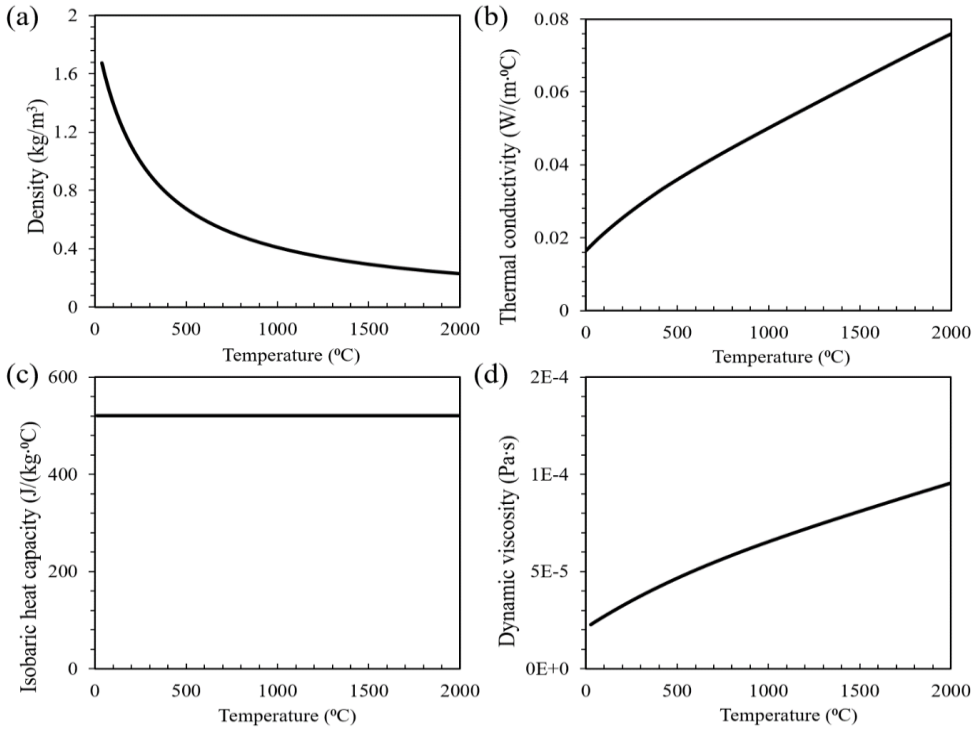

Figure 3.2 - Physical properties of argon versus temperature for: (a) density (b) thermal conductivity, (c) specific heat capacity, (d) dynamic viscosity.

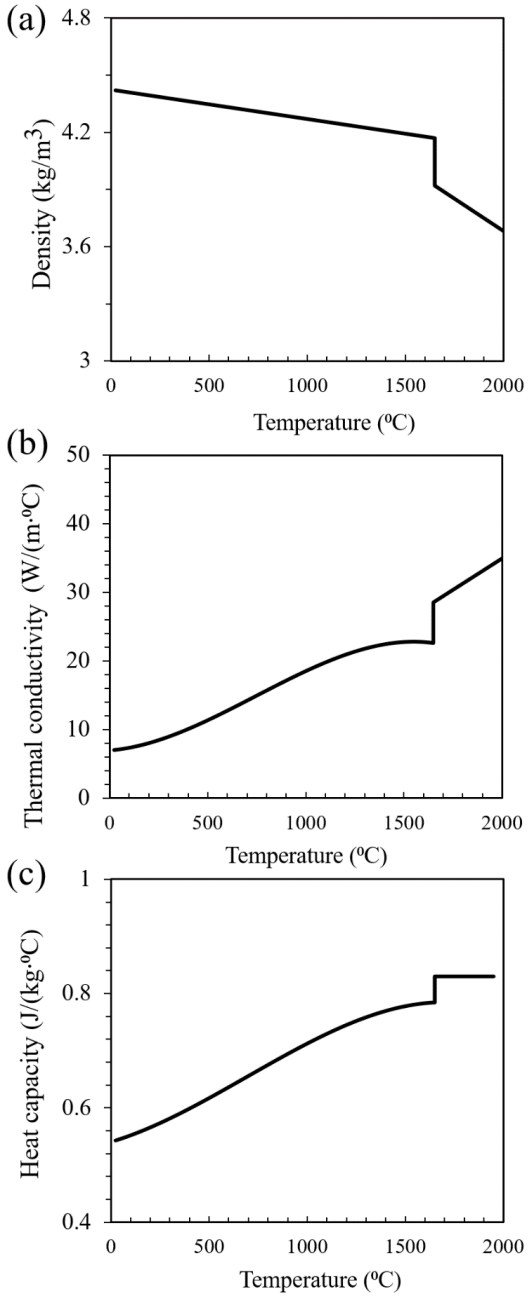

Figure 3.3 - Physical properties of solid- and liquid-phase Ti-6Al-4V versus temperature: (a) density (b) thermal conductivity and (c) specific heat capacity

3.2. Validation

3.2.1. Convection Heat Transfer

The methods employed for quantifying the convection heat transfer during a representative L-PBF process were validated/benchmarked by simulating, separately, common forced and free

convection environments with known heat transfer. For forced convection, the steady-state, laminar flow of argon between two, smooth parallel unit-width plates were simulated. As shown in Figure 3.4 (a), the length of each plate was set as 3 m and the distance between the plates, *b*, was set as 0.05 m. Non-slipping, Newtonian fluid flow with an inlet temperature of T_∞ = 10 ºC was assumed and a uniform heat flux boundary was imposed, i.e. q = 10 W/m². The inlet flow velocity profile was assumed to follow Eq. (3.4) [104] consisting of an average inlet velocity of U_{avg} = 1 m/s:

$$U(y) = \frac{3}{2} U_{\text{avg}} \left[1 - 4 \left(\frac{y}{b} \right)^2 \right] \tag{3.4}$$

The local heat transfer coefficient was estimated via simulation by solving Eq. (2.27) while the analytical local heat transfer coefficient for fully-developed flow described in Figure 3.4 (a) was estimated using Eq. (3.5) [104]:

$$\mathrm{h}_x = \frac{\mathrm{Nu} \cdot k}{x} = \frac{8.235 \cdot k}{x} \tag{3.5}$$

The analytically predicted and simulated heat transfer coefficients are presented in Figure 3.4 (b). In the entrance region, the flow was not developed yet and the predicted heat transfer coefficient varied from the analytical solution. However, as the flow became more developed, the relative percent difference between the predicted heat transfer coefficient and analytical solution decreased to 10.5%.

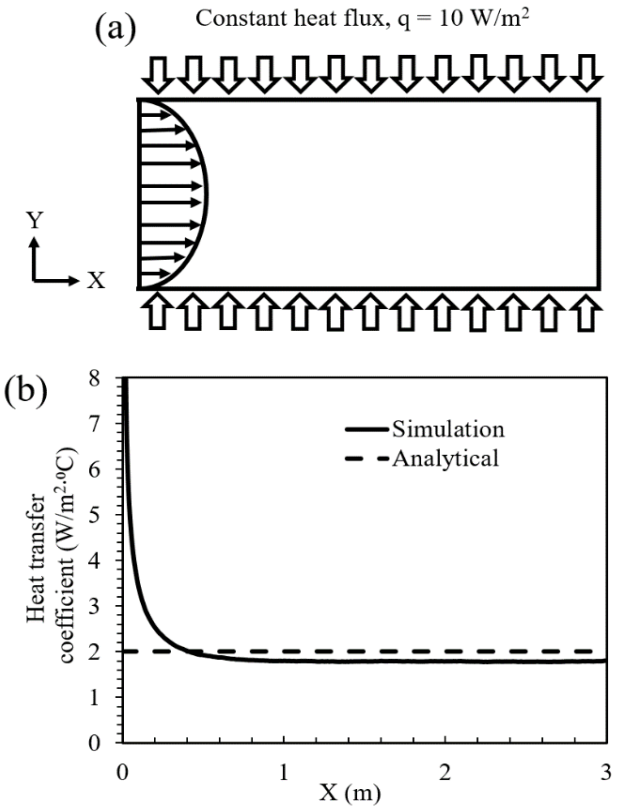

Figure 3.4 - (a) Description of flow field between two parallel plates, (b) analytical and simulation results for heat transfer coefficient.

For validating/benchmarking the numerical free convection calculations, experimental results published by Turgut et al. [105] were used. Two horizontal plates, as shown in Figure 3.5, with different isothermal temperatures were used. The plates were made of copper and their size was 0.3048×0.1524 m^2. Temperature at various locations were measured using 24 gage fiberglass insulated copper–constantan thermocouples. The experimental error due to thermocouples was report as ± 0.2 °C. For the Nusselt number, the maximum relative uncertainty was estimated to be 5.8%. The plate separation distance was 15 mm and the difference between the lower plate temperature and ambient air temperature was allowed to vary from 9 °C and 60.3 °C. The distance between plates was filled with air. The characteristic length, L_c, was defined as:

$$L_c = A/p_w \tag{3.6}$$

where A is the area of the plate surface and p_w is its wetted perimeter. Effects of temperature difference between the bottom plate and ambient air temperature on heat transfer coefficient were examined experimentally. The results for the case when the distance between plates was 15 mm are shown in Table 3.1. As presented, the numerical simulation prediction is within 10% of the experimental results. Considering the fact that the experimental method has up to 5.8% margin of error, the results are fairly accurate.

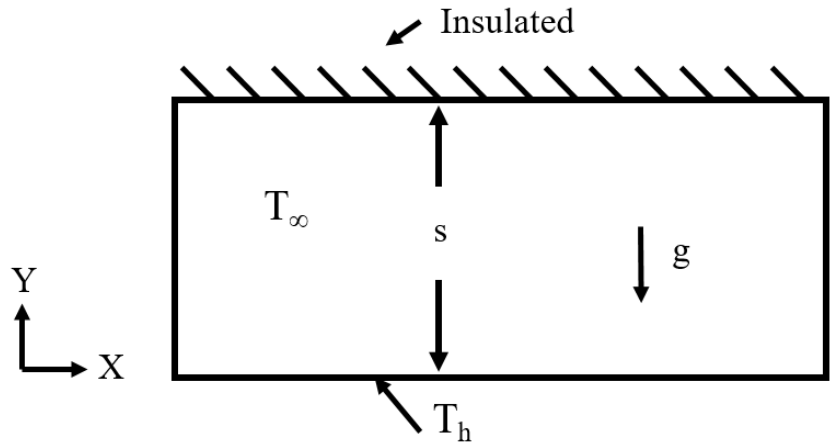

Figure 3.5 - Physical domain of the experimental setup used for validating numerical free convection.

Table 3.1 - Nusselt number from numerical simulation and experimental results.

Temperature difference (T_h-T_∞, °C)	10	20	30	40	50	60
Experimental Nusselt number [105]	1.8	2.0	2.1	2.2	2.4	2.4
Simulated Nusselt number	1.6	1.8	1.9	1.9	2.1	2.2

3.2.2. Melt Pool

To validate the ability of the presented model in predicting heat transfer within the HAZ, experimental results obtained by Criales et al. [106] were used for comparison. Criales et al. used an EOS M270 L-PBF system with a single-mode continuous-wave Ytterbium fiber laser with 100

μm laser spot size. Nickel alloy 625 (i.e. Inconel 625), gas-atomized powder with an average particle size of 35 μm was used. Fabrication was done under nitrogen gas atmosphere. The substrate and powder material were similar in chemical composition. The process parameters used in the experiment are summarized in Table 3.2. A digital optical microscope was utilized to obtain images of the electro-polished surfaces from which the melt pool width and depth were measured. During experiments, laser power was kept constant at 169 W, while scan speeds were varied between 725 mm/s and 875 mm/s. The results from these experiments were compared with results from the numerical model herein and these results are summarized in Figure 3.6 and Table 3.3. As shown in Figure 3.7, the simulated melt pool possessed similar length and depth as that reported by Criales et al. [106]. For both scan speeds investigated, the simulated melt pool did not differ more than 14% of the reported geometry. The simulated, maximum melt pool temperature under the specified process parameters was found to be ~2500 ºC.

Table 3.2 - Parameters used for simulating the L-PBF of single-track, single-layer of Nickel alloy 625.

System	EOS M270
Substrate material	Nickel alloy 625
Substrate size	25 x 25 x 5 cm^3
Powder description	Gas-atomized, air-dried
Mean particle diameter	35 μm
Powder layer thickness	20 μm
Powder bed porosity	0.4
Laser spot diameter	100 μm
Laser power	169 W
Scan speed	875 mm/s
Powder bed absorptance	0.38 [107]
Absorption coefficient	10^6 cm^{-1} [96]
Emissivity	0.35
Building volume	25 x 25 x 35 cm^3
Shielding gas type	Nitrogen
Shielding gas inlet temperature	20 ºC
Shielding gas inlet flow rate	0.25 m^3/s
Chamber wall temperature	20 ºC

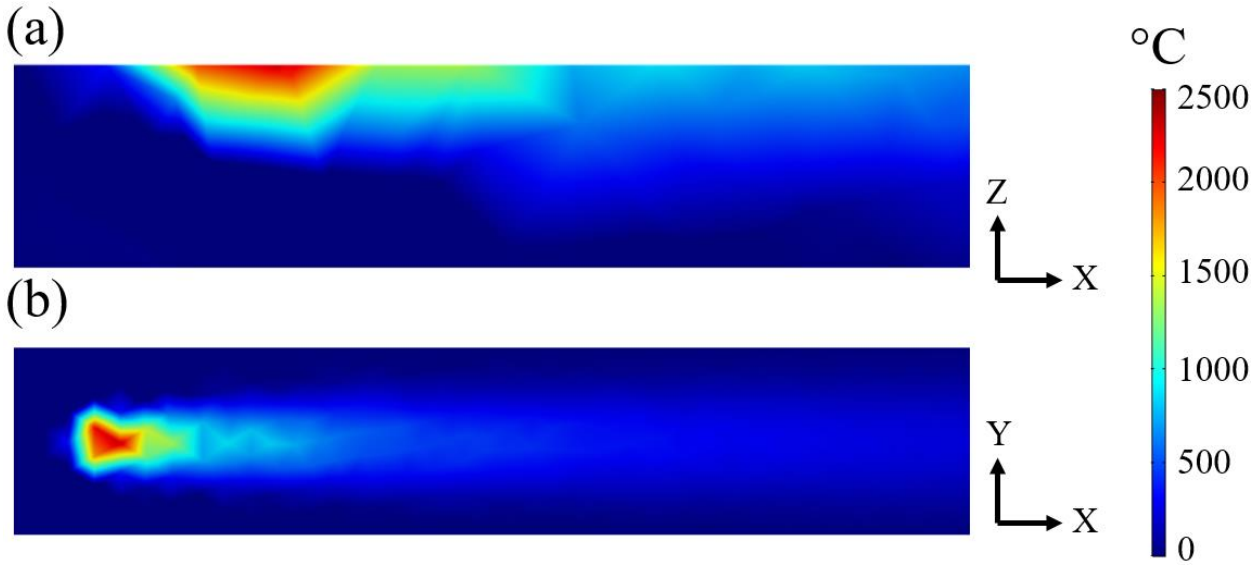

Figure 3.6 - (a) Front and (b) top view of Nickel alloy 625 melt pool with 169 W laser power and 875 mm/s scan speed (laser is moving right to left).

Table 3.3 - Experimentally-measured [106] and simulated Nickel alloy 625 melt pool dimensions during single-track L-PBF for different scan speeds at a laser power of 169 W.

Laser power (W)	Scan speed (mm/s)	References	Melt pool width (µm)	Melt pool depth (µm)
169	875	Experimental [106]	134	35
		Simulation	125	30
169	725	Experimental [106]	159	51
		Simulation	140	45

Various other experiments were conducted for validating the numerical model. A L-PBF system (PHENIX 100) with fiber laser was utilized. The fiber laser consisted of an intensity with a Gaussian profile, 50 W power limit, 1075 nm wavelength and operated at a spot size of 70 µm (i.e. A_{mp}). The L-PBF process was conducted under argon atmosphere, which was pumped into the 0.2 m^3 chamber at a rate of approximately 167 cm^3/s. Parts were built upon a modified SS 17-4 PH substrate for monitoring temperature. The substrate consisted of a centrally-located Ø = 3.2 mm thru-hole and 1 x 50 mm^2 slot, to allow for thermocouple attachment and wire travel, respectively. An embedded, pre-calibrated Type-C thermocouple (OMEGA, bead diameter ≅ 75 µm) was utilized by attaching its welded tip (bead) to the substrate. The substrate was 10 x 10 x 1

cm^3 in bulk dimension, and as shown in Figure 3.7, the thermocouple was located approximately 3 mm (± 0.5 mm) below exposed surface. Temperature data were recorded using a data logger (ICP DAS I-7018) at a rate of 1 Hz. Maximum error associated with measured temperature was found to be approximately 4.5 °C (±1 %), while nominal error of the data logger was 0.2 %.

The material used in the process was SS 17-4 PH powder (LPW, Inc.) with an average particle size of 25 μm. Thermal conductivity of bulk material is approximately 12 W/m·□C at room temperature. The latent heat of fusion for the material is 270 kJ/kg [108]. The absorptance, α, was assumed to be constant at 0.65 [109]. To measure the density, 50 ml of powder was loaded to a 100-ml glass graduated cylinder. Then the cylinder was weighted using electronic analytical balance (RADWAG AS 220/C/2) with accuracy of 0.1 mg. The density was calculated according to the relationship: mass/volume. For the current investigation, the density of the powder bed was measured to be approximately $\rho_p = 4680$ kg/$m^{3.}$

Two different sets of experiments were performed. The first experiment was performed without powder in the machine – with only the modified substrate exposed. The laser moved from the starting point, as shown in Figure 3.7, to the edge of the plate in a diagonal line repeatedly. Three different scan speeds and powers were employed and these parameters are summarized in Table 3.4. The scan pattern was only performed once and then the substrate was allowed to cool back to room temperature before a new set was performed.

Table 3.4 - Process parameters utilized for nine laser scans along thermocouple-embedded substrate

Power\speed	50 mm/s	150 mm/s	250 mm/s
25.0 W	Exp. #1	Exp. #2	Exp. #3
37.5 W	Exp. #4	Exp. #5	Exp. #6
50.0 W	Exp. #7	Exp. #8	Exp. #9

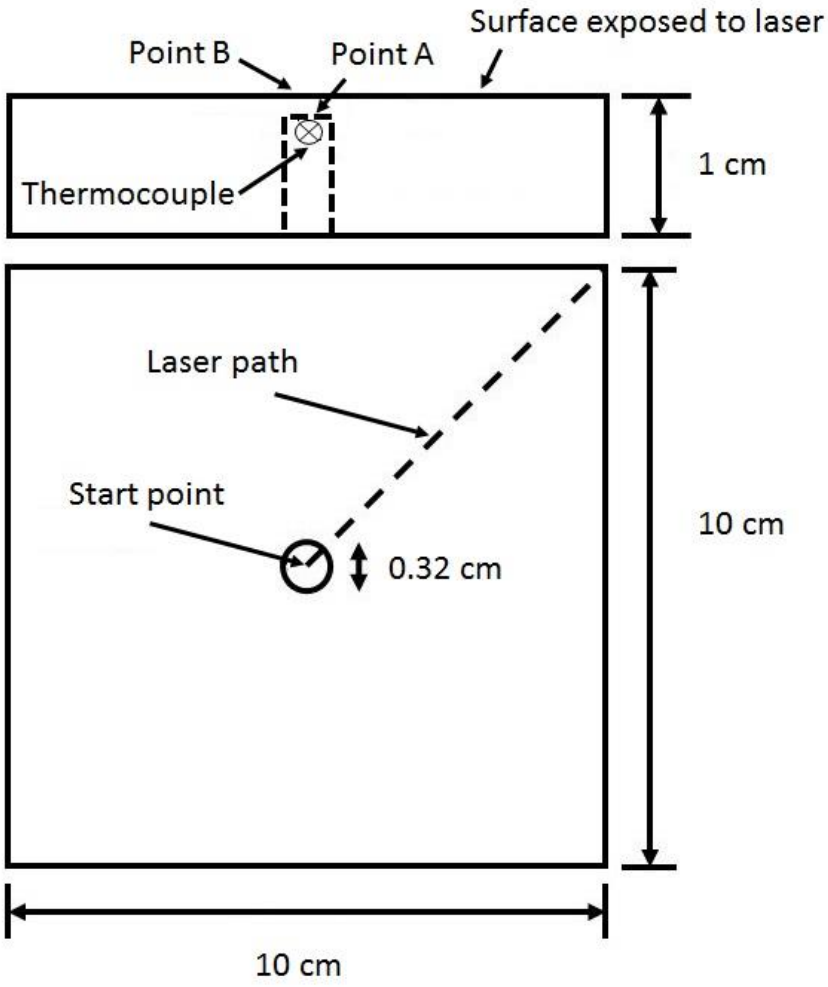

Figure 3.7 - Dimensions of thermocouple-embedded substrate with start point and laser path

The second experiment consisted of fabricating a multitrack wall structure atop the thermocouple-embedded substrate. The length and width of the wall was 50 mm and 2 mm, respectively. The multitrack wall was constructed using a collinear/unidirectional scan pattern. The process parameters were held constant with time and consisted of a 50 W (± 0.5 W) laser output power, 50 mm/s scan speed, 30 µm layer thickness and 50 µm hatching pitch. Results from the experiment were used to verify numerical simulations. Hence, the substrate design and powder bed were ensured to match those related to the L-PBF machine/process utilized for validation experiments.

The temperature response at Point A (shown in Figure 3.7), as measured experimentally and numerically for Exp. #7 (single laser pass) is shown in Figure 3.8. For the numerical simulation of this experiment, the temperature under the substrate (Point A) was extracted after simulating heat transfer through powder and substrate. The results demonstrate that the temperature within the substrate during laser exposure does not surpass 60 ºC, and that the substrate cools within ~ 15 s. However, the experimental data appears to agree well with numerical data for all experiments conducted, i.e. Experiments #1 - #9, Table 3.4, the numerical model approach is shown to be validated in Figure 3.8 (a).

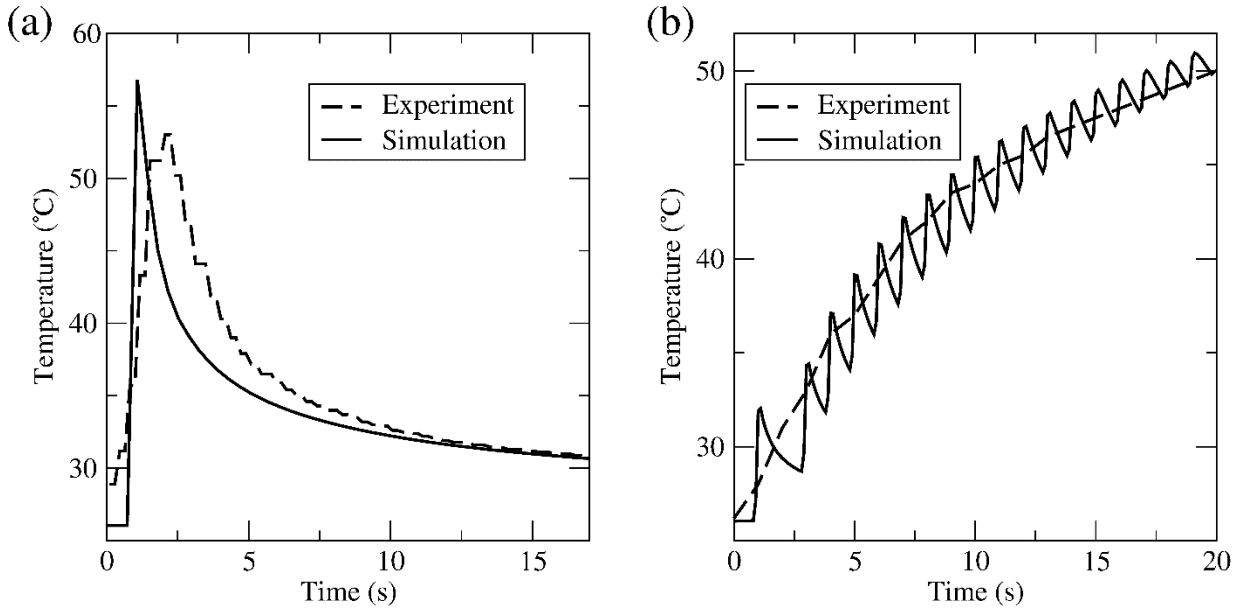

Figure 3.8 - (a) Temperature response at Point A with respect to time during Exp. #7 process parameters. (b) Temperature response at Point A for the first layer of deposition with respect to time during SS 17-4 PH multitrack wall build using Exp. #7 process parameters

Figure 3.8 (b) shows the simulated substrate temperature response during deposition of the SS 17-4 PH multitrack wall while using the same parameters from Exp. #7. The effect of scan pattern on the temperature response at Point A below the substrate is clearly evidenced by the multiple temperature peaks vs. time. Note that the experimental data is not oscillating due to the

employed temperature collection frequency; however, the general temperature rise agrees very well with the numerical simulation. During deposition of one layer, the temperature of the substrate has increased by 25 ºC, to a maximum temperature near 50 ºC. Note that the temperature cycling amplitude appears to reduce, as the laser gets closer and closer to Point A.

3.3. L-PBF Simulation

The validated numerical model was used for simulating the L-PBF (powder bed size = 5 × 1 × 0.05 mm^3) of a single-track of Ti–6Al–4V with a length of 5 mm. The size of the substrate and chamber size were 10 x 10 x 1 cm^3 and 25 x 25 x 35 cm^3, respectively. Note that the area of the powder bed was smaller relative to the substrate. The five sides of the powder bed exposed to argon were subjected to convection and radiation heat transfer. Process parameters used for simulation correspond to the default process parameters of an EOS M290 for fabricating dense Ti–6Al–4V parts and are presented in Table 3.5. The measurement, i.e. data extraction, location was at the middle of the track during its L-PBF.

The simulation was repeated using different mesh sizes to ensure mesh-independent results. These results are summarized in Table 3.6. From Table 3.6, it may be seen that maximum melt pool temperature converges as cell size is reduced. The maximum melt pool temperature changed less than 2% when reducing the mesh volumes from 5000 μm^3 to 3800 μm^3. Based on these results, simulations were performed with a mesh size of 3800 μm^3.

Table 3.5 - Parameters used for simulating the L-PBF of single-track, single-layer of Ti–6Al–4V.

System	EOS M290
Substrate material	Ti-6Al-4V
Substrate size	10 x 10 x1 cm^3
Length of track	5 mm
Powder description	Gas-atomized, air-dried
Mean particle diameter	35 µm
Powder layer thickness	50 µm
Powder bed porosity	0.4
Laser spot diameter	100 µm
Laser power	170 W
Scan speed	1250 mm/s
Powder bed absorptance	0.25 [110]
Absorption coefficient	10^6 cm^{-1} [96]
Emissivity	0.35
Melt pool thermal conductivity	25 – 45 W/m·°C [111]
Building volume	25 x 25 x 35 cm^3
Shielding gas type	Argon
Shielding gas inlet temperature	20 ºC
Shielding gas inlet flow rate	0.25 m^3/s
Chamber wall temperature	20 ºC

Table 3.6 - Maximum melt pool temperature during L-PBF of Ti-6Al-4V for various mesh resolutions for laser power of 170 W and scan speed of 1250 mm/s.

Mesh size (µm^3)	**Maximum melt pool temperature (ºC)**
3800	3080
5000	3030
10000	2850
15000	2500

CHAPTER 4

Single-Laser Additive Manufacturing

4.1. Introduction

Utilization of constant, time-invariant L-PBF process parameters is a common practice given its simplicity and repeatability. For such cases the major process parameters, such as laser speed, power, hatching space, etc., all remain constant on either a per track or per layer basis. Such use of time-invariant process parameters can lead to a temperature field more conducive for residual stress (or, thermal deformation), pore formation, inhomogeneous microstructure and more; due primarily to variations in heat flux locality and/or rates. If an operator aims to minimize the variation in PBF process parameters throughout a build, quality control is perhaps easiest achieved by strategically determining optimal scan patterns a priori, such that adverse thermal effects associated with part size, geometry and complexity are minimized. Such scan patterns are at the full discretion of the part designer/manufacturer and implementable on a per-layer basis

In this particular study, the effects of scan pattern on temperature distribution and local cooling rates of SS 17-4 PH during L-PBF is studied. In addition, the effectiveness of changing them will be compared to changing the process parameters. In addition, effects of substrate size on temperature response was calculated, as well. Results from simulation were verified using thermocouple. Therefore, heat transfer through substrate was taken into account. Finally, effects of changing each of these parameters on microstructure of the part and the size and direction of its grains were studied.

4.2. Substrate Thermal Response

Figure 4.1 presents the simulated temperature response of the substrate at Point B during the build of the first four layers of a thin wall of width 1 mm and length 10 mm. Laser power was 50 W and scan speed was 50 mm/s. In addition, layer thickness, Δl, and hatching space were 30 μm and 50 μm, respectively. Peak temperature at each point occurs during the deposition of that point, although it will decrease significantly afterwards. Nevertheless, during the deposition of the neighbor point on the next track, the temperature would reach 85% of peak temperature. The peak temperature at point B continues to decrease during deposition of next tracks and it would reach 10% of its original peak during deposition of 20^{th} track. At the start of depositing new layer, the initial temperature is different from previous layer and effects of sensible heating is evident. In addition, during fabricating of each new layer, peak temperature at previously deposited layer are smaller compared to new layer. It could be observed from Figure 4.1 that during deposition of second, third and fourth layer, peak temperature at point B in first layer has decreased 50%, 30% and 15% respectively.

High temperature gradients generate high tensile residual stress. Temperatures gradients in the x and z directions at point A are presented at Figure 4.2. Laser power was 50 W and scan speed was 50 mm/s. It may be seen that temperature gradient in x direction is maximum just before and after the point heated by laser spot. In addition, thermal gradient in z direction is maximum at the heating location and it decreases significantly.

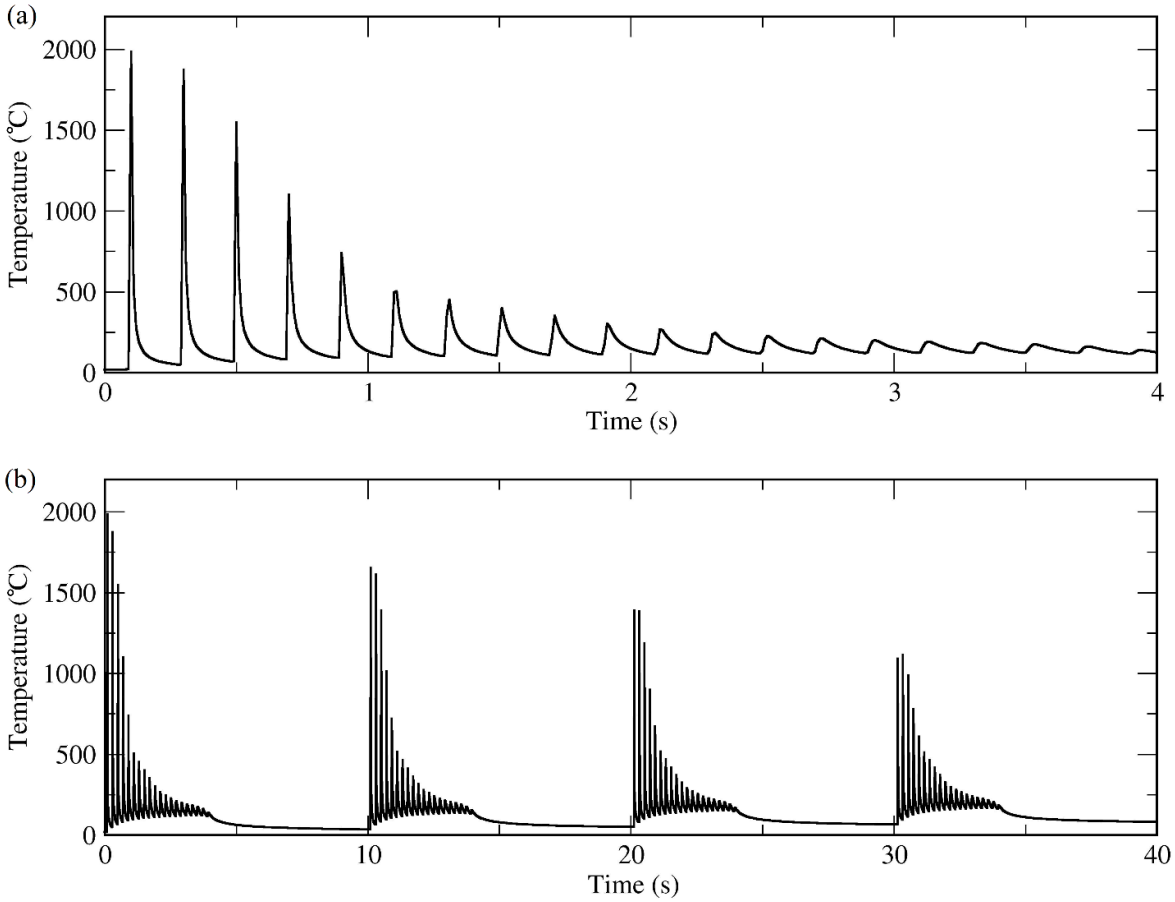

Figure 4.1 - Temperature response at the middle of first track (Point B) while depositing 20 tracks (each track is 10 mm) in (a) one layer and (b) four layers of SS 17-4 PH with respect to time, 50 W laser power, 50 mm/s scan speed using scan pattern #A

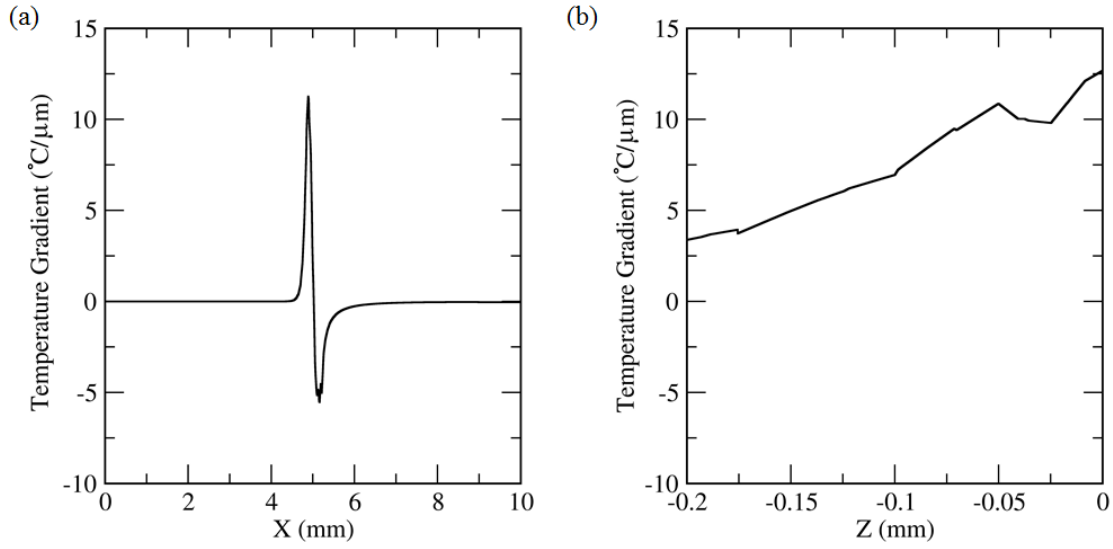

Figure 4.2 - Temperature gradient during fabrication of single track (10 mm) at t = 0.1 s, 50 W laser power, 50 mm/s scan speed at (a) X direction, (b) Z direction

In Figure 4.3, time rate of change of temperature while deposition of two layers at point B is presented. Each layer consists of four tracks. The process parameters are the one as Exp. #7. Temperature time rate of change peaked when it hits the point and it will continue to decrease during the deposition of nearby tracks. At the same time, during the deposition of next layer, temperature time rate of change is 33% lower compared to the amount of first layer. During the fabrication of each track, nearby tracks are affected by heat transfer. Based on continuous cooling transformation (CCT) diagram for SS 17-4 PH, the minimum temperature for affecting part microstructure is 1000 K. Above this temperature, the part microstructure depends on cooling rate.

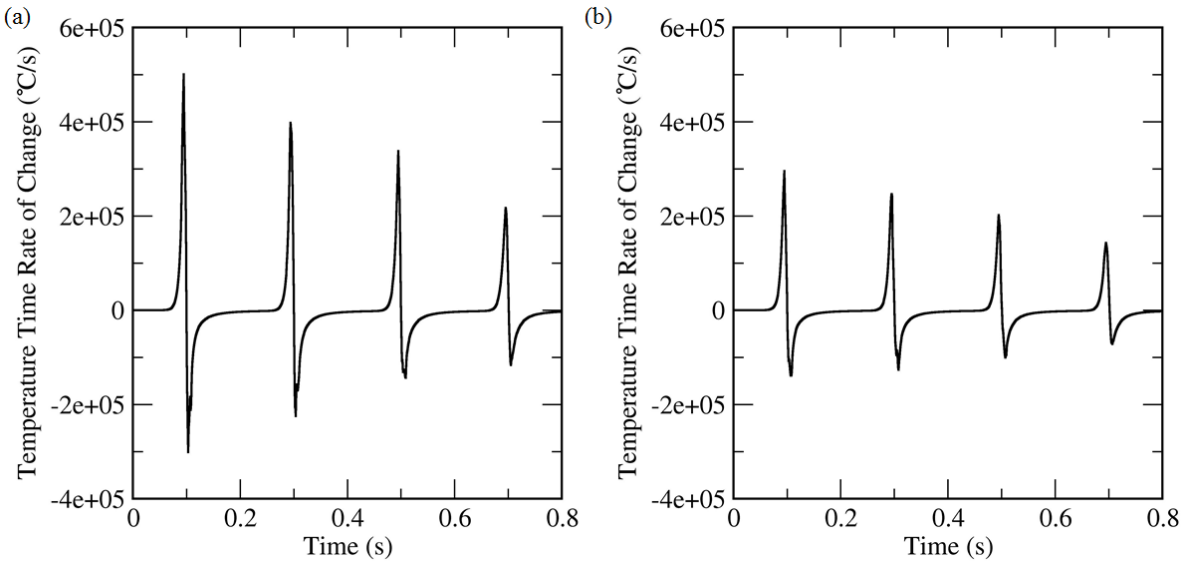

Figure 4.3 - Temperature time rate of change at Point B while fabricating four 10 mm tracks of SS 17-4 PH using scan pattern #A with respect to time: laser power = 50 W & scan speed = 50 mm/s (a) first layer and (b) second layer

4.3. Effects of Scan Pattern

The effects of scan pattern on substrate temperature response was investigated by using each of the two scan patterns shown in Figure 4.4 (a)-(b) for the simulated L-PBF fabrication of a SS 17-4 PH multitrack wall. The first pattern, Figure 4.4 (a), is the laser moving in one direction, the second one, Figure 4.4 (b), show laser moves in alternating direction.

The temperature response at measurement location for all two scan patterns, using process parameters from Exp. #7, is shown in Figure 4.4 (c). From Figure 4.4 (c), it may be seen that each scan pattern provides for a unique temperature response at measurement location within the substrate, and thus, a different temperature response in the surrounding powder bed and part. The temperature response dampened as it diffuses through part, powder bed and substrate. The results show that, as the trend observed in Figure 4.4 (c), the temperature oscillations in amplitude as the laser approaches the measurement point. Hence, the severity of temperature fluctuations is decreased as the bulk part temperature increases for a given layer. That is due to increase in initial temperature during the deposition of each new track. The multidirectional scan pattern (e.g. scan pattern A) provided for largest temperature amplitudes. The reason for difference in peak temperature is due to difference between time interval of deposition of each point and neighboring point. Note that although the time invested per layer for all of two scan patterns is the same, the deposited part will experience completely different cooling and heating rates – as evidenced by the amplitude and frequency of the temperature oscillations at Point B. These different cooling rates will directly affect the encumbered part microstructure.

The heating and cooling rates (i.e. temperature time rate of change) using scan pattern A and B are presented in Figure 4.4 (d). The temperature was obtained through the simulation of multitrack wall build. By comparing the plots, it is observed that temperature rate is strongly dependent on scan pattern. Scan pattern (A) has slightly higher cooling rate. These phenomena can be explained by time interval between fabrications of neighbor tracks. In this case, time interval between fabrications of neighboring track for scan pattern #B is twice the time interval of scan pattern #A. By increasing the time interval, the point has more time to cool down. It can be concluded that by using random scan pattern, each point has more time to cool down and each

point would experience more uniform build pattern. By knowing the effects of scan pattern on thermal response, controlling the temperature rate become feasible.

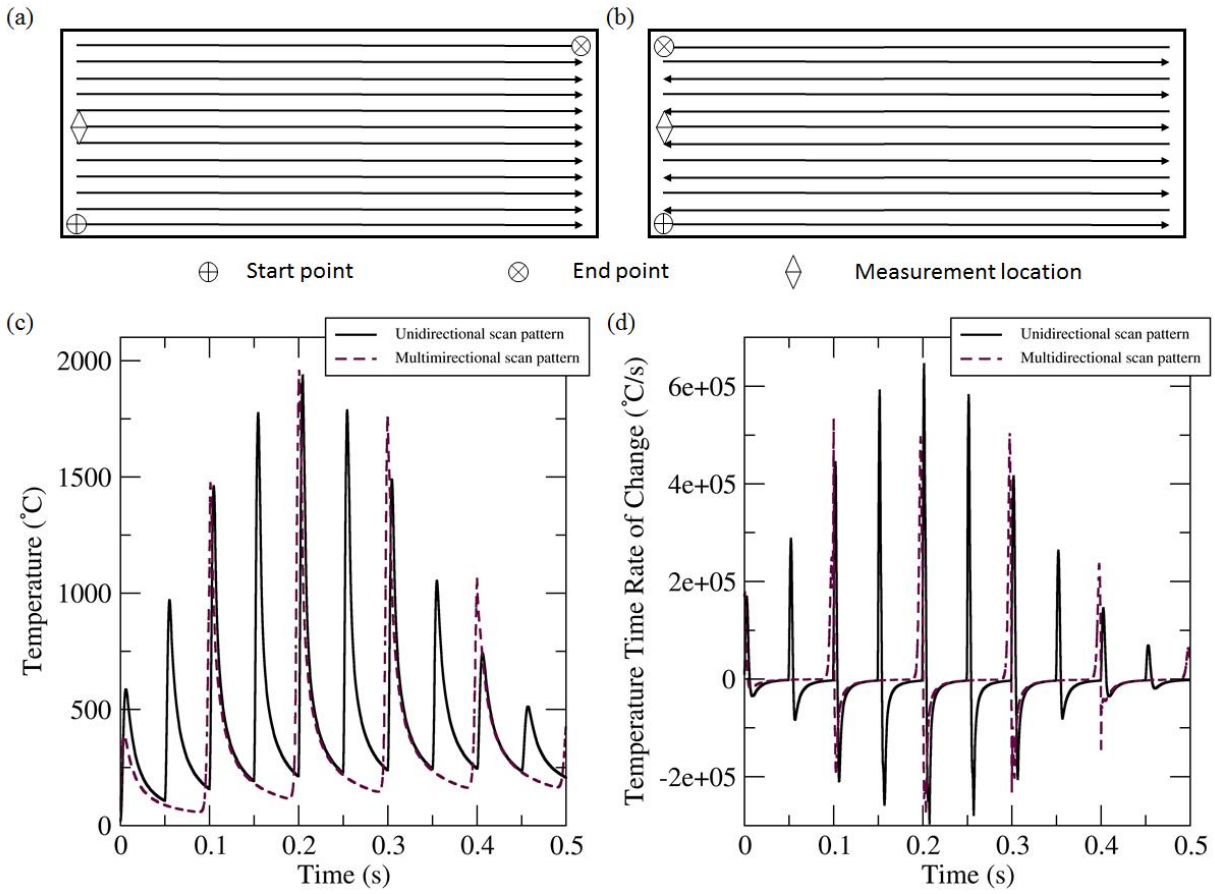

Figure 4.4 - Scan patterns investigated for fabrication of a multitrack wall with dimensions of 2.5 mm by 0.5 mm: (a) unidirectional/lengthwise (scan pattern #A), (b) alternating (scan pattern #B), (c) Variation of temperature (d) temperature time rate of change of measurement location with respect to time with laser power = 50 W & scan speed = 50 mm/s with two different scan patterns during fabrication of SS 17-4 PH

Another important factor in categorizing mechanical properties of build parts is magnitude and direction of conductive heat flux. The microstructure of the part is function of the value and direction of thermal gradient. Thijs et al. [43] reported that the grain growth is perpendicular to the isotherm. Therefore, the grain growth direction is parallel to direction of conductive heat transfer. In Figure 4.5, heat direction in x, y and z directions are shown at the beginning, middle and end of the build track. Heat flux is maximum at z direction. The reason for that is due to absorption of

most of energy through powder bed. Rest of the absorbed energy will spread in y and z direction. It is observed in Figure 4.5 that there is heat flux at x and y direction at the center of laser.

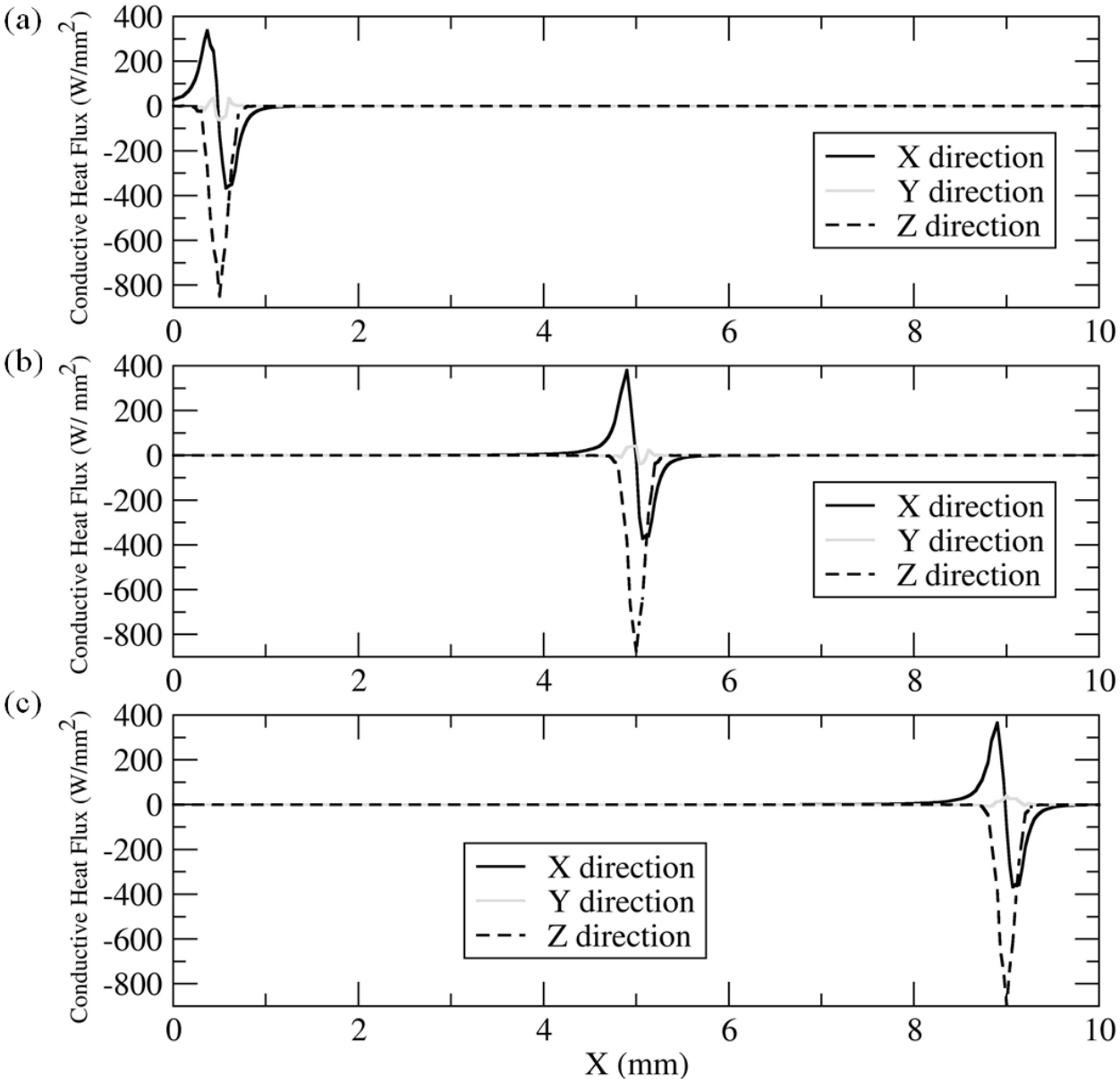

Figure 4.5 - Conductive heat flux at x, y and z direction, with scan pattern #A and 10 mm track length, with laser power = 50 W & scan speed = 50 mm/s at (a) t = 0.4 s, (b) t = 0.5 s, (c) t = 0.6 s

In Figure 4.6, the heat flux at x, y and z direction is shown at three locations, beginning, middle and end of the track, using two different scan patterns. From observing Figure 4.6 two points can be understood. First, the heat flux is not same at molten pool in different location.

Therefore, it is possible to have non-homogenous parts. Conductive heat flux magnitude decreased 2% from the beginning of the track until the end of it. Additionally, by changing scan pattern, heat flux will be different. From Figure 4.6, it is observed that alternating scan pattern has 87% higher conductive heat flux in the x direction compared to unidirectional. These variations are due to change in changes in initial conditions. Another point is that heat flux direction has not changed significantly by changing between the two scan patterns. However, if widthwise scan pattern was used, the heat flux direction would change as shown in Figure 4.5. Consequently, the easy way to control heat flux is by designing appropriate scanning strategy, i.e. meander, stripe or island pattern [112]. If for each layer, the scanning strategy rotated by β, the grains become more equiaxed and parts would act isotropic. Usually β is chosen to be 90º or 45º.

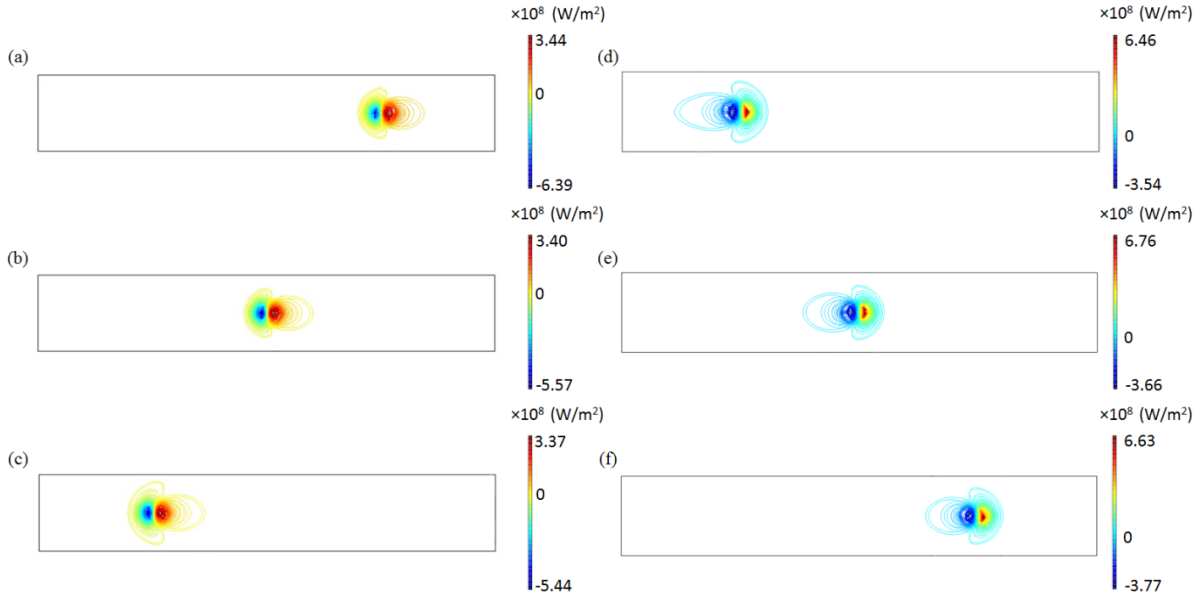

Figure 4.6 - Conductive heat flux in x direction using Exp. 7 process parameters and the track length of 5 mm, with scan pattern #A, at (a) t = 0.3 s, (b) t = 0.35 s, (c) t = 0.4 s, Conductive heat flux at x direction, with scan pattern #B at (d) t = 0.3 s, (e) t = 0

4.4. Effects of Part Size

The effects of part geometry on temperature response and cooling rate of measurement location were studied by fabricating a multitrack wall with various lengths via simulation. As shown in Figure 4.7 (a) - (b), a 0.5 mm thick wall with a length of 2.5 mm or 5 mm with height of 5 mm was fabricated. The scan pattern #A, Figure 4.4 (a), and process parameters from Exp. #7 were utilized. The temperature response of measurement location for the first deposited layer is provided in Figure 4.7 (c) - (d).

In Figure 4.7 (c) – (d), it is observed that as the length of the wall decreases, for a given set of process parameters and scan pattern, the peak temperature increases. When the length of sample is reduced from 5 mm to 2.5 mm, the peak temperature increases from 2000 ºC to 2100 ºC. As the size of the part increases, its heat capacitance increases too. Consequently, the same process parameters during the fabrication would cause higher temperature of the parts, powder bed and substrate. The same reason applied for higher temperature at higher layers.

The heating/cooling rates are influenced by the geometry of the part, as shown in Figure 4.7 (e) – (f). As the length of the part increases, the cooling rate increases. The cooling rate at higher layers are lower compared to the first deposited layers. That could be explained by heat accumulation at smaller sample or higher layers. Consequently, that would result in lower cooling rate and thermal gradient. Yadollahi et al. [50] built a sample via L-PBF using two build orientation, vertical and horizontal. The samples are made of SS 17-4 PH. Both vertical and horizontal samples are cylindrical rods possessed an 8 mm diameter and 75 mm height. The retained austenite in horizontal sample was about ~7% while vertical sample contained an average of ~3% retained austenite. The level of retained austenite will go up higher that the cooling rate level continues to go up. That is consistent with results from this section.

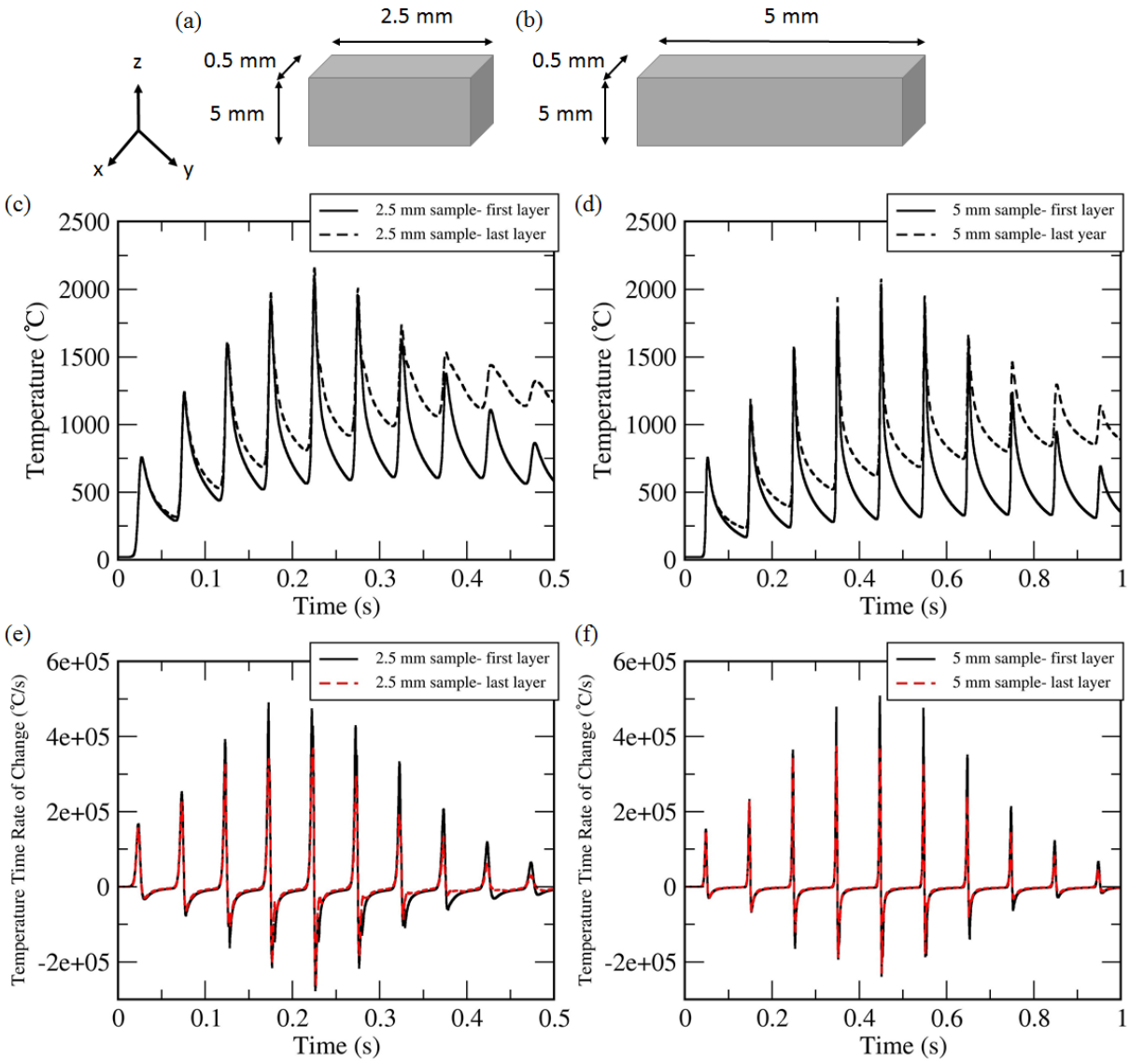

Figure 4.7 - (a), (b) Multitrack wall cross-sectional dimensions (c), (d) Variation of temperature and (e), (f) Temperature time rate of change at measurement location with respect to time with laser power = 50 W & scan speed = 50 mm/s, and scan pattern #A with two different geometries

4.5. Effects of Substrate Size

Substrate size can affect heat accumulation during L-PBF, and this is demonstrated in Figure 4.8 as it shows effects of substrate thickness on thermal response. The case study for this study was changing the thickness of substrate while keep the area constant. The exposed area was kept

constant at 100 cm^2 and the thickness for case #1 and case #2 was chosen 10 mm and 5 mm. The process parameters chosen for this study is 20 W laser power and 50 mm/s scan speed. The measurement location is at point B. It is observed from Figure 4.8 that as the volume of substrate decreases; the temperature would increase due to accumulative heat. This effect becomes more important during the cooling phase. That is due to diffusion of heat through substrate during the cooling. As time passed, effects become more important. During the fabrication of first track, peak difference of temperature at point B is about 10 ºC. However, during the fabrication of fourth track, it becomes nearly 100 ºC. Based on this result, authors expect that by increasing the substrate volume, the cooling rate will increase. Consequently, the level of martensite in the part decreases.

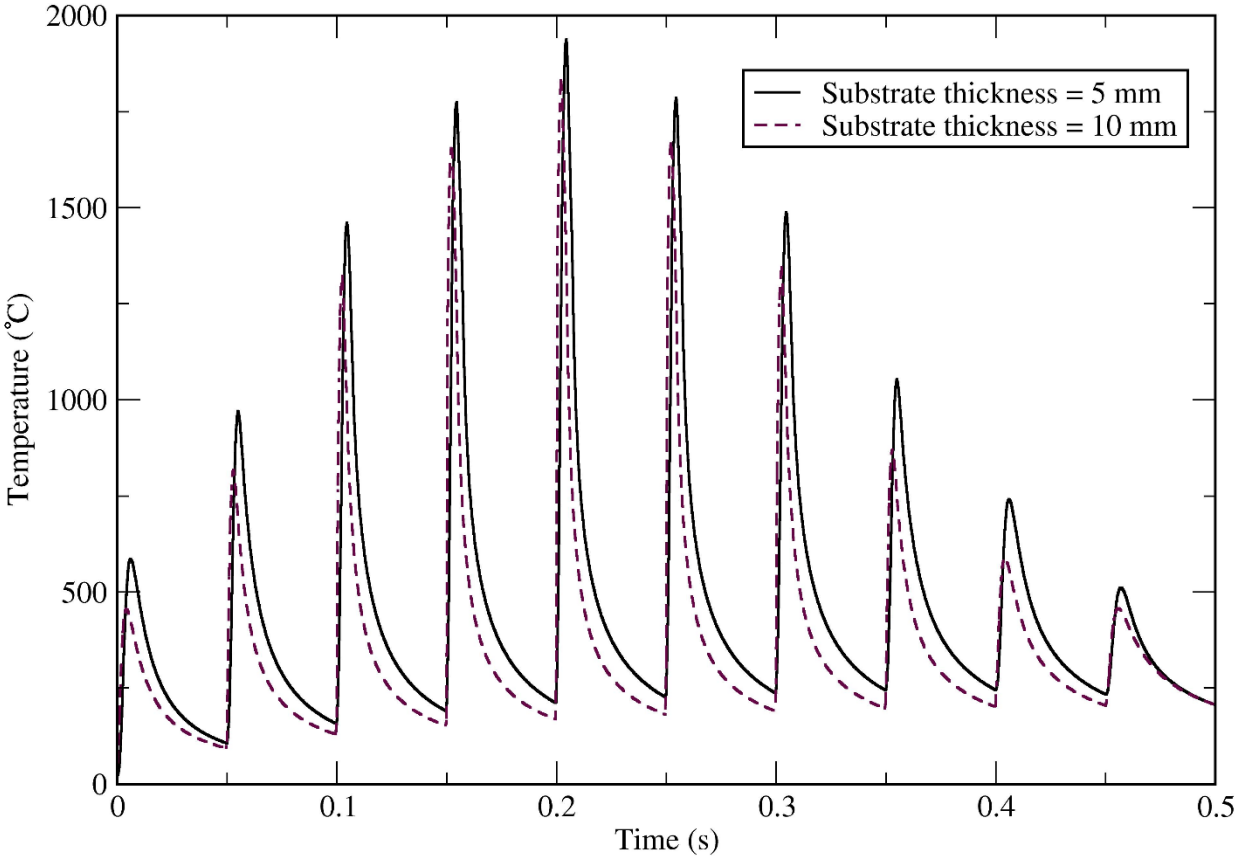

Figure 4.8 - Effects of thickness of substrate on temperature variation at Point B for the first layer of deposition with scan pattern #A (ten tracks, 2.5 mm) with respect to time during fabrication of SS 17-4 PH thin wall build 50 W laser power, 50 mm/s scan speed

CHAPTER 5

Multi-Laser Additive Manufacturing

5.1. Simulation

The validated numerical model was used for simulating the multi-laser PBF (ML-PBF) of a Ti–6Al–4V parallelepiped structure with dimensions of 10 x 5 x 0.06 mm^3 that were built using multiple tracks and consisting of two total layers. To present mechanically-relevant results, the parameters associated with the L-PBF process reported by Vilaro et al. [113], and summarized in Table 5.1, were utilized since they were proven effective in producing fully-dense Ti–6Al–4V material. This particular study focused on fabricating tensile specimens via a Trumpf LF250 L-PBF system and no thermal monitoring was performed. As necessary, the validated numerical model employed parameters and constants (see Table 5.1) discussed earlier in Section 3.2; some examples include the melt pool liquid thermal conductivity and powder bed porosity.

Using the parameters in Table 5.1, the L-PBF of an individual, two-layered parallelepiped structure was simulated for various laser numbers and scan strategies. Scan strategies were selected to reduce overexposure of regions near island border lines; this is because some synchronous, multi-laser scan strategies can result in instances where all lasers are in close proximity, thus affecting prediction accuracy. The number of islands and sub-islands were varied while track sweeping directions (i.e. X+ or Y+ directions) were held constant for all islands/sub-islands employed. The scan strategy was repeated for the first and second layers in all simulations conducted. In total, 13 different simulations, i.e. S1-S13, were performed, with S1-S5 employing

a X+ track sweep direction, S6-S10 employing a Y+ track sweep direction and S11-S13 employing 'mixed' X+/Y+/X-/Y- track sweep directions.

Table 5.1 - Parameters used for simulating the L-PBF and ML-PBF of a Ti–6Al–4V parallelepiped based on those reported by Vilaro et al. [113].

System	Trumpf LF250 [113]
Substrate material	Ti-6Al-4V [113]
Substrate size	10 x 10 x1 cm^3
Powder description	Gas-atomized, air-dried [113]
Mean particle diameter	35 µm [113]
Powder layer thickness	30 µm [113]
Powder bed porosity	0.4
Hatch spacing	200 µm [113]
Laser spot diameter	220 µm [113]
Laser power	200 W [113]
Scan speed	500 mm/s [113]
Powder bed absorptance	0.25 [110]
Absorption coefficient	10^6 cm^{-1} [96]
Emissivity	0.35
Melt pool thermal conductivity	25 – 45 W/m·K [111]
Shielding gas type	Argon
Shielding gas flow rate	167 cm^3/s
Shielding gas temperature	20 ºC
Chamber wall temperature	20 ºC
Convection heat transfer coefficient	12.7 $W/m^2 \cdot K$

Islands and sub-islands were built using a quadrant-, halves- or fourths-style IDS. For the quadrant division scheme, the part (or island) was divided into four equally-sized islands (or sub-islands) with division lines intersecting at the center of the part (or island). The sequence in which quadrants were built varied with number of lasers used. For P=1, the top-left quadrant, Q1, was fabricated and the next island manufactured was selected in a clockwise (CW) fashion, with the bottom-left quadrant being Q4, as shown in Figure 5.1. The 'fourths' island division scheme allowed islands to be positioned adjacent to each other in a single row with X-parallel or Y-parallel division lines, while the 'halves' division scheme allowed for two islands formed by a Y-parallel division line. The part was also fabricated using no division scheme, i.e. a 'full' or 'single' island division. Figure 5.1 illustrates the various scan patterns (SPs) investigated for: P=1, P=2, P=4;

referred to now as SP-A, SP-B, and so forth, until SP-H, corresponding to Figure 5.1(a) – 5.1(h), respectively. The various simulations performed with respect to the investigated scan patterns and division schemes/sequences are summarized in Table 5.2. The various scan patterns investigated are shown schematically in Figure 5.1.

Table 5.2 - Simulations performed for the single- and multi-laser PBF of the 2-layered Ti-6Al-4V parallelepiped

Sim. #	Scan pattern	# islands (or lasers)	# sub-islands per island	LIP	IDS	Sub-island sequence	Track sweep direction (track scan direction)
S1	SP-A	1	1	0	Full	N/A	Y+ (X+)
S2	SP-C	1	4	1	Quadrant	Q1, Q2, Q3, Q4	Y+ (X+)
S3	SP-C	2	2	3	Halves (X)	(Q1, Q4), (Q2, Q3)	Y+ (X+)
S4	SP-C	4	1	2	Quadrant	N/A	Y+ (X+)
S5	SP-F	4	1	2	Fourths (X)	N/A	Y+ (X+)
S6	SP-B	1	1	0	Full	N/A	X+ (Y+)
S7	SP-D	1	4	1	Quadrant	Q1, Q2, Q3, Q4	X+ (Y+)
S8	SP-D	2	2	3	Halves (Y)	(Q1, Q4), (Q2, Q3)	X+ (Y+)
S9	SP-D	4	1	2	Quadrant	N/A	X+ (Y+)
S10	SP-G	4	1	2	Fourths (Y)	N/A	X+ (Y+)
S11	SP-E	1	4	1	Quadrant	Q1, Q2, Q3, Q4	Y+(X+), X+(Y+), Y-(X-), X-(Y-)
S12	SP-E	4	1	2	Quadrant	N/A	Y+(X+), X+(Y+), Y-(X-), X-(Y-)
S13	SP-H	4	4	3	Quadrant	Q1, Q2, Q3, Q4	Y+(X+), X+(Y+), Y-(X-), X-(Y-)

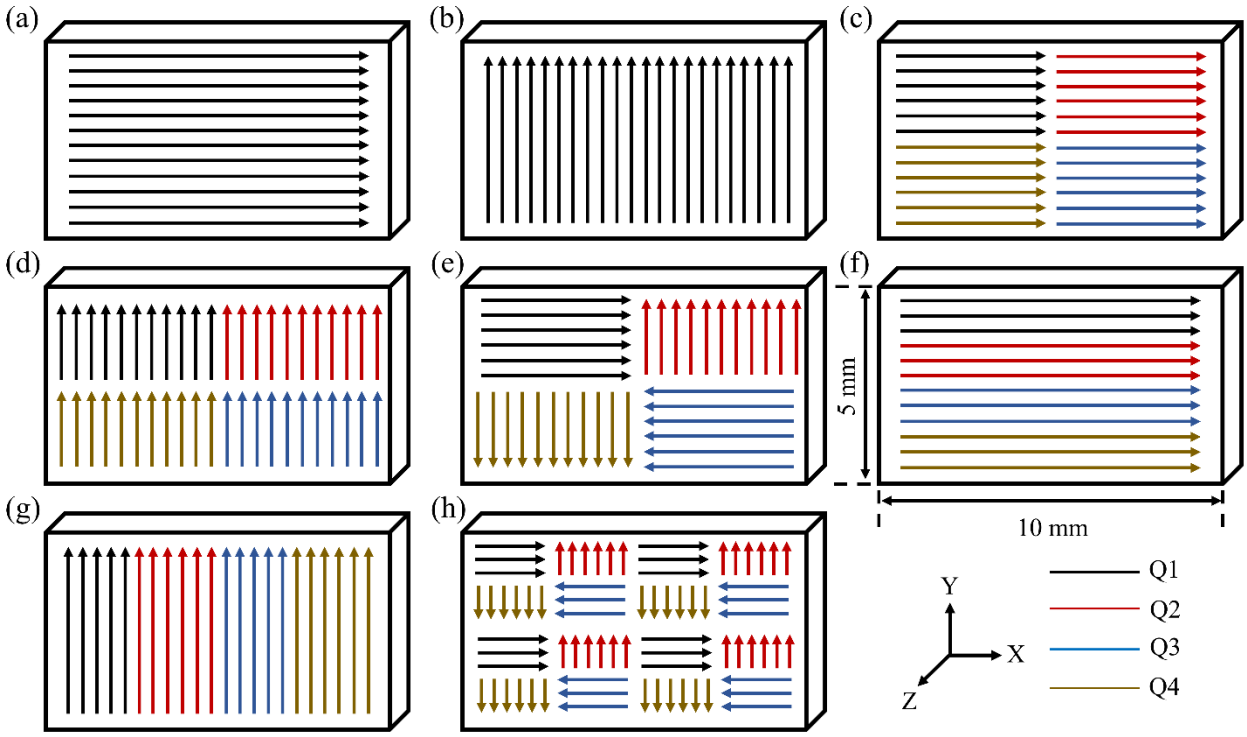

Figure 5.1 - Schematic of scan patterns used for simulations: (a) SP-A, (b) SP-B, (c) SP-C, (d) SP-D, (e) SP-E, (f) SP-F, (g) SP-G, (h) SP-H; Q1-Q4 refer to sub-islands/islands.

Simulation S1 employed SP-A and a single laser dedicated to a single island (i.e. LIP-0) with laser tracks swept in the Y+ direction, parallel to the part's shortest edge. Simulation S2 employed the quadrant IDS and scan pattern SP-C while using a single laser swept in the Y+ direction for the in-series building of four sub-islands in the following CW sequence: Q1, Q2, Q3 and then Q4. Here, Q1-Q4 are the names of sub-islands as shown in Figure 5.1. Simulation S4 is similar to S2 except that four lasers were used for in-parallel building of islands Q1-Q4 (i.e. LIP-2). Simulation S3, being a LIP-3 build plan, employed the halves IDS and scan pattern SP-C while using two lasers swept in the Y+ direction for the in-series building of two sub-islands per island in the following sequence: Q1 then Q4 in-parallel to Q2 then Q3. Simulation S5 employed the fourths IDS and scan pattern SP-F while using four lasers swept in the Y+ direction for the in-parallel building of four islands. Simulations S6-S10 followed the strategies detailed by S1-S5,

respectively, except that scan patterns SP-B (for S6), SP-D (for S7-S9) and SP-G (for S10) were employed along with a X+ track sweep directions. Simulations S11-S13 employed the quadrant IDS and tracks with mixed sweep directions. Simulation S11 employed a single laser and scan pattern SP-E for the in-series building of four sub-islands in the Q1-Q4 sequence (LIP-1). Simulation S12 employed four lasers and scan pattern SP-E for the in-parallel building of four islands (LIP-2). Finally, S13 employed four lasers and scan pattern SP-H for the in-series building of four sub-islands per island; all sub-islands were built in the Q1-Q4 sequence (LIP-3).

Sixteen points, P1-P16, were imposed along each layer for extracting local temperatures, cooling rates and temperature gradients during simulations S1-S13. Each 'extraction point' was centered within a sixteenth of the parallelepiped volume as illustrated in Figure 5.2. These temperature measurement/exaction points enabled a means to investigate local, transient behavior of the powder bed/part temperature distribution.

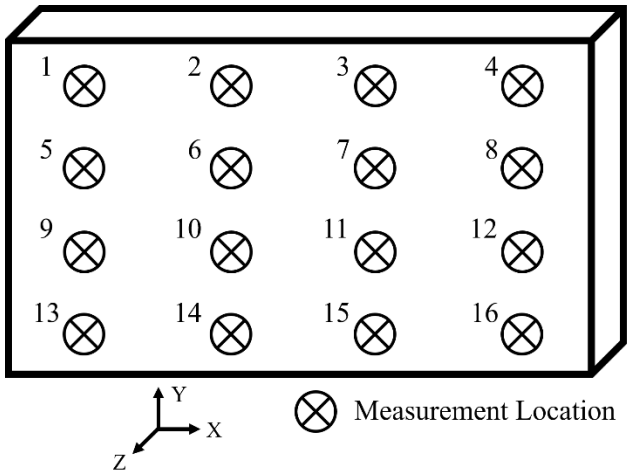

Figure 5.2 - Schematic of the sixteen measurement locations P1-P16 used to record temperature, temperature gradient and time rate of change.

The real-time distance between lasers dedicated to Q2-Q4 relative to Q1 for S4 and S12 is shown in Figure 5.3. This relative motion of island scan paths allows another means to understand measured thermal phenomena. For instance, it may be seen that the distance remains constant with

time for S4 and S9 in which unidirectional island sweep directions are used while it oscillates with time for S12, in which each island has a different laser track sweep direction. A constant or oscillating relative laser position during LIP > 2 will affect the layer thermal response. Local temperatures will increase when two lasers approach each other and their relative distance decreases. By keeping the laser distance constant between regions, the thermal response will be more homogenous.

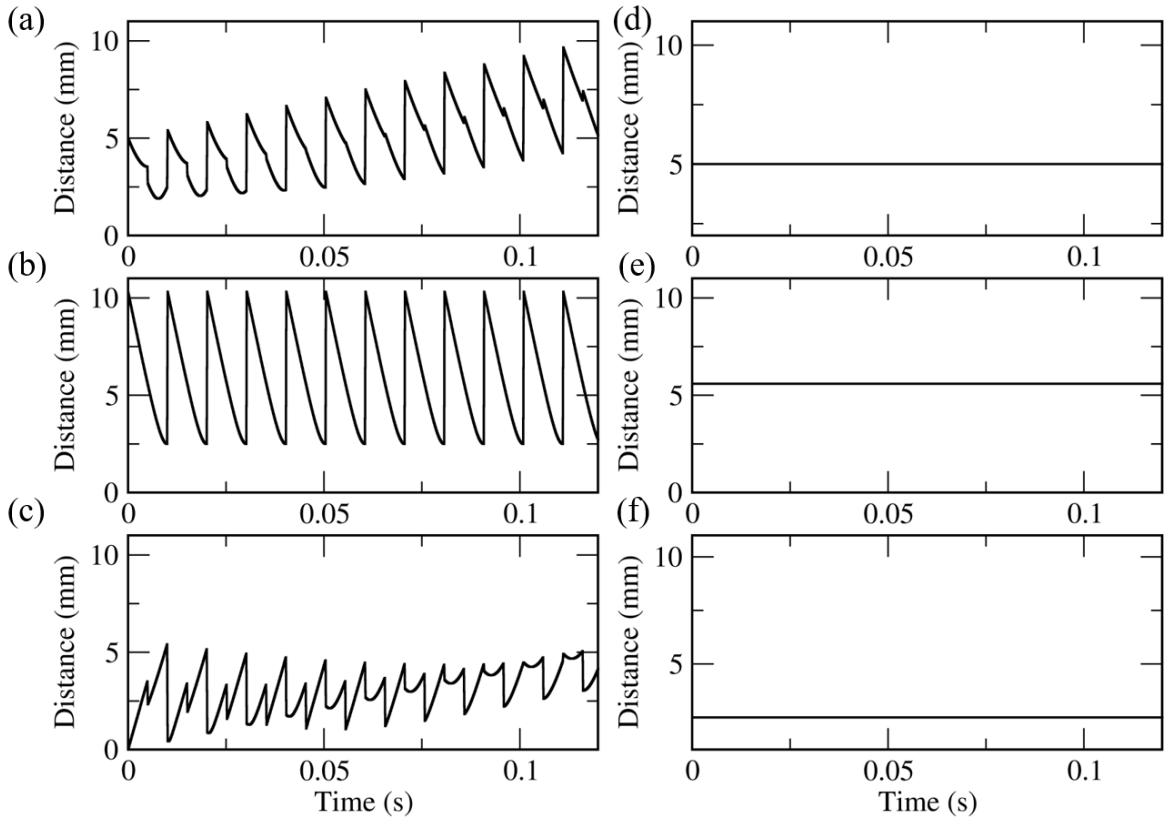

Figure 5.3 - Relative distance vs. time during S12 between Q1 and (a) Q2, (b) Q3, and (c) Q4; Relative distance vs. time during S4 between Q1 and (d) Q2, (e) Q3, and (f) Q4.

5.2. Temperature of Melt Pool and Heat Affected Zone

The melt pool and HAZ temperature distributions, halfway through building the first layer, for S1, S4 and S5 are shown in Figure 5.4 (a) – Figure 5.4 (c), respectively, while a magnified view

of a representative melt pool corresponding to S1 is provided in Figure 5.4 (a). The representative melt pool is found to be semi-circular with a maximum temperature zone possessing a diameter near that of the laser. The HAZ possesses a thermal 'wake' that follows behind the melt pool. Each laser produces identical melt pools and HAZs. As shown in Figure 5.4, increasing the number of lasers increases the temperature of the powder bed and local HAZs since the area corresponding to elevated temperatures for a layer, or total HAZ, during its manufacture also increases. During ML-PBF, the powder bed receives more energy in less time and track lengths become shorter due to in-parallel island building; thus, thermal energy has less time to diffuse in between tracks, and local temperatures can increase. This elevated powder bed temperature can prove important when calibrating instrumentation to monitor the IR signature of the powder bed. Powder recyclability for use with ML-PBF will most likely be different from that corresponding to single-laser PBF, since surrounding powder bed temperature is slightly more elevated in general; especially for cases in which track lengths are shorter.

For the inspected scan strategies (i.e. S1-S13), it was found that the number of lasers, and thus the number of HAZs, has little effect on melt pool temperature and morphology during the majority of the build. This is primarily due to the locality of directed laser energy, and the fact that the HAZ is very small relative to the remainder of the powder bed and substrate, which contains a relatively high thermal capacitance. A significant portion of the energy delivered to the powder bed is used for melting and superheating the melt pool; thus, initially hotter powder bed regions do not necessarily translate to hotter melt pools. Initially-hotter powder beds can impact, although slightly, the wetting behavior of the melt pool, local heating rates, HAZ cooling rates, and more; thus ML-PBF of relatively small parts may result in such parts possessing different microstructures than those fabricated using the same process parameters via traditional, single-

laser PBF. If the size of the powder bed and/or part were reduced, or if a more convergent scan pattern were employed (i.e. laser relative distances decrease) so that HAZs would be closer to each other more often, then the melt pool shape should be more influenced. The thermal conductivity of the powder bed is very small relative to that of the solidified tracks/part. As a result, the heat transfer through the un-melted powder bed is less and melt pool asymmetry exists, as shown in Figure 5.4 (a). The HAZ temperature is more distributed along the solidified region as opposed to the neighboring powder bed region. All islands receive the same heat flux during processing; thus, only minor differences in peak temperatures, i.e. ± 50 ºC, were observed at locations P1-P16 during S1-S13. As expected, the amount of time invested per layer decreases with the addition of each new laser.

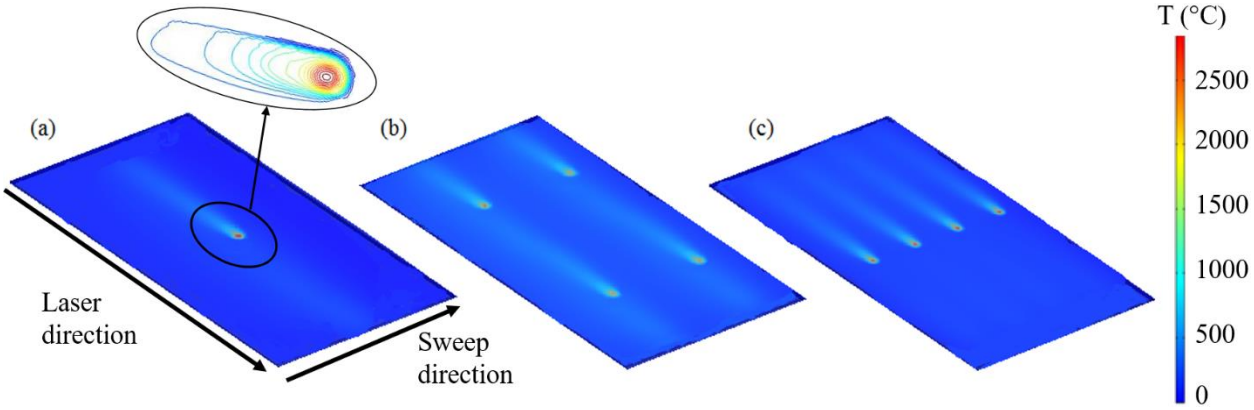

Figure 5.4 - Temperature response (in ºC, with legend shown on right) of powder/part/substrate during L-PBF of first layer for (a) S1, (b) S4 and (c) S5

The simulated melt pool temperatures were found to possess local extremes around ~2850 ºC, located near the center of the penetrating laser beam, as evidenced in Figure 5.4. This temperature is significantly higher, by ~1000 ºC, than the liquidus temperature of Ti-6Al-4V, indicating a high level of superheat (~50%). Such a superheated melt pool should consist of density and surface tension gradients, and thus free convective and Marangoni-type currents should exist, respectively, within and along the surface of the melt pool. Due to this flow, alloy

solutes will be transported and rearranged within a matter of microseconds; in addition, contaminants and inert gas may be trapped within the dynamic melt pool. The superheated melt pool is more prone to unstable morphologies, splashing and more [11,114], which can lead to improper fusion and/or pore formation at intermittent locations along a track [44,115,116]. At these elevated liquid temperatures, amounts of the Ti-6Al-4V alloy powder may vaporize and vapor recoil can occur [114,117]. Note that the predicted peak temperatures should be slightly less due to the melt pool convective transport not being accounted for through use of an accurate effective thermal conductivity. Vapor recoil, natural convection eddies, Marangoni convection and instability, all contribute to the melt pool effective thermal conductivity, and thus, should be considered for more accurate temperature predictions.

Peak temperatures experienced along the first layer of the Ti-6Al-4V parallelepiped during fabrication of its second layer (layer immediately above the first layer) were found to vary between 1700 ºC and 1800 ºC for all simulations performed. Since the maximum melting temperature of Ti-6Al-4V is ~1660 ºC, portions of the first layer will re-melt while the next layer is fabricated. These remelting temperatures will influence fusion behavior of the layer set atop of it, while the solidification behavior of the remelted layer will be influenced by the cooling rates along the new layer. The temperature potential between the new and remelted layer will support residual stress formation upon final fusion. Note that peak temperatures experienced during fabrication of the first and second layers were found to be similar, indicating that melt pool peak temperature may be near independent of layer number for layers near substrate.

The melt pool temperature as predicted from continua-based FEM provides an indirect means to assess conditions conducive for pore formation, lack of fusion and vaporization. Per use of parameters/conditions reported by Vilaro et al. [113], the simulation results indicate a relatively

hot, scan/layer-independent melt pool in excess of 1000 ºC its liquidus. These conditions may be conducive for melt pool instability, which can then promote mechanisms for pore formation and lack of fusion. The existence of pores within AM Ti-6Al-4V has proven detrimental to its fatigue behavior, as they serve as stress risers and crack initiation sites [5,118–121]. Any lack of fusion is typically aligned perpendicular to the part build direction (in this case, z), and this introduces a high degree of mechanical anisotropy [4,50]. Hence, control of melt pool temperature may prove beneficial in reducing pore formation; however, the melt pool temperature must remain sufficiently high as to guarantee effective layer-to-layer fusion. Scan planning for ML-PBF should be cognizant of relative distance between melt pools as to ensure that any elevated powder bed temperatures do not drastically affect melt pool wetting behavior, as this can lead to regions of unique microstructure.

5.3. Cooling Rates

Local cooling rates are important to quantify, and to design for, as they drive microstructure formation and evolution immediately upon the solidification of the melt pool. To estimate the effect of scan strategy and number of lasers on cooling rates during PBF, an average of all maximum cooling rates extracted at points P1-P16 for each M^{th} layer, i.e. AMCR_M, was determined for all simulations using:

$$\text{AMCR}_M = -\frac{1}{16}\sum_{i=1}^{16}\left(\min\left[\frac{\partial T_i}{\partial t}\right]\right) \tag{4.1}$$

The uniformity in AMCR, and thus cooling rates, across a layer can influence the homogeneity of the final microstructure of the as-printed part. To quantify this uniformity, a standard deviation of local, maximum cooling rates for a given layer, i.e. the SDCR_M, was found using:

$$\mathrm{SDCR}_M = \sqrt{\sum_{i=1}^{16}\left(-\min\left[\frac{\partial T_i}{\partial t}\right] - \mathrm{AMCR}_M\right)^2 \Big/ 15} \tag{4.2}$$

The AMCRs and SDCRs corresponding to S1-S13 for the first and second layers are shown graphically in Figure 5.5. It may be seen that, in general, $\mathrm{AMCR}_1 > \mathrm{AMCR}_2$, for all scan strategies investigated due primarily to the heat capacitance of the substrate in which the first layer of powder is initially deposited and sintered. The second layer of powder cools off less quickly (by ~80%) since the thermal resistance of the first layer of solidified material decreases the heat transfer rate from the HAZ to the substrate. The AMCR for all simulations investigated is on-the-order of 10^6 ºC/s (or ~1 ºC/µs). The trends in AMCR were found to be similar for both layers investigated; however, the SDCR trends were not consistent for both layers. Note that although the first layers are typically sacrificial upon completion of PBF, their thermal response are of interest to ensure quality support structures for the non-sacrificial layers of the final part. The maximum cooling rate extracted from each point, P1-P16, along with its AMCR and SDCR, for the first and second layers, are provided in the Appendix as Tables A1 and A2, respectively.

Figure 5.5 indicates that as the number of lasers increases, the AMCR generally decreases, since the amount of energy delivered to the powder bed and part increases regional temperatures (i.e. pre-heat). Higher cooling rates were achievable using the LIP-0, single-laser PBF process with tracks parallel to the part's longest edge and swept in the Y+ direction. Lower cooling rates were achieved using the S9, S10 and S13 strategies – which all employed 4 lasers and LIP > 1. As track lengths were reduced via island division and/or sweeping tracks along the longest edge of the part (with tracks parallel to the shortest edge), the cooling rates generally decreased. Introduction of more islands and/or lasers generally decreases maximum cooling rates. Comparing S4, S9 and S12, which all employ the quadrant IDS and 4 lasers, but consist of different track

sweep directions, i.e. Y+, X+ and mixed, respectively, it is evident that the cooling rate decreases when tracks are swept along the part's longest edge.

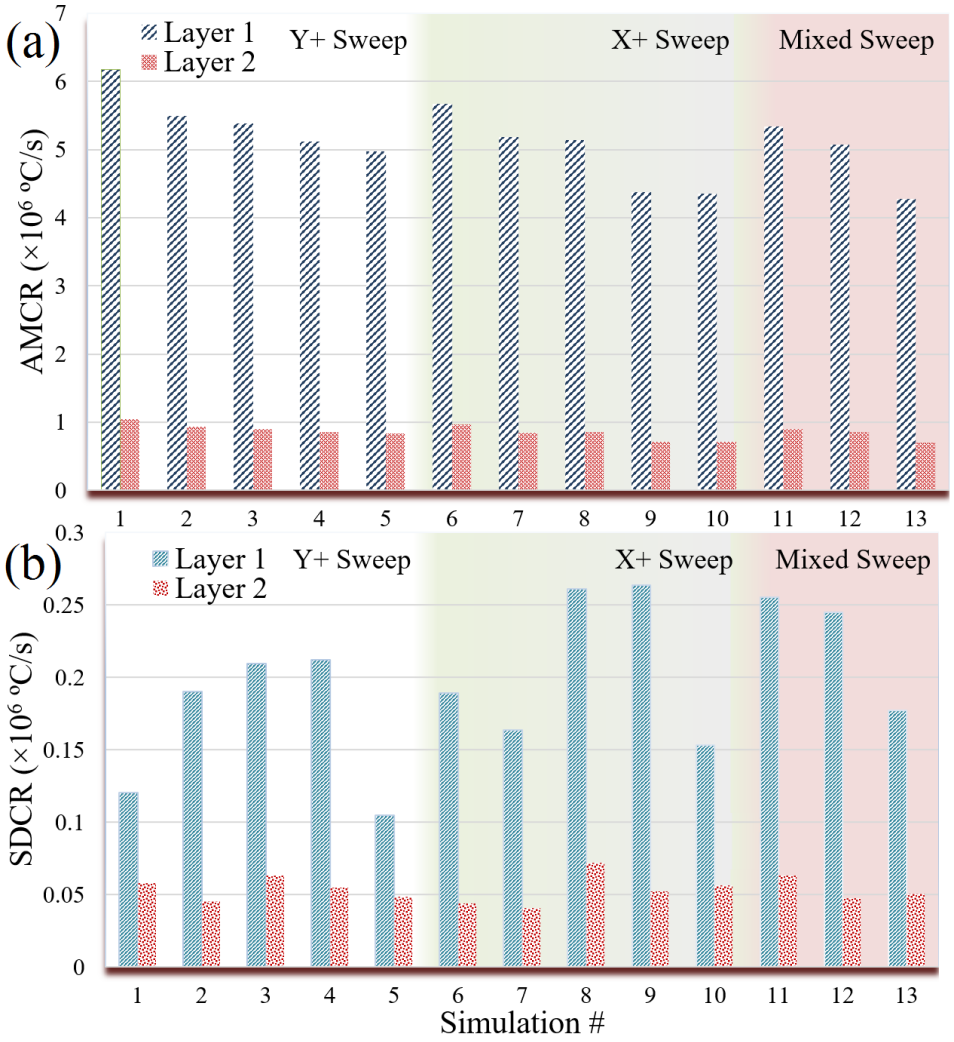

Figure 5.5 - (a) Average, maximum cooling rate (AMCR) and its (b) standard deviation (SDCR) with respect to first and second layers of Ti-6Al-4V parallelepiped during its manufacture via L-PBF/ML-PBF using scan strategies S1-S13.

The relative distance between melt pools during layer fabrication may not have a significant effect on maximum cooling rates. As shown in Figure 5.3, S12 provides for time-varying relative distances between island melt pools, while for S4, the melt pools maintain a constant distance relative to each other; however, in both cases, the AMCRs are similar. Although the AMCR may be more independent of relative melt pool motion (at least for the scan patterns

investigated herein), the cooling rates experienced during S12 are less homogeneous over the layer as evidenced by its higher SDCR. Employing a mixed sweeping strategy, in general, will increase the SDCR of a layer. Per Tables A1-A2, cooling rates are generally highest at the start of a track and can decrease along the track length due to heat accumulation effects.

The effect of IDS on layer cooling rates is best evidenced by comparing S4 and S5 with S9 and S10. Although the 'quadrant' and 'fourths' division schemes provide for similar AMCRs, the SDCRs are significantly different. For both the X+ and Y+ track sweeping directions, the fourths IDS can reduce the SDCR by approximately 50% relative to the quadrant IDS. This indicates that more homogeneous microstructures can be obtained by employing IDSs consisting of islands aligned successively next to each other, in a single row and with border lines parallel to track scan directions, as opposed to IDSs consisting of islands 'split' by intersecting border lines at the center of the layer. The sweep direction proves important when employing sub-islands for a single laser; meaning, when going from LIP-0 to LIP-1 (e.g. S1 to S2 or S6 to S7), the SDCR can be better controlled when employing islands that have tracks swept parallel to the part's longest edge. Layers fabricated using a single laser and a single sub-island, with tracks parallel to the longest edge, proved to have the highest cooling rates while also having a relatively low SDCR. Increasing the number of lasers, as evidenced by comparing S2-S4 (or S7-S9), in which each of these simulations employ either 1, 2 or 4 lasers, respectively, will decrease AMCR, but the decrease going from 2 to 4 lasers is significantly less drastic.

Figure 5.6 shows the maximum cooling rates measured at P1-P16 along the first two layers of the Ti-6Al-4V parallelepiped for S1, S6 and S13 in the form of radar charts. These radar charts provide a unique means for visualizing homogeneity in maximum cooling rates with respect to each layer; assuming the discrete 'measuring points', i.e. like P1-P16, are arranged in an

appropriate manner. For example, using the P1-P16 scheme provided in Figure 5.2, generated radar charts appear more circular in shape when the maximum cooling rate varies less with location along the layer for a given scan pattern; while they appear more 'star-shaped' with increased inhomogeneity. For all simulations, the maximum cooling rate varies with location along the layer (i.e. no perfect circle exists). In general, homogeneity in maximum cooling rates is higher for the first layer relative to the second layer, and this can be attributed to the thermal capacitance of the substrate. Increasing the LIP order will dissolve a 'perfect circle', i.e. similar to S1, to a more staggered shape since more variation and fluctuation in cooling rate will exist due to more lasers and sub-islands. Low LIP scan patterns allow each layer to possess a thermal response less influenced by other lasers.

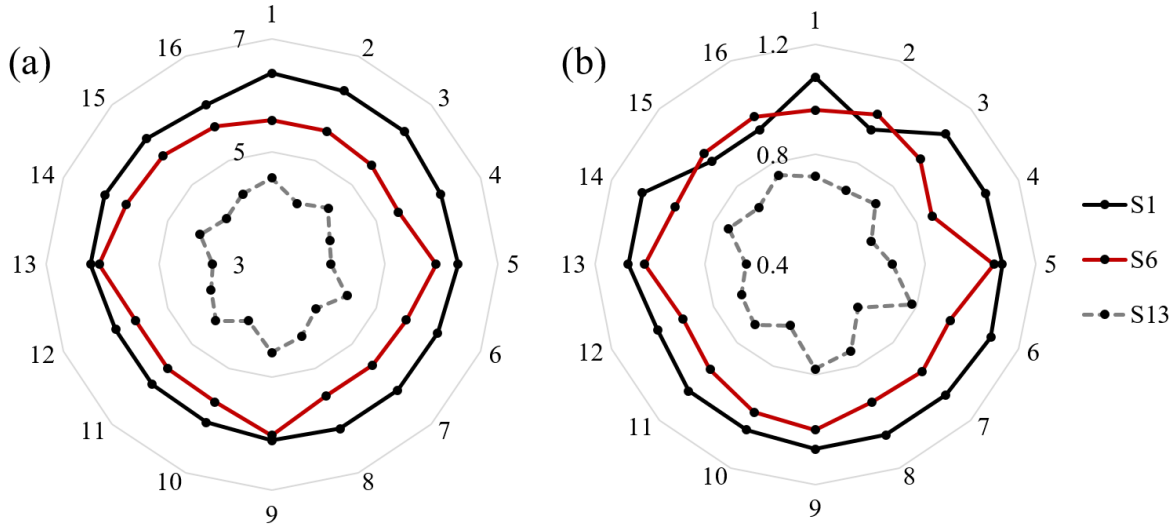

Figure 5.6 - Radar charts showing maximum cooling rates (in units 10^6 ºC/s) measured at points P1-P16 (circumferential markings) during manufacture of the Ti-6Al-4V parallelepiped following scan strategies described in S1, S6 andS13 (star/circular profiles) for the (a) first layer and (b) second layer.

Based on the results herein, Ti-6Al-4V will cool very rapidly from temperatures well above its β-transus (~995 ºC) during L-PBF. Microstructural phase transformations are then highly influenced by the magnitude and time-rate-of-change of local cooling rates. Many have verified

the dominance of the martensite phase in PBF Ti-6Al-4V [43,91,122–124], and this can be attributed to the very fast cooling rates encountered upon solidification of the melt pool, as confirmed herein as ~10^5-10^6 ºC/s. Maintaining these high cooling rates during PBF will preserve the amount of martensite in the final Ti-6Al-4V material. Elevated powder bed temperatures can promote α' martensite decomposition, while sustained temperature gradients can lead to a complete α+ β phase. [122]. Although the current work has focused on maximum cooling rates, the sustained cooling rates inherent to ML-PBF should be lower relative to single-laser PBF due to the more elevated powder bed temperatures. Thus, increasing the number of lasers for PBF may promote more martensite decomposition and a final Ti-6Al-4V material with less martensite. The various scan patterns will influence the elongated grain growth directions within the Ti-6Al-4V material. As shown by Thijs [43], the elongated grains will follow the direction of the conductive heat flux. Thus, layers fabricated using scan patterns that provide for relatively high SDCRs and time-variant relative motion of melt pools, i.e. S11-S13, will possess more anisotropic microstructure.

5.4. Temperature Gradients

In general, parts made via L-PBF experience very high temperature gradients, and such gradients can drive residual stress formation [25,69,122]. The rapid, localized heating/cooling of the melt pool during L-PBF promotes material expansion and contraction at non-equal rates, thus forming micro- and macro-stresses within the solid part volume. In addition, these thermal stresses can lead to the occurrence of segregation phenomena and the presence of non-equilibrium phases [43]. Residual stress can prove detrimental to the fatigue behavior of Ti-6Al-4V during its application [5,125]. The temperature-dependent properties of Ti-6Al-4V are somewhat supportive to residual stress formation during PBF [32]. Relative to many other common AM metals, Ti-6Al-

4V has a low thermal diffusivity, resulting in more thermal energy build-up as opposed to its transport, and thus, over the same time window, Ti-6Al-4V will have higher local temperature gradients.

Herein, local temperature gradient magnitudes are extracted and used for predicting the existence of thermal stress, which can lead to, most often, tensile residual stress in the part [28]. An average maximum temperature gradient magnitude from points P1-P16 corresponding to the M^{th} layer, i.e. AMTG_M, was determined for S1-S13 using:

$$\text{AMTG}_M = \frac{1}{16}\sum_{i=1}^{16}(\max\|\nabla T_i\|) \tag{5.3}$$

In addition, the homogeneity of AMTGs along a layer was quantified by taking their standard deviation, i.e. the SDTG_M:

$$\text{SDTG}_M = \sqrt{\sum_{i=1}^{16}(\max\|\nabla T_i\| - \text{AMTG}_M)^2 \Big/ 15} \tag{5.4}$$

The AMTGs and SDTGs for each layer during S1-S13 are shown in Figure 5.7. Similar to trends observed for cooling rates, the AMTGs and SDTGs are generally lower during fabrication of the second layer which has less heat transfer to the substrate. The AMTG is high, on-the-order of 20-100 ºC/µm for all simulations. In addition, the AMTG varies along the layer; being higher at points near the start of a track and lower toward the end of a track, primarily due to heat accumulation effects [45]. The magnitude of the temperature gradient also decreases with laser sweep direction; meaning, as the part grows in volume, and the surrounding media accumulates more heat, later tracks will experience lower AMTGs. This confirms that regional preheat can reduce residual stress formation, as local temperature gradients become less severe during final

track fabrication. All maximum temperature gradient magnitudes at P1-P16 during fabrication of the first layer and second layer are summarized in Table A3 and Table A4, respectively.

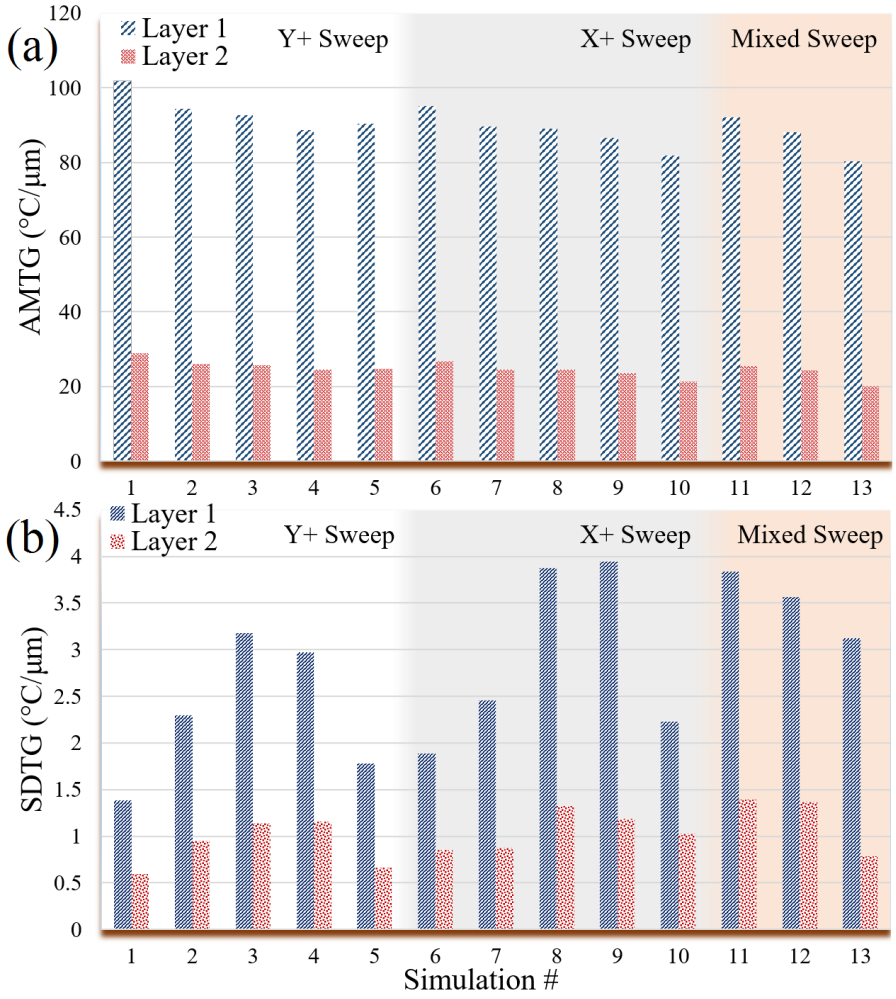

Figure 5.7 - (a) Average, maximum temperature gradient magnitude (AMTG) and its (b) standard deviation (SDTG) with respect to first and second layers of Ti-6Al-4V parallelepiped during its manufacture via L-PBF/ML-PBF using scan strategies S1-S13.

By comparing AMTGs in Figure 5.7 (a), it may be concluded that employing more lasers via ML-PBF can reduce the magnitudes of temperature gradients by ~5%. A ~10% reduction in AMTG is achieved by employing the 'fourths' IDS instead of the 'quadrant' IDS, indicating the importance of island geometries relative to layer geometry. Building layers in a sequenced island approach, i.e. LIP-1/LIP-3 decreases the AMTG (i.e. S1 vs. S2, S6 vs. S7 and S12 vs. S13) for

both layers. Lower AMTGs exist when sweeping lasers in the X-direction, along the longest dimension of the parallelepiped, with tracks parallel to the shortest edge. By comparing the results from S1 and S6 in Figure 5.7, scan patterns with smaller tracks (S6) result in lower temperature gradients as compared to patterns with longer tracks (S1). This is due to the time interval between the fusion of neighboring points on an island with shorter tracks being smaller than that for islands with longer tracks. Longer time intervals allow heat to diffuse, while shorter time intervals result in more retained heat and thus higher temperature. The synchronous, mixed-sweeping technique investigated (i.e. P=4) demonstrates to provide for the lowest AMTG. Li et al. [28] demonstrated similar results for single-laser, mixed-direction/island scanning.

The SDTG provides insight into the spatial uniformity of AMTG and a means for characterizing the complexity of a residual stress distribution. Figure 5.7 (b) provides the SDTGs for S1-S13, while Figure 5.8 provides radar charts of the AMTGs. Since the scan strategy related to S1 was found to provide the lowest SDTG, its radar chart possesses a more circular shape, while S13, has a more staggered profile due to its higher SDTG. In general, strategies providing for lower AMTGs tend to have higher SDTGs. For example, S1, S6 and S13 provide for the highest AMTG for their respective sweep strategy, while in contrast, these same strategies possess the lowest SDTG in their category. Lower SDTGs, unlike the AMTG, were found to exist when sweeping lasers in the Y-direction, along the shortest dimension of the parallelepiped, with tracks parallel to the longest edge. Mixed-sweeping techniques demonstrated to provide the highest SDTG when using one or four lasers.

Results suggest that increasing the total number of sub-islands (e.g. S1 to S2 to S13) will decrease the AMTG and increase the SDTG of a layer. Utilizing an IDS cognizant of the part shortest edge can provide a significant reduction in SDTG. For example, the ‘fourths’ IDS appears

to be more appropriate for the multi-laser approach, since its SDTG is comparable to that experienced for a unit-island layer (LIP-0). The mixed sweep approach for accomplishing single- (i.e. S11) or multi-laser PBF (i.e. S12 and S13) provides less homogeneity in AMTGs; however, the lowest overall AMTG was accomplished using S13. The mixed-sweep strategy (i.e. SP-E, SP-H), in contrast to both the X and Y scan strategies (i.e. SP-A through SP-D), possesses an SDTG that decreases as more islands and lasers are introduced.

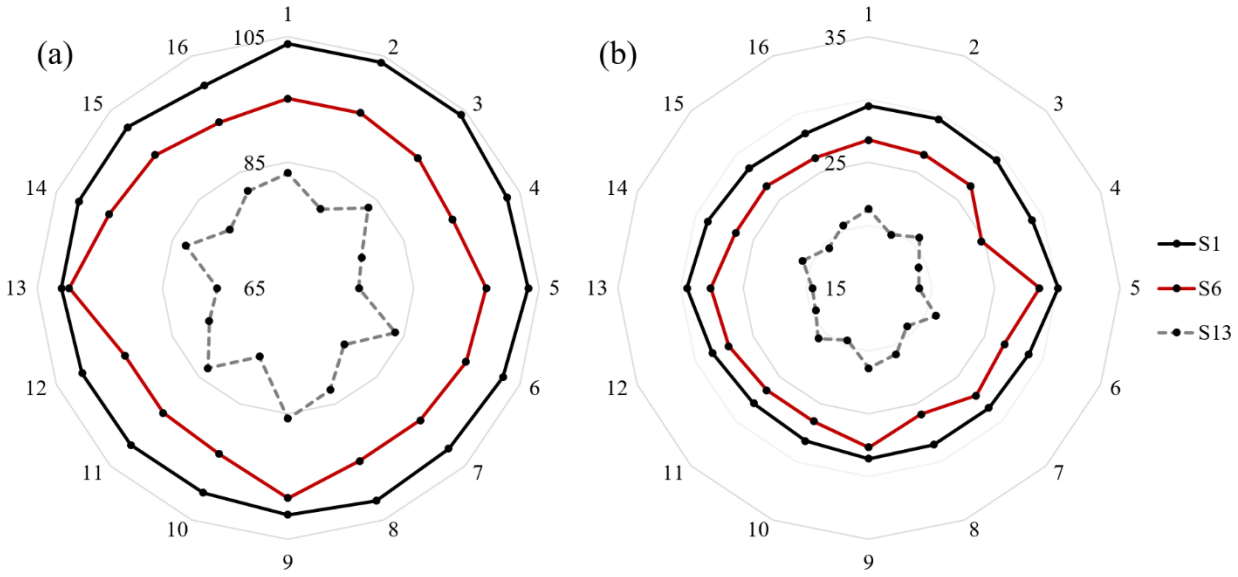

Figure 5.8 - Radar charts showing maximum temperature gradient magnitudes (in units ºC/µm) measured at points P1-P16 (circumferential markings) during manufacture of the Ti-6Al-4V parallelepiped following scan strategies described in S1, S6 and S13 (star/circular profiles) for the (a) first layer and (b) second layer.

Results demonstrate that scan strategies consisting of melt pools with time-variant relative distances can lead to higher STDGs. Figure 5.9 presents the response of local temperature and its gradient as a Q1 laser (see Figure 5.1) passes a point centered on its respective island, for S1, S4 and S9. Note that the time to complete the presented islands ranges from 100 ms (for S1 and S4) to 400 ms (for S9). From Figure 5.9 (a) – (c), it may be seen that the peak temperatures experienced are similar. There are slight temperature perturbations before and after local temperature spikes due to the passing of the laser as it scans neighboring, adjacent tracks. These temperature

perturbations do not exceed the liquidus temperature of Ti-6Al-4V, so the center region of the track does not remelt. The first temperature perturbation is lower in magnitude than that of the second perturbation due to regional heat accumulation effects. The first temperature perturbation is more pronounced for the S9 strategy (4 lasers, X+ sweeping, quadrant IDS) due to the shorter track lengths providing for a lower track-to-track time interval and more regional preheating. The cooling rates immediately after the laser passes the point-of-interest are much higher than those experienced after the second temperature perturbation. After the adjacent track is finished, the point-of-interest experiences a semi-continuous cooling rate on-the-order of 1000 ºC/s for the remainder of the layer building process. This indicates that conditions are highly favorable for martensite retention within Ti-6Al-4V parts fabricated by single- or multi-laser PBF.

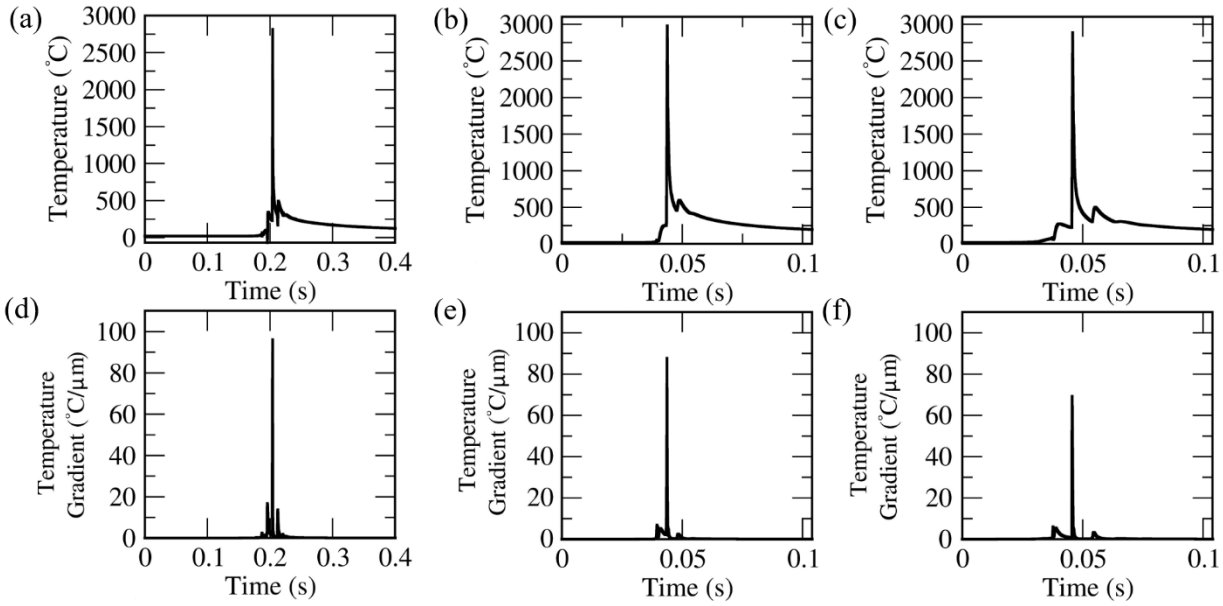

Figure 5.9 - Temperature response for (a) S1, (b) S4, and (c) S9, as well as the temperature gradient magnitude response for (d) S1, (e) S4, and (f) S9, as the Q1 laser passes its island center.

As shown in Figure 5.9 (d) – (f), the local temperature gradient magnitude, at the center of the Q1 island for the S1, S4 and S9 scan strategies, also varies with time, LIP and scan direction (i.e. track lengths). The local temperature gradient magnitude at the point-of-interest achieves

maximums on-the-order of 60-90 ºC/µm, with the lowest peak occurring for S9 – the simulation employing 4 lasers (LIP-2) and shorter tracks parallel to the part's shortest edge. These high, instantaneous temperature gradients support the formation of tensile residual stress in the center of the island; however, the scanning of tracks immediately atop the point-of-interest may elevate its temperature to liquidus, thus 'erasing' any encumbered residual stress. The instantaneous temperature gradients experienced by the point-of-interest during the PBF of the layer directly above it will be less in magnitude, by ~30%, due to less heat penetration. Hence, the free surface of the final parts should consist of higher residual stress. The difference between peak temperatures of adjacent layers (of thickness = 30 µm) was found to be ~1000 ºC for many of the scan strategies investigated, and this confirms a layer-wise temperature gradient (Z direction) around 30 ºC/µm. There are perturbations in temperature gradient magnitude when the laser scans the neighboring tracks. Since the track scanned before the point-of-interest's track provides for a bigger temperature difference, as less preheat is available, the first perturbation is higher in magnitude. Note that the highest temperature gradient magnitude was measured to occur for S1 (LIP-0) which consisted of a single laser, a single island, and long tracks parallel to the part's longest edge. Increasing the laser number to 4, i.e. S1 to S4, results in a local decrease in temperature gradient magnitude by ~10%. Based on Figure 5.9 (d) - (f), it appears that local residual stress formation is more sensitive to track scan directions and not number of lasers employed, as evidenced by comparing the percent decrease between S1 and S4, and the S1 and S9.

The local temperature gradient will depend on the scan direction of the employed laser(s). As shown in Figure 5.10, the temperature gradient inherent to the point-of-interest during S1 has a high Z-component and a low X- and Y-component. It was consistently found that the

temperature gradient parallel to the laser scan direction is the lowest, and this agrees with the results of Mercelis et al. [25] and Li et al. [28]. Unidirectional, single-island scanning similar to S1 will have more points along the layer experience a similar thermal history, and thus, its SDTG will be low and the residual stress along the X and Y directions will be more uniform, and this agrees with the results presented by Li et al. [28], as well.

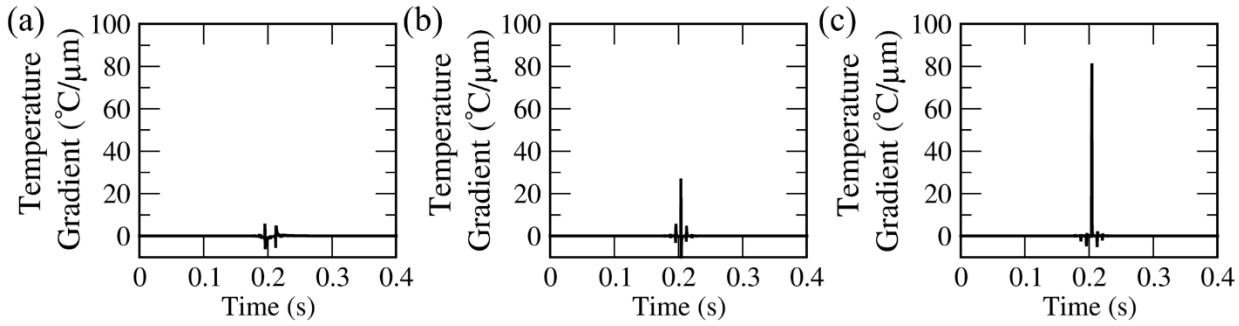

Figure 5.10 - Response of local temperature gradient as Q1 laser passes center of island during S1: (a) X-component, (b) Y-component, and (c) Z-component.

CHAPTER 6

Modeling the Shielding Gas

6.1. Gas Flow and Temperature Fields

Figures 6.1 (a) - (b) show the velocity distribution of the argon shielding gas within the representative L-PBF chamber along the center of the track in the x-z plane while the laser is at the middle of the track (halfway complete with the single-track layer). In all cases the inlet gas velocity is 8 m/s. As shown in Figure 6.1 (a), the gas flow has the same direction as the laser, while in Figure 6.1 (b), the gas is moving in the opposite direction of the laser. The velocity boundary layers are clearly visible along the top surface of the chamber and along the powder bed at the bottom of the chamber. The no-slip velocity condition is verifiable based on the zero-magnitude velocity near the powder bed/gas interface and top surface wall. The argon speed is slightly lower near the HAZ regardless of laser/gas-flow directions due to its lower density in this region. The boundary layer along the powder bed is more defined in shape, and slightly thinner, relative to the top boundary layer due to gravity effects. The boundary layer thickness depends on whether it is in the processed region, in which the powder has been melted and solidified, or non-processed (powder bed) regions. Results verify that the top and bottom boundary layers do not merge and that the flow may be approximated as external cross-flow over a flat plate when assuming a smooth powder bed continuum.

Figures 6.1 (c) – (d) show the temperature distribution of the argon gas when the inlet speed is 8 m/s. For Figure 6.1 (c), gas flow is in the same direction as the laser, while in Figure 6.1 (d),

the gas flow is in the opposite direction of the laser. As expected, the temperature of argon in vicinity to the melt pool (i.e. processed area) is much higher due to convection heat transfer. In regions just above the melt pool, argon reaches temperatures as high as 800 °C. Argon temperatures above the processed region remain elevated and a transient, thermal boundary layer is evident. Argon temperatures outside this boundary layer are essentially equal to the input/supply temperature. The thermal boundary shape depends on the laser/gas-flow directions. For the case when the gas and laser are moving in the same direction, the thermal boundary layer is 'pushed' past the melt pool and protrudes into the unprocessed region of the track, thus allowing argon-to-powder convection heating. In other words, due to the speed of the gas, the powder bed will be heated even before coming in contact with laser. This 'pre-heated' argon will also contribute to the bulk heating of the thermal boundary layer as the processed length of the track increases. For the opposite laser/gas-flow direction case, it may be seen that the thermal boundary layer has a more rounded leading edge that does not protrude into the unprocessed region of the powder bed as much. The thermal boundary layer for the opposite-direction case is somewhat thicker, while the same-direction thermal boundary layer has a more defined profile that becomes thinner, more quickly, in processed regions further from the melt pool.

Temperature contours of the simulated melt pool in the XY and YZ plane are shown in Figure 6.2 (a) – (b), respectively. Results suggest that a relatively shallow and long melt pool exists for the selected material (Ti-6Al-4V), process parameters and operating conditions - the length, width and depth of the melt pool are estimated to be 250 μm, 115 μm and 55 μm, respectively. The width and depth were estimated based on the Ti-6Al-4V liquidus temperature contour. The length of the melt pool is longer along the laser direction as compared to the perpendicular direction. Simulation results indicate a highly-localized, peak temperature around 3080 °C which

is almost twice the liquidus temperature of Ti-6Al-4V. The trailing mushy zone possesses a length approximately twice, to 3x, that of the melt pool depth. Note that the gas flow direction slightly impacts the trailing edge of the melt pool (and HAZ) width. As shown in Figure 6.2 (a), the melt pool (and HAZ) is wider and slightly shorter in the case of opposite gas/laser directions.

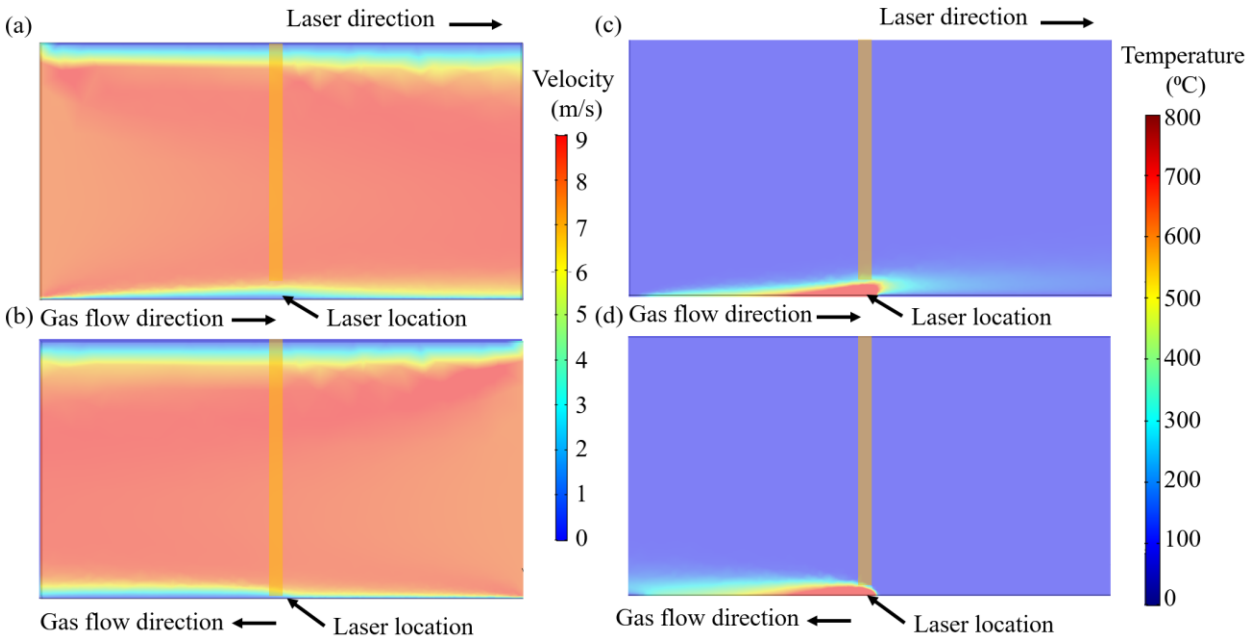

Figure 6.1 - Velocity magnitude (i.e. speed) of argon inside the chamber with 8 m/s inlet with laser and gas moving (a) in same direction, (b) in different directions. Temperature distribution of argon inside the chamber with 8 m/s inlet with laser and gas moving (c) in same direction, (d) in different directions.

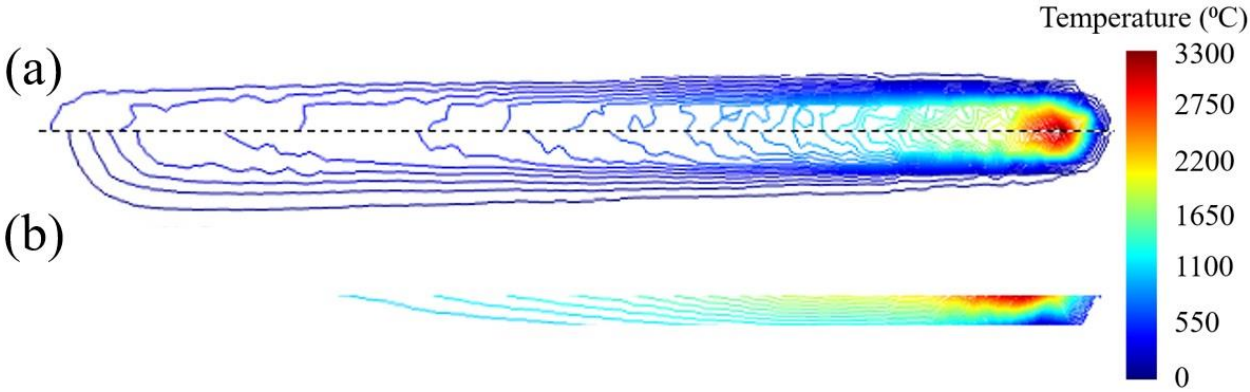

Figure 6.2 - Track temperature distribution (scan speed = 1250 mm/s, argon speed = 4 m/s) along (a) XY plane with gas and laser in same direction (top) and opposite directions (bottom) and (b) temperature distribution along YZ plane with gas and laser in same direction.

6.2. Non-Dimensional Numbers

The thermophysics inherent to L-PBF can be quantified and understood via pertinent non-dimensional numbers/groups as discussed in Section 2.4. Here, the non-dimensional numbers are provided as a function of time for the entire L-PBF of a track at a point, i.e. measurement location, located halfway along the track. Figure 6.3 shows the effects of gas direction and speed on its local Reynolds and Rayleigh numbers. With respect to the Reynolds number, it may be seen that the flow within the chamber is laminar, i.e. $Re \leq 5 \times 10^5$. At the trailing edge of the track and substrate, local Reynolds numbers are $O(10^3)$ and $O(10^4)$, respectively. Gas flow direction has no meaningful effect on the Reynolds number due to symmetry of the track and chamber; however, the Rayleigh number is greatly affected. When the laser and gas are moving in opposite directions, local Rayleigh numbers are higher relative to when they are moving in the same direction. This implies that when the laser and gas are moving in opposite directions, free convection becomes more important relative to conduction. Another interesting phenomenon observed is that, even before the laser hits measurement location for the case in which the laser and gas are moving in same direction, the Rayleigh number steadily increases. When the laser and gas are moving in opposite directions, the Rayleigh number is not effected until after the laser hits the measurement location. This phenomenon occurs due to the pre-heating of the measurement location by the hot argon which is 'pushed' downstream from the processed region. As the gas speed increases, the local Rayleigh number near the melt pool increases indicating more unstable free convective flows in this area during laser irradiation. In all cases investigated, the Rayleigh number is on-the-order of $2\text{-}3 \times 10^3$ during laser irradiation above the melt pool and then sharply decreases once the laser passes. This sharp decrease indicates that buoyancy-driven flow is only dominant prior and during

laser irradiation of a point. The Rayleigh number 'recovers' and steadily rises with time after the laser moves away from the processing point.

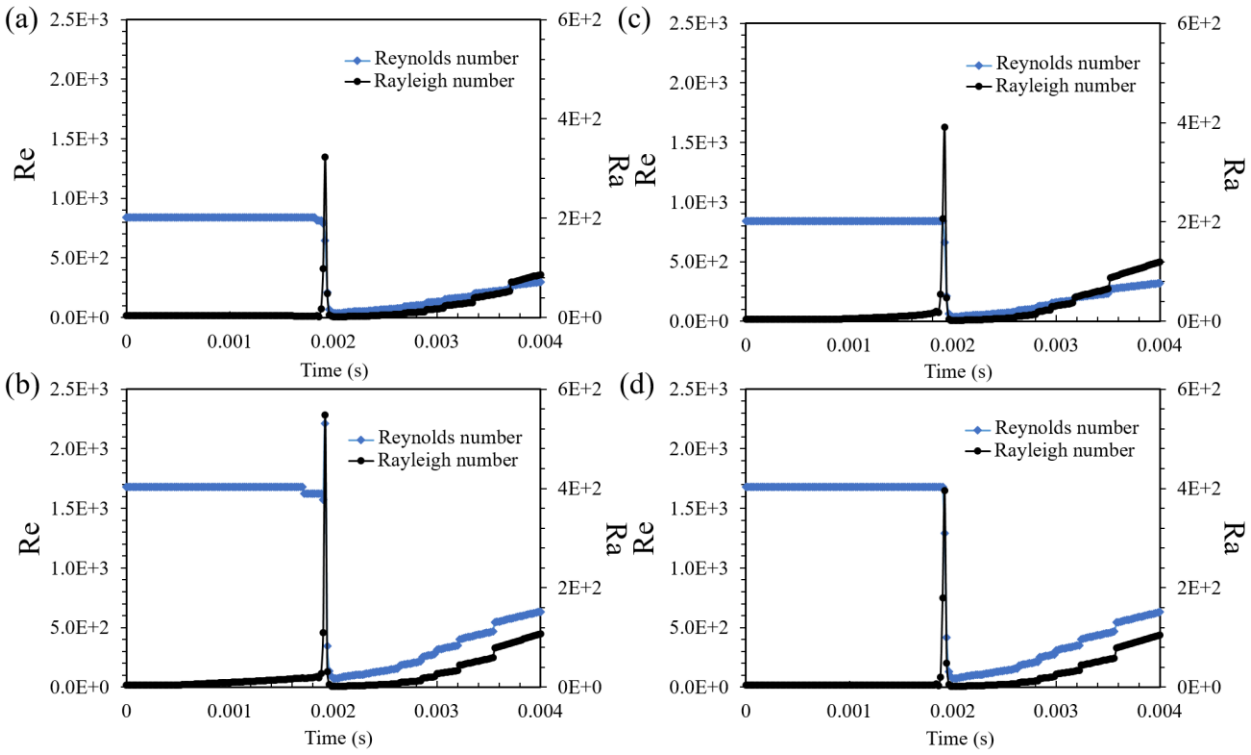

Figure 6.3 - Reynolds and Rayleigh numbers at the middle of track when gas and laser are moving in same direction and the speed of argon is (a) 4 m/s or (b) 8 m/s. Reynolds and Rayleigh numbers at the middle of track when gas and laser are moving in opposite directions and the speed of argon is (c) 4 m/s or (d) 8 m/s.

Figure 6.4 displays the Richardson number - a measure of free convection to forced convection. As shown in Figure 6.4, the Richardson number is near zero indicating that, although argon density variation around the melt pool is considerable, buoyancy is not a major transport mechanism relative to forced convection for the majority of track. The Richardson number becomes nearly four times higher atop the HAZ during material processing indicating that during laser heating, local argon becomes very hot (~800 ºC) and thus buoyancy-driven flow becomes more prevalent in this region. Flow speed is the only factor that significantly affects bulk Richard number during L-PBF.

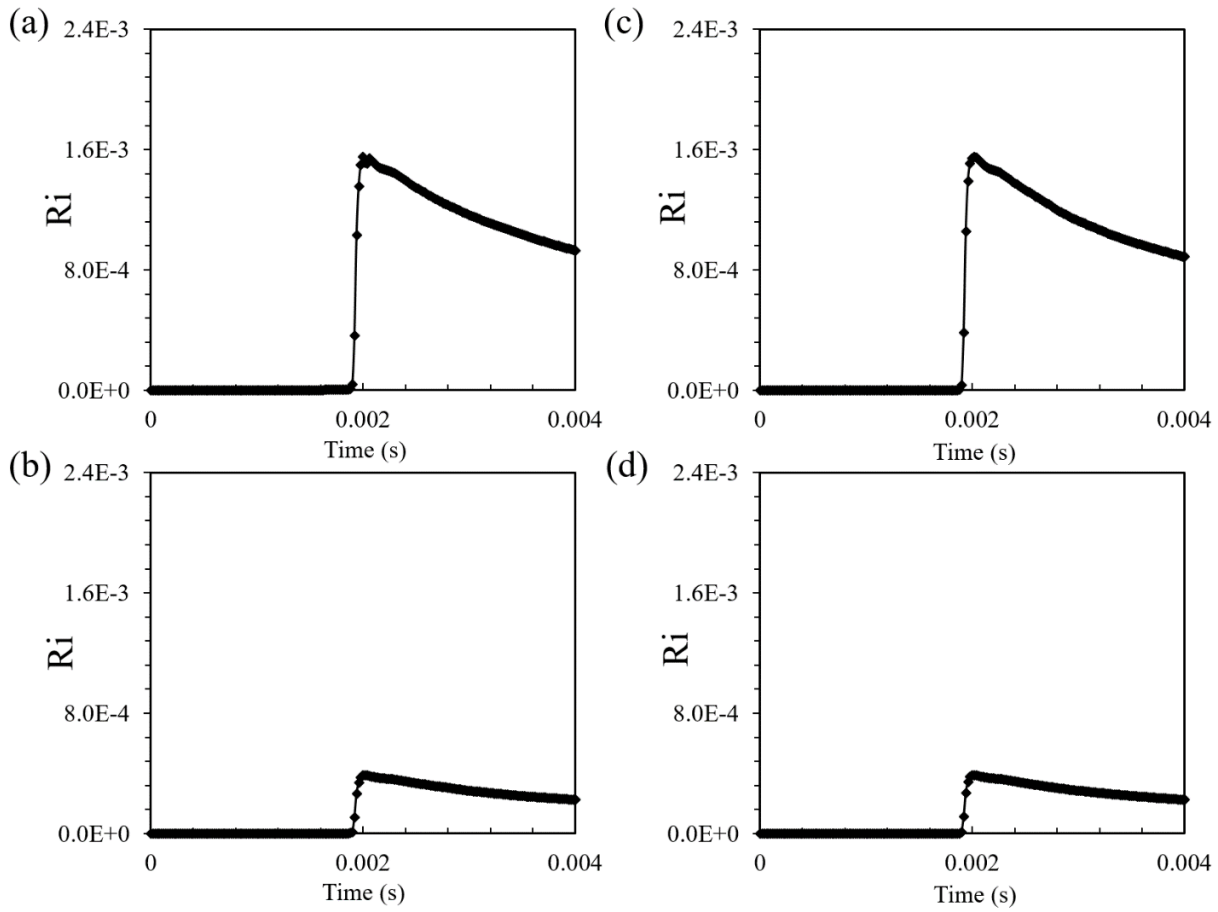

Figure 6.4 - Richardson number at the middle of track when gas and laser are moving in same direction and the speed of argon is (a) 4 m/s or (b) 8 m/s. Richardson number at the middle of track when gas and laser are moving in opposite directions and the speed of argon is (c) 4 m/s or (d) 8 m/s.

Figure 6.5 shows the Nusselt and Prandtl numbers at the center of the track during the simulated L-PBF conditions. It is observed that local Nusselt numbers depend on gas flow direction relative to laser direction. Nusselt numbers are generally higher when the laser and gas are moving in the same direction relative to when they are moving in opposite directions. For same-direction laser/flow configurations, maximum Nusselt numbers on-the-order of 3000 are obtainable during laser heating. Once the laser moves past the mid-point of the track, the Nusselt number drops very rapidly to values near $O(10^1)$. Interestingly, when the laser and gas move in the same direction, the Nusselt number steadily increases as the laser approaches the measurement

location at the middle of the track. This is attributed to the upstream thermal boundary layer (i.e. hot argon) coexisting at downstream locations. Preheated gas moves ahead of the laser due to the bulk gas flow direction, and this is confirmed in Figure 6.1. Increasing the speed of the flowing argon will increase heating Nusselt numbers due to increased forced convection. When the laser and gas move in opposite directions, the heating Nusselt number is much smaller and concentrated at the point of material processing. The local cooling Nusselt number is higher immediately after laser processing for opposite flow/laser directions. As shown in Figure 6.5, argon Prandtl numbers are lower before the laser reaches the measurement location. This indicates that heat transfer to the argon via conduction plays a bigger role after material processing – this is also evidenced by the lower Nusselt numbers during the cooling phase. The gas Prandtl number is relatively unaffected by the direction and speed in which the argon gas flows. This implies that the ratio of gas-wise conduction to convection heat transfer during L-PBF is near-independent of flow configuration and scan strategy when using argon.

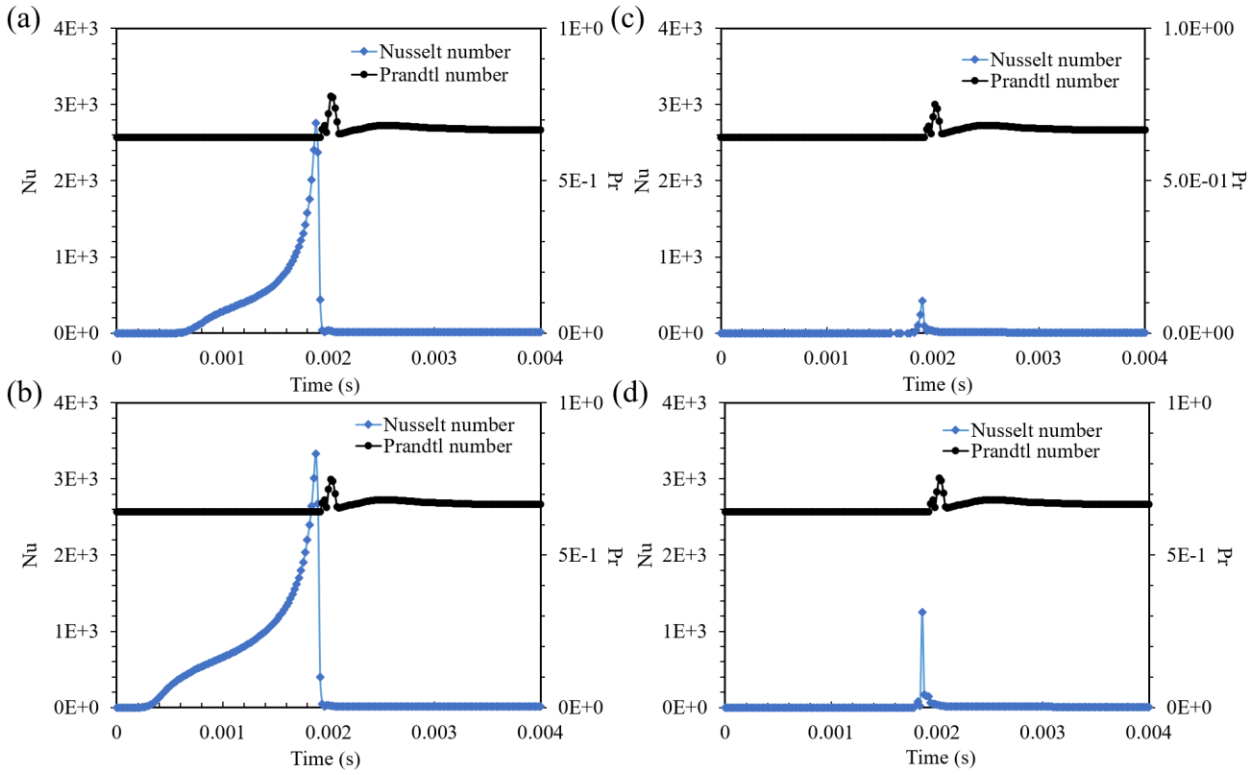

Figure 6.5 - Nusselt and Prandtl numbers at the middle of track when gas and laser are moving in same direction and the speed of argon is (a) 4 m/s or (b) 8 m/s. Nusselt and Prandtl numbers at the middle of track when gas and laser are moving in opposite directions and the speed of argon is (c) 4 m/s or (d) 8 m/s.

Figure 6.6 provides the process' Biot number at the mid-point of the track under the various investigated gas/laser configurations. The Biot number can be used as a measure of temperature uniformity in a convecting solid, with higher Biot numbers indicating more temperature variation within the solid. From Figure 6.6, it may be seen that, like the Nusselt number, the highest Biot number occurs during material processing when the gas and laser are moving in the same direction. Higher Biot numbers during the preheating phase of the same gas/laser direction configuration indicates that convection heat transfer has a stronger influence on temperature than conduction. Due to the Biot number's dependence on the heat transfer coefficient of argon, it increases as gas speed increases – indicating steeper temperature gradients in the HAZ. The Biot number typically ranges between 1 and 10 for the investigated L-PBF process – with higher Biot numbers existing during pre-heating and material processing phases. These relatively high Biot numbers indicate,

as expected, that the temperature gradients around the HAZ are significant. During the cooling phase, the argon gas temperature is much less and, due to heat transfer through the melt pool and solid, there is less heat to transfer to the moving gas. It may be seen in Figure 6.6 that a Biot number 'recovery' occurs during cooling – in which the Biot number temporarily increases as the melt pool solidifies and latent heat transfer dominates.

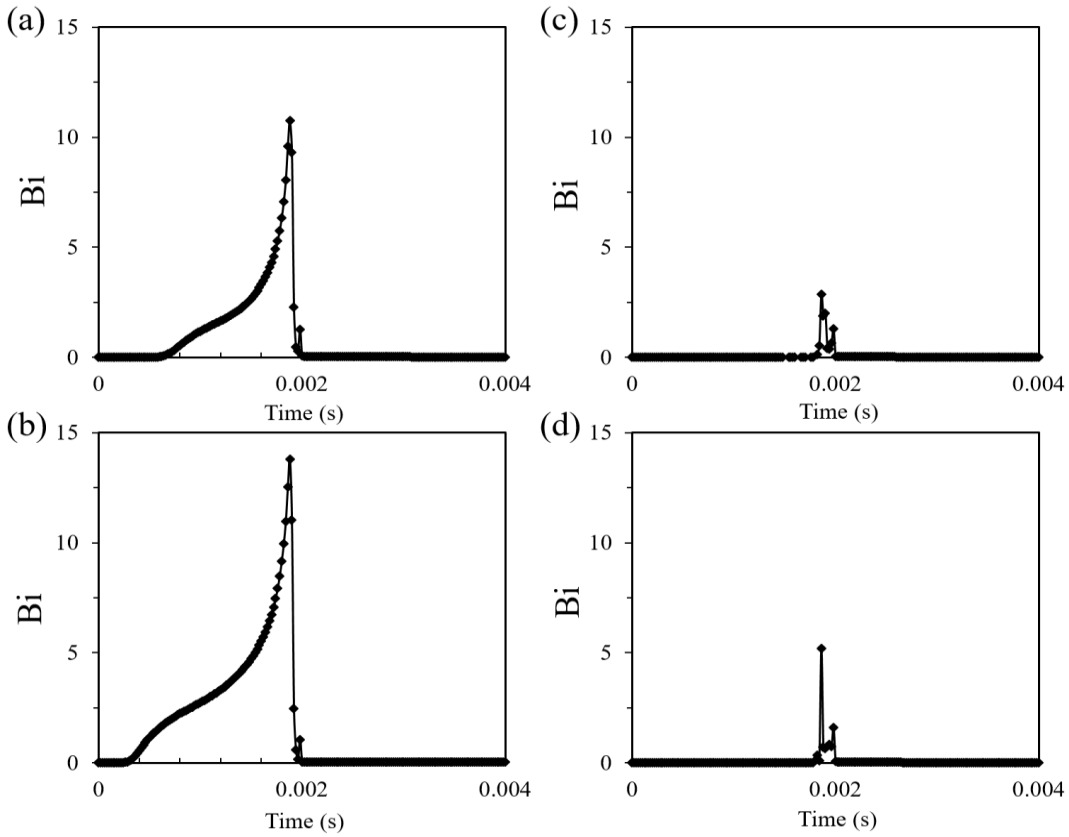

Figure 6.6 - Biot number at the middle of track when gas and laser are moving in same direction and the speed of argon is (a) 4 m/s or (b) 8 m/s. Biot number at the middle of track when gas and laser are moving in opposite directions and the speed of argon is (c) 4 m/s or (d) 8 m/s.

6.3. Gas Thermal Response of Melt Pool

Figure 6.7 presents the local temperature and temperature gradient response at the track's mid-point for the various gas/laser motion configurations investigated. It may be seen that the maximum temperature of the melt pool drops around 30 ºC (~ 1%) when the speed of argon

increases due to higher convection heat transfer rates. The maximum melt pool temperature is slightly lower (~20 ºC) when the gas and laser move in the same direction, again due to the convective heat flux becoming more prominent. Since the melt pool area is very small, i.e. ~ 8 x 10^{-9} m², any local changes in convective heat transfer result in only modest changes in maximum melt pool temperature. This same trend is observed with the local, absolute temperature gradient. The temperature gradient is approximately 15% lower when the laser and gas are moving in same direction relatively to when they move in the opposite direction. When the laser and gas move in the same direction, the un-melted region is pre-heated by the flow of heated argon, which helps reduce temperature gradients. It is observed that when the laser and gas are moving in the same direction, that the temperature gradient starts to increase when the laser approaches the measurement location, whereas when the laser and gas are moving in opposite directions it only increases when the laser is at the measurement location. In all cases, the temperature and temperature gradient decrease similarly with time after the laser moves from the mid-point of the track (i.e. during cooling). As the melt pool solidifies, the temperature gradient plateaus for a brief period due to the near-constant temperature experienced during latent heat transfer. This plateau is more defined, and level, when the laser and gas are moving in the same direction.

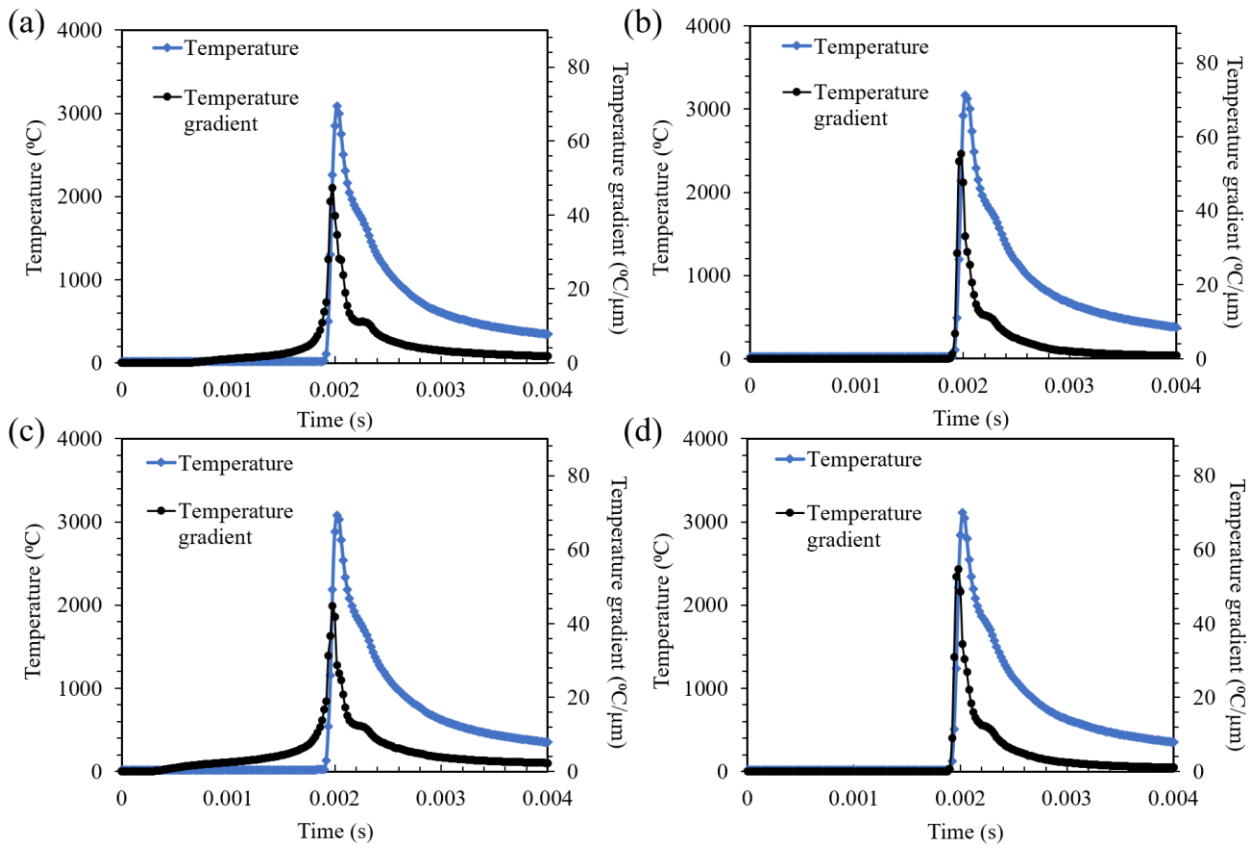

Figure 6.7 - Temperature and magnitude of temperature gradient at middle of track when gas and laser are moving in same direction and the speed of argon is (a) 4 m/s or (b) 8 m/s. Temperature and temperature gradient at the middle of track when gas and laser are moving in opposite directions and the speed of argon is (c) 4 m/s or (d) 8 m/s.

The gas flow and laser direction should affect the local melt pool temperature time rate of change (TTRC), i.e. heating/cooling rates. This is important since cooling rates (i.e. negative TTRCs) drive microstructure formation and evolution in metals. Figure 6.8 provides the local TTRCs at the mid-point during the L-PBF of the Ti-6Al-4V track. It may be seen that heating rates are generally higher than the cooling rates, with maximum heating rates around 50 x 10^6 ºC/s and maximum cooling rates around 10 x 10^6 ºC/s. When the laser is moving opposite to the gas flow direction at 4 m/s, the maximum cooling rate is approximately 10% higher than when they are moving in the same direction. This is attributed to the fact that the track is preheated during the same-direction scenario, and thus, the temperature potential between the heated argon and track is less. As the gas speed increases to 8 m/s, this percent difference decreases to ~3%. It may be

noticed that the cooling rate increases slightly during solidification of the melt pool (and mushy zone) – due to the latent heat of fusion, and this is evident by the 'kink'/'bump' in the cooling regime shown in Figure 6.8.

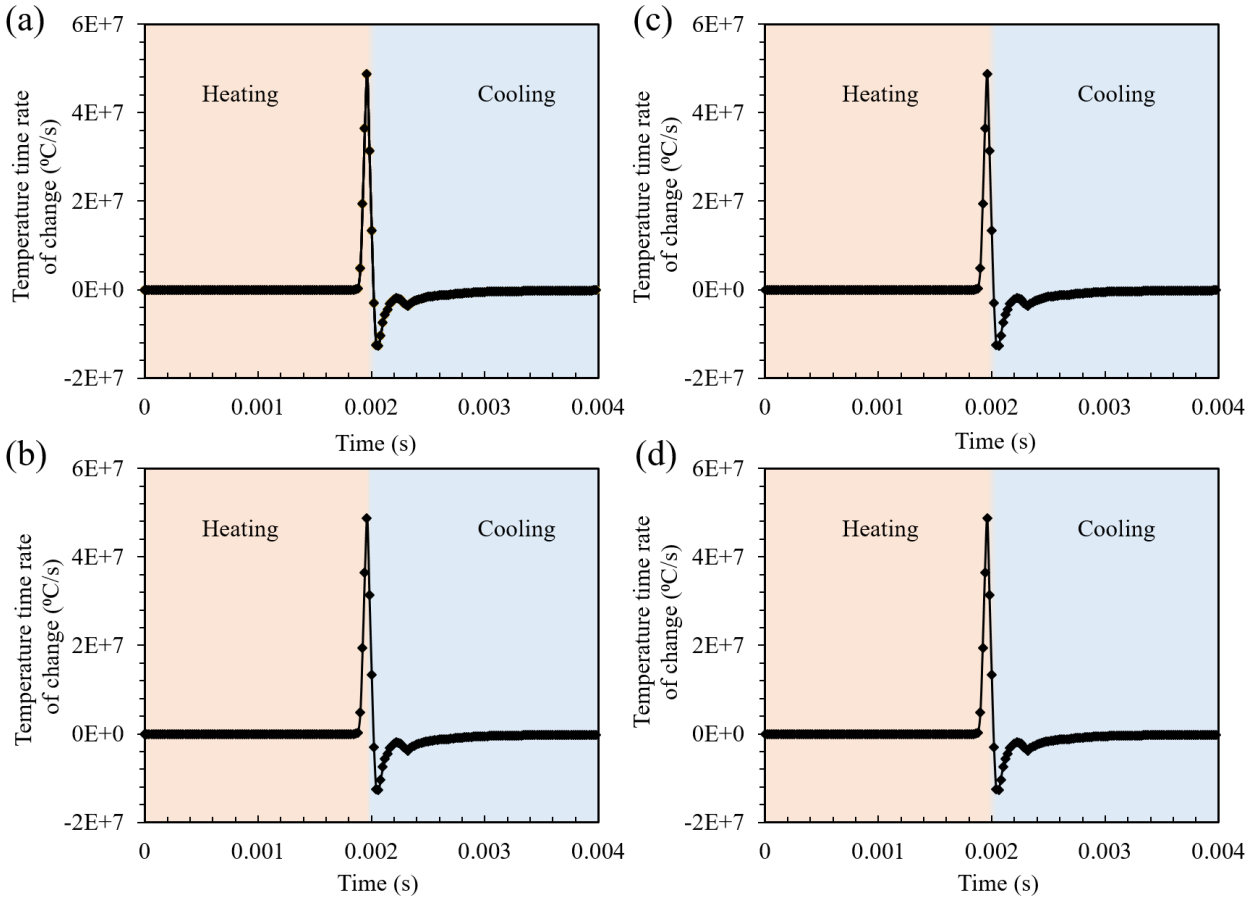

Figure 6.8 - Temperature time rate of change at the middle of track when gas and laser are moving at same direction and the speed of argon is (a) 4 m/s and (b) 8 m/s. Temperature time rate of change at the middle of track when gas and laser are moving in opposite directions and the speed of argon is (c) 4 m/s and (d) 8 m/s.

In order to understand the effect of gas-side convection on the cooling rates near the melt pool and solidified track interface – which have more influence on microstructure formation, the local TTRC at the bottom of the melt pool was investigated and the results are presented in Figure 6.9. Unlike the maximum cooling rates, here, the cooling rates are virtually unaffected by laser/gas relative motion or gas speed. The solidification 'bump' during cooling becomes more dampened and of lower magnitude. For the 4 m/s and 8 m/s gas flow speed conditions, the maximum,

absolute-value cooling rate is ~3% and 7% lower, respectively, during opposing laser/gas directions than for same-direction scenarios. This is a different trend that that observed for the top-side melt pool cooling rate – which, for the same gas flow speed, opposing laser/gas directions provided for higher cooling rates. Top-side preheating, which occurs during same laser/gas directions, ensures that more heat is available at the bottom of the melt pool for increased cooling rates. In call cases, the molten state cooling rate decreases with melt pool depth.

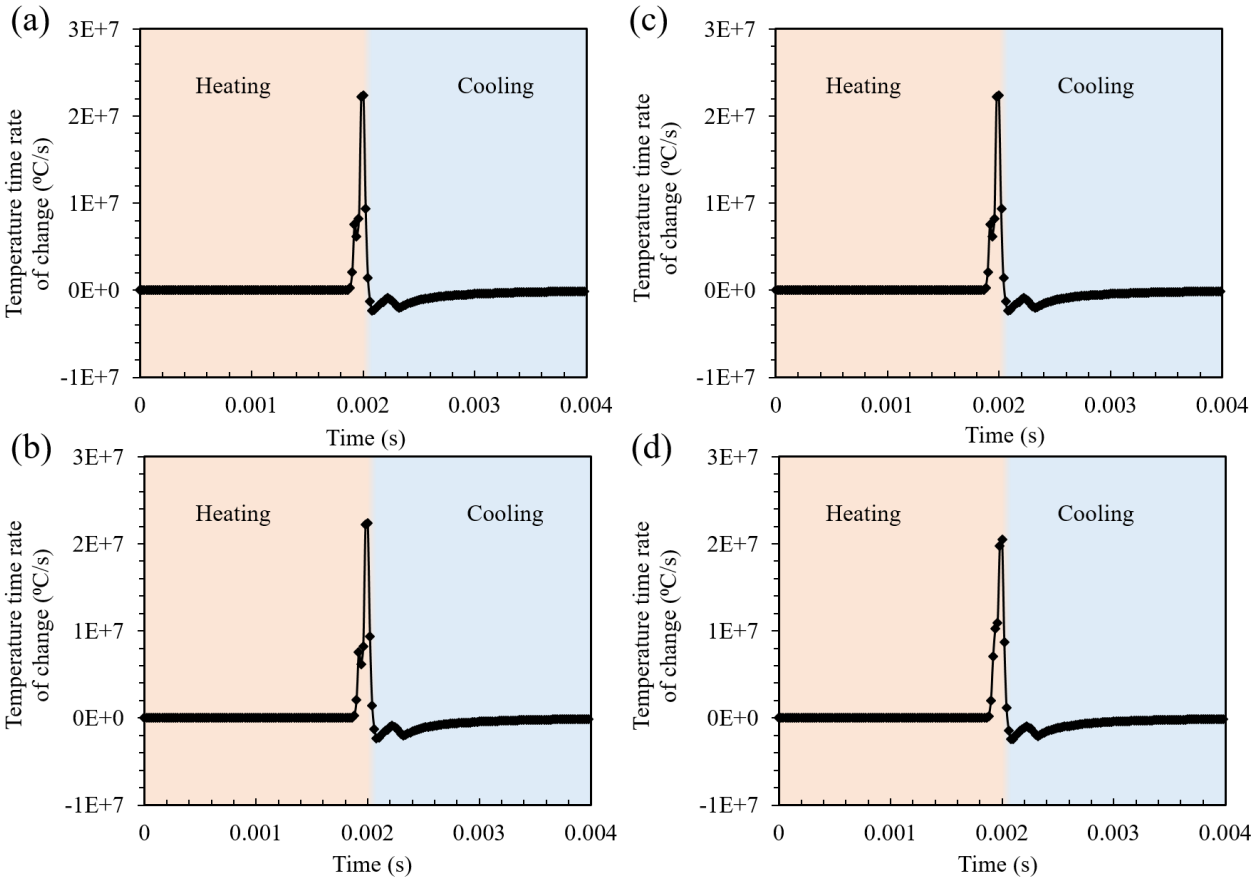

Figure 6.9 - Temperature time rate of change at the bottom of melt pool at middle of track when gas and laser are moving in same direction and speed of argon is (a) 4 m/s or (b) 8 m/s. Temperature time rate of change at the bottom of melt pool at the middle of track when gas and laser are moving in opposite directions and speed of argon is (c) 4 m/s or (d) 8 m/s.

To demonstrate how model assumptions can impact predicted convection and radiation heat transfer rates, the case in which both convection and radiation heat transfer are neglected, and the case in which a constant/uniform heat transfer coefficient for convection is employed, were

investigated. Figure 6.10 (a) shows the temperature and the temperature gradient results when convection and radiation heat transfer were neglected. Figure 6.10 (b) shows the temperature and temperature gradient results when a constant heat transfer coefficient, h = 15 W/m^{2}·ºC was used and radiation considered. It may be seen that the predicted, maximum temperature is ~40 ºC lower while the temperature gradient is ~2% higher when a constant heat transfer coefficient (with radiation) is considered relative to when neglected. As expected, the temperature and temperature gradients in both simplified cases differ in magnitude relative to those predicted when convective heat flux and adjoining gas flow are modeled.

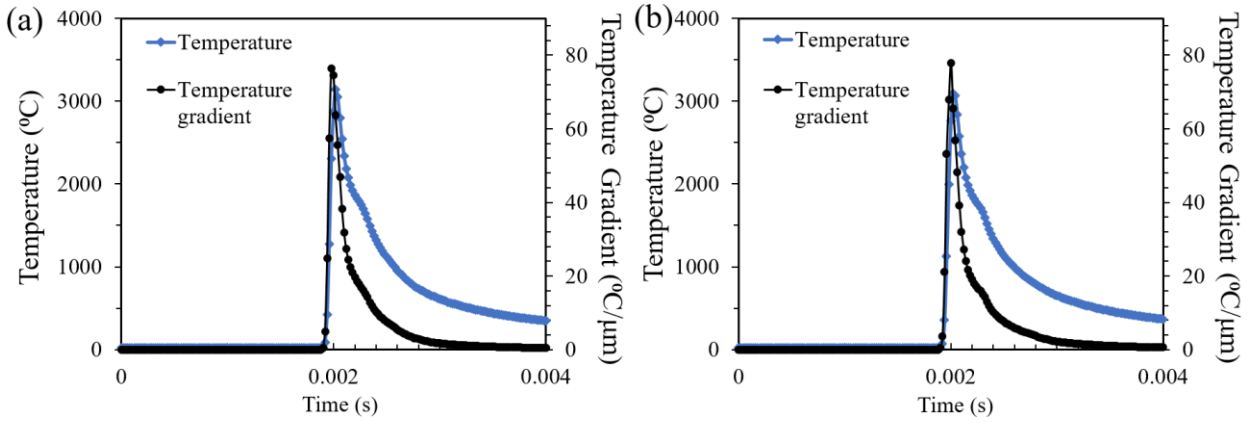

Figure 6.10 - Temperature and temperature gradient at the middle of track when (a) effects of convection and radiation are neglected, (b) constant heat transfer coefficient (h = 15 W/m^{2}· ºC) is used for convection and radiation considered.

The impact of assigning or neglecting a uniform convection heat transfer coefficient on predicted melt pool TTRCs (i.e. heating and cooling rates) was investigated. Figure 6.11 (a) provides the TTRCs of the top-side melt pool when thermal radiation and convection are neglected, while Figure 6.11 (b) provides the TTRCs when a uniform, constant heat transfer coefficient (with radiation) is assigned. It may be seen that when assuming uniform convection fluxes, the average melt pool cooling rates differ by 15% relative to when using CFD.

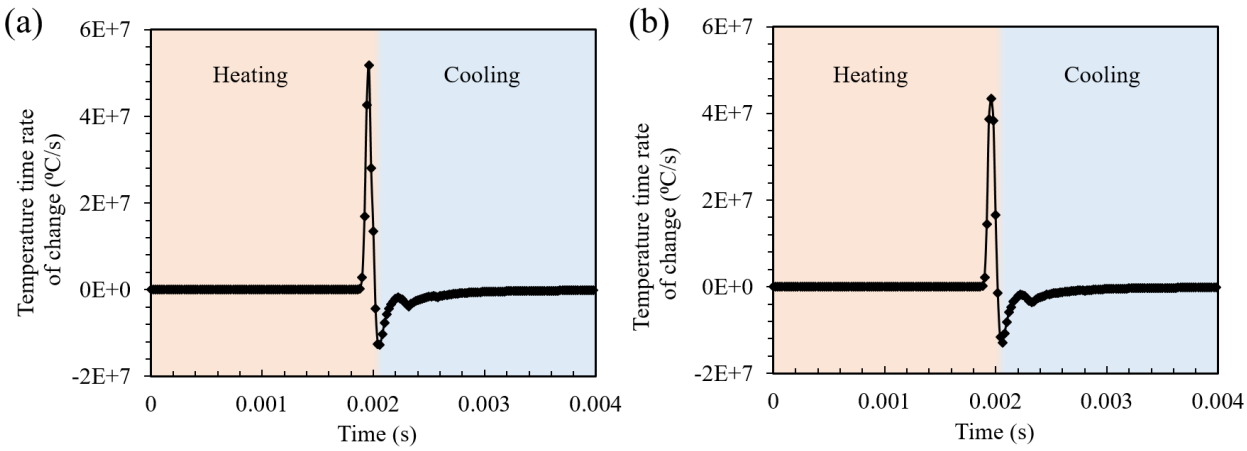

Figure 6.11 - Temperature time rate of change (TTRC) near top of melt pool at the middle of track when (a) effects of convection and radiation are neglected, (b) radiation is accounted for and a uniform, constant heat transfer coefficient (h = 15 W/m^2·ºC) is assigned.

CHAPTER 7

Efficient Numerical Simulation

7.1. Introduction

Since the thermal response of a part during its AM influences its microstructure, residual stress and defect formation, it is important to predict and model the inherent heat transfer as a function of part material type, geometry, location, orientation, operating environment, laser scan strategy, laser power, etc. By understanding these process-property relationships, one gains more control over the AM part/process design for building higher quality parts that meet constraints. These process-property relationships enable end-users to reduce the number of trial-and-error experiments required to learn optimal process/design parameters for a given material.

In-lieu of solving a complex set of governing, partial differential equations for the L-PBF problem, numerical simulation is employed, e.g. FEM and/or CFD. FEM may be used for numerically solving the discretized conservation equations via computational resources. The FEM discretizes the domain into thousands, or millions, of elements in which the conservation equations are applied iteratively using algebraic methods. Modeling and simulation techniques will play a critical role in advancing AM by providing a means to quantify how process variables affect resultant component properties [126]. Through effective process modeling, the underlying transport physics can be better understood and final, AM part production and qualification can be accelerated.

There are various space and time scales in which one can model the AM process. Simulation of the L-PBF process at the powder scale (micro-scale) allows one to integrate secondary/tertiary transport effects such as vapor generation, laser interaction, particle/molten-metal interaction, spattering, denudation and more – which all can contribute to the formation of defects. These models give temperature and time histories of the melt pool, with applications to real-time process diagnostics and microstructure development. Powder scale models can also be used to study issues of surface finish and part density.

To expedite the simulation process and gain the ability to perform simulation on large-scale parts, a new technique is proposed herein. This method combines a bundle of layers and simulates them together in order to decrease the number of layers required to perform a simulation. Results are compared to experimental findings from the literature.

7.2. Theory

For modeling the L-PBF process, typically each layer is simulated separately along with the per-island scan strategy. A typical part consists of hundreds of layers and thousands of meters of scan paths. In the proposed method, the heat flux applied at the top layer is assumed uniform. The time required to build a rectangular section is calculated as:

$$t = \frac{m \times l}{w \times v} \tag{7.1}$$

where l is the length of the rectangle, m is the thickness of the part, w is the hatching space, and v is scanning speed. The constant heat flux applied at the top of the layer is calculated as:

$$\boldsymbol{q}_{\mathrm{pb,i}} = \frac{P}{m \times l} \tag{7.2}$$

where P is laser power. Another assumption used to facilitate the simulation is attaching layers together to form a "bulk-layer" – in which the numbers of layers required to model the AM of a part is decreased significantly.

7.3. Validation

Tetrahedral meshes were used for the powder bed and were uniformly dispersed, being ~0.05 mm3 in size (mesh lengths of ~ 0.5 mm). To ensure mesh independent results, simulations were repeated with mesh with lengths of 0.25 mm. No major changes were observed in the simulation results. The numerical model was built using COMSOL® Multiphysics 5.2. Simulations were conducted using the 'Hopper' cluster at the High Performance Computing Center at Auburn University. Each job utilized 80 processors and a total of 128 GB memory. Employed simulation results were validated using data from L-PBF experiments conducted by Dunbar et al. in which a local temperature response was recorded using a thermocouple at the bottom of the substrate [127]. In these experiments, two Ti–6Al–4V parts with geometries of 6.35 x 6.35 x 1.5 mm^3 and 31.8 x 31.8 x 0.24 mm^3 were fabricated. The time interval for both cases was 10 seconds. The substrate size for fabrication of the parts was 89 x 26 x 0.81 mm^3 and 89 x 36.9 x 3.2 mm^3, respectively. The process parameters for the L-PBF process are presented in Table 7.1.

Two different simulations were conducted to compare the accuracy of each proposed modeling technique. First a constant heat flux was applied to each layer and the process was continued layer-by-layer until the whole part was simulated (S1). Second, a constant heat flux was applied at the surface of bulk-layers (S2). The temperatures predicted at the bottom of the substrate for S1-S2 are presented in Table 7.2. The simulation of a 31.8 x 31.8 x 0.24 mm^3 part for S1-S2 took approximately 3 hours and 30 minutes, respectively. The difference between temperature

prediction and experimental results for fabrication of the small part was 20 ºC and 35 ºC for S1 and S2, respectively. For the larger part, the temperature difference between the experimental result and the S1 and S2 simulation results was 25 ºC and 35 ºC, respectively.

Table 7.1 - Parameters used for simulating the L-PBF of a Ti–6Al–4V part.

System	EOS M280
Substrate material	Ti–6Al–4V
Powder description	Gas-atomized, air-dried
Powder layer thickness	30 µm
Laser spot diameter	100 µm
Laser power	280 W
Scan speed	1200 mm/s

Table 7.2 - Comparison between experimental results from Dunbar et al. [127] and different simulations conducted of Ti–6Al–4V 6.35 x 6.35 x 1.5 mm^3 part.

No	Experimental result [127]	Simulation #2	Simulation #3
1	105 ºC	125 ºC	140 ºC
2	305 ºC	330 ºC	340 ºC

It is observed in Figure 7.1 that the substrate and powder bed absorb thermal energy from the fabricated parts. Additionally, it is observed from Figure 7.2 that by fabricating a larger part and adding more power to the system, the effects of heat accumulation become more marked. Results suggest that modelling each layer separately via an ‘effective’/uniform laser heat flux (S1) is more accurate than a bulk layer approach (S2). However, when a constant heat flux is applied at the top of each layer the predicted temperature is higher than the measured temperature. This error could be explained by the fact that heat has less time to diffuse compared to when a local heat flux is modeled. Although individual layer modeling results in more accurate results, the traditional approach requires significantly longer computation times when compared to the proposed techniques.

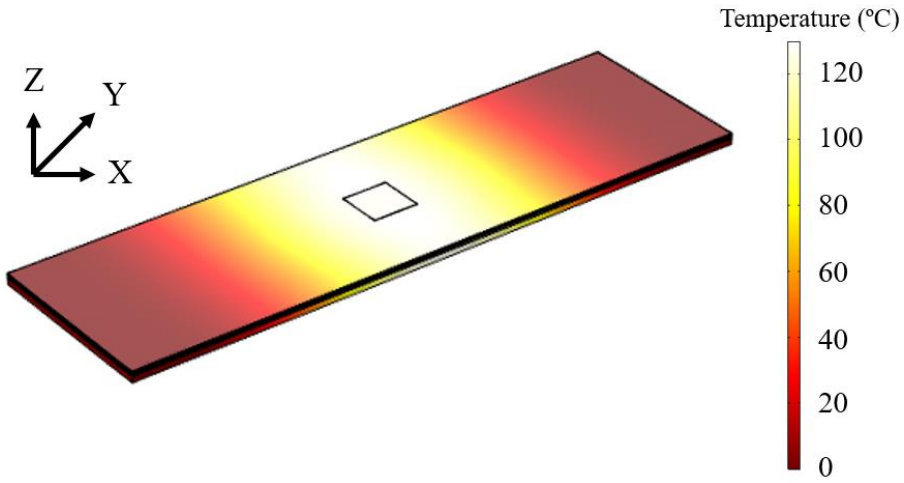

Figure 7.1 - Temperature distribution of Ti–6Al–4V 6.35 x 6.35 x 1.5 mm^3 part after fabrication has finished.

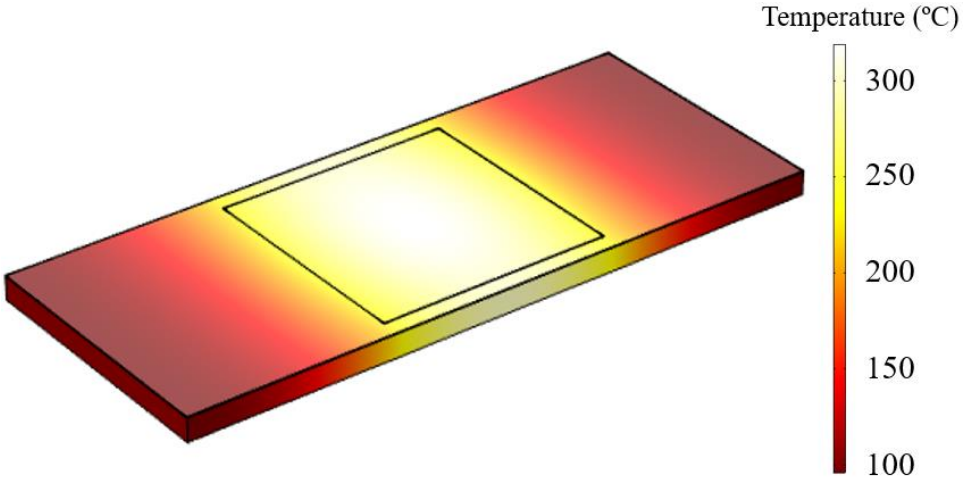

Figure 7.2 - Temperature distribution of Ti–6Al–4V 31.8 x 31.8 x 0.24 mm^3 part after fabrication has finished.

7.4. Results

The validated numerical approach was used to investigate the temperature distribution along two different-geometry SS 17-4 PH parts during L-PBF. One part was a cylinder with two cross-sections, i.e. a 'dog bone', as shown Figure 7.3 (a). The cylinder had a total length of 84 mm with the top and bottom portions having a diameter of 11 mm and the middle section having a length of 36 mm and a diameter of 7 mm. The other part was a square rod with a cross-section of 11 × 11 mm2 and thickness of 84 mm, as shown in Figure 7.3 (b). Process parameters used for

fabrication of these SS 17-4 PH parts are presented in Table 7.3. The time interval between fabrication of each layer was set at 10 seconds.

The temperature distribution along both parts immediately after fabrication is presented in Figure 7.4. It is observed that the temperature along newly-deposited layers is higher relatively to previously-deposited layers. Additionally, it is observed that the cylinder accumulated more heat relative to the square rod. Most of the thermal energy is diffused through fabricated parts. During fabrication of cylinder, the built area is smaller compared to square rod, thus, heat accumulation becomes more important.

Table 7.3 - Parameters used for simulating the L-PBF of a SS 17-4 PH part.

System	EOS M280
Substrate material	SS 17-4 PH
Powder description	Gas-atomized, air-dried
Powder layer thickness	40 µm
Laser spot diameter	100 µm
Laser power	220 W
Scan speed	755 mm/s
Hatching space	110 µm

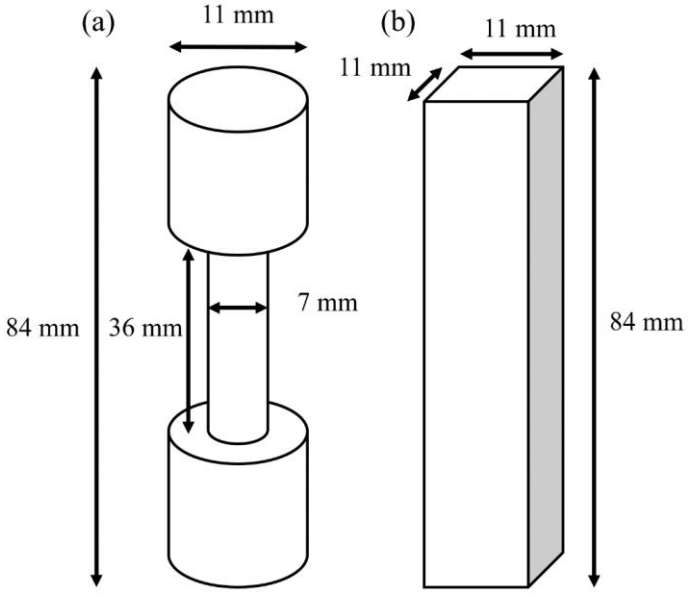

Figure 7.3 - Schematic of L-PBF simulated SS 17-4 PH parts.

As shown in Figure 7.5, the maximum temperature is almost 100 ºC higher on the cylinder relative to the square rod immediately after their L-PBF. This elevated temperature would generally correspond to lower temperature gradients and cooling rates along top portions of the cylinder. It is important to notice that the effects of heat accumulation are more significant at newly-deposited layers and tends to fade away with previously deposited layers. Additionally, it is observed in Figure 7.5 that when the built area during fabrication of the cylinder changes, the temperature distribution will significantly be affected. Smaller built area translates to higher heat accumulation.

The different thermal responses shown in Figures 7.4 – 7.5 indicate that, in general, different-sized/shaped specimens (e.g. cylinder and square rod) will have different microstructural and mechanical properties. In order to fabricate different-sized/shaped parts with similar mechanical properties, which would be important when transitioning from witness/test specimens to full-scale components, it is essential to fabricate parts with the same thermal response, i.e. local cooling rates, absolute temperatures, temperature gradients, etc. In order to achieve this, process parameters must be altered. A simple parameter to control/alter, and one employed herein, is the time interval between layers of fabrication. To demonstrate this, the layer-to-layer time interval the cylinder part was increased from 10 seconds to 15 seconds. It is observed from Figure 7.6 and Figure 7.7 that, in this case, the thermal response of the cylinder and square rod become much closer to each other.

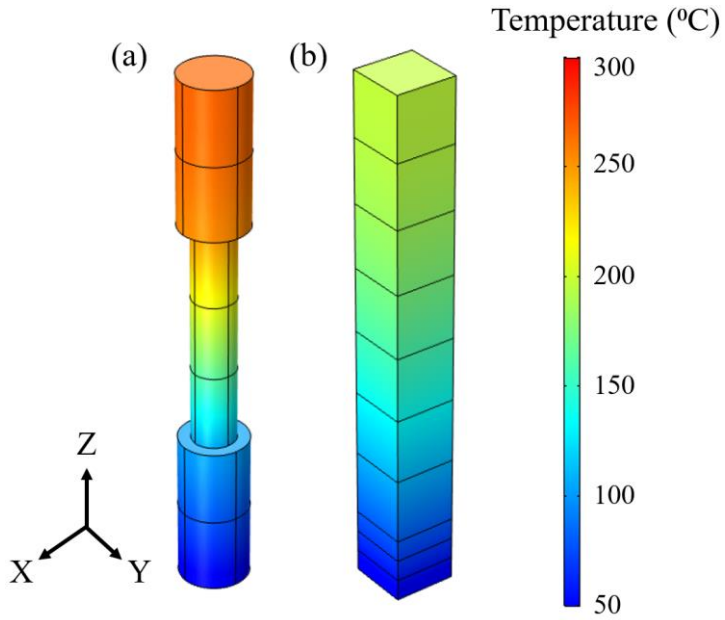

Figure 7.4 - Temperature distribution of fabricated (a) cylinder and (b) cube after fabrication of the parts.

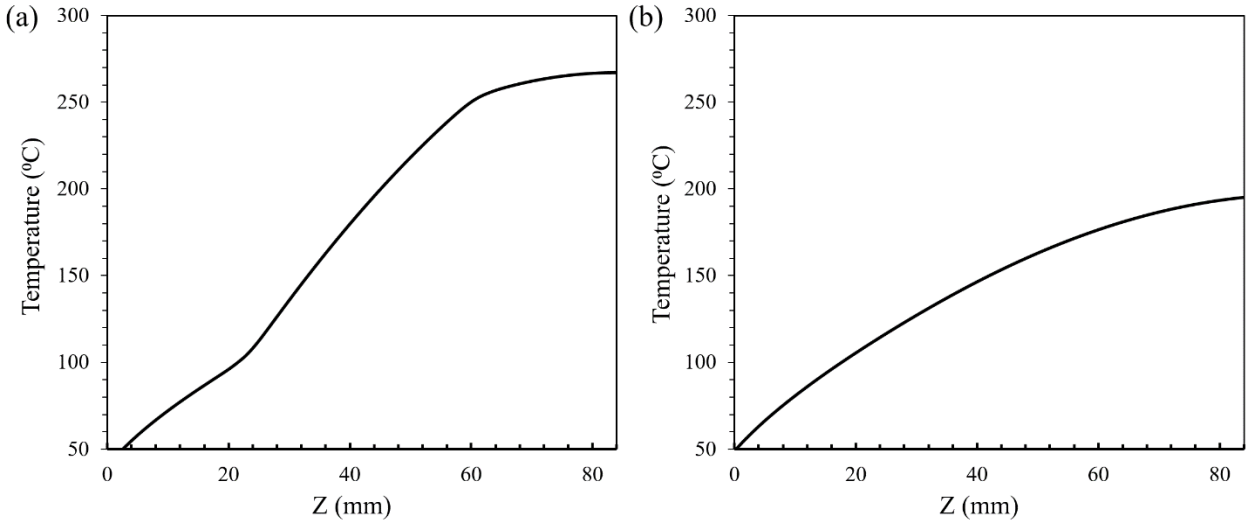

Figure 7.5 - Temperature distribution of (a) cylinder and (b) cube along the main axis after fabrication of last layer.

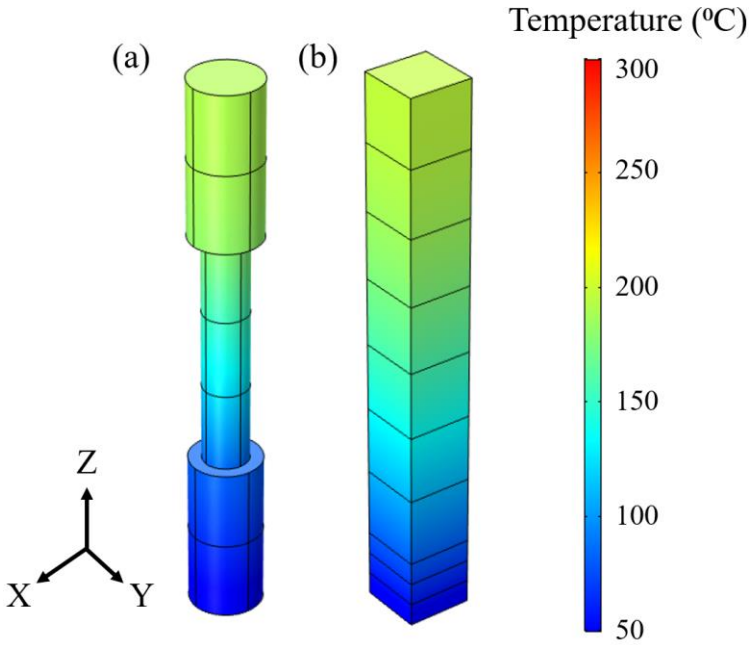

Figure 7.6 - Temperature distribution of fabricated (a) cylinder and (b) cube after fabrication of the parts.

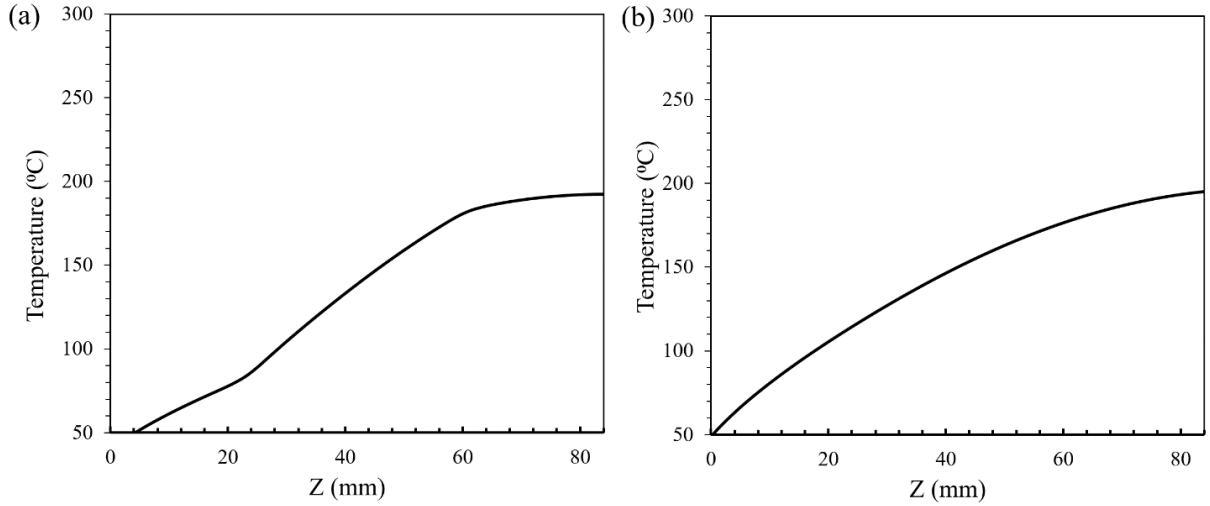

Figure 7.7 - Temperature distribution of (a) cylinder and (b) cube along the main axis after fabrication of last layer.

CHAPTER 8

Mechanical Implications

8.1. Introduction

The residual stress within heat treated and as-built (or, 'as-is') SS 17-4 PH specimens fabricated via L-PBF were measured using neutron diffraction at NIST's Center for Neutron Research (CNR). The presented data include measured lattice strains (i.e. d-spacings), stress-free lattice spacings (d0) and hoop/axial (or x-,y-,z-component) residual stress calculations. Uncertainties associated with residual stress measurements are estimated and also provided. All results are presented in the form of tables and plots in multiple Excel worksheets. Three specimens were analyzed and their corresponding measurements are grouped by tab color, i.e.: vertical as-is (i.e. as-built) rod (color code = red), vertical/heat-treated as-is rod (color code = blue), and the horizontal as-is parallelepiped (color code = yellow). Comment boxes are provided in the Excel sheets with instructions on how to replicate calculations using X-ray diffraction data analysis software. Data are supported with schematics that indicate the diffraction locations and manufacturing scan patterns.

8.2. Experimental Design, Materials and Methods

A PHENIX PM-100 system equipped with a 50 W Nd:YAG laser was utilized for the L-PBF of specimens from gas-atomized, SS 17–4 PH powder (Phenix Systems) feedstock. The powder feedstock possessed a size distribution of: 10 μm < D50 < 13.5 μm and D80 < 22 μm

[128]. All specimens were built together on the same, non-heated substrate within an argon-purged environment. Two vertical rods and a horizontal parallelepiped were manufactured. The cylindrical specimens were approximately 8 mm in diameter and 80 mm in height. Each layer of the parallelepiped possessed dimensions of 8 × 80 mm2 and its total height was 9 mm. Process parameters (i.e. laser power, scanning speed, layer thickness, and hatching pitch) were optimized to obtain an acceptable level of final part density using a design of experiments methodology [128]. The final process parameter used, which are summarized in Table 8.1, included: laser power of 48 W, traverse speed of 300 mm/s, layer thickness of 30 μm, and hatching pitch of 50 μm.

Table 8.1 - Parameters used for fabricating specimens.

Powder and substrate material	SS 17-4 PH
Powder description	Gas-atomized, air-dried
Powder size distribution	10 μm < D50 < 13.5 μm
Powder layer thickness	30 μm
Hatch spacing	50 μm
Laser spot diameter	70 μm
Laser power	48 W
Laser wavelength	1075 nm
Scan speed	300 mm/s
Shielding gas type	Argon
Shielding gas temperature	20 ºC
Shielding gas flow rate	167 cm^3/s
Substrate temperature	20 ºC

Default scan strategies were used for fabricating each specimen. For the vertical rods, the laser started at the top left region of the first layer as shown in Figure 8.1 (a). The laser then moved back and forth in a hatching pattern until the layer was complete. For the second layer, the same hatch pattern was repeated; only it was rotated 90° clockwise, as shown in Figure 8.1 (b). The scan patterns for the third and fourth layers were similar, however, they were rotated 180° and 270° clockwise relatives to the first scanning directions, as shown Figure 8.1 (c) – (d). This scan strategy was repeated after completion of the fourth layer until the end of the build. For the parallelepiped,

the scan strategy consisted of building several, equal-sized hexagonal regions (~5 mm in length) in a random order. The hexagonal scan strategy varied with each layer as shown in Figure 8.2. The layer-wise scanning strategy outlined in Figure 8.2 was repeated after completion of every 6th layer.

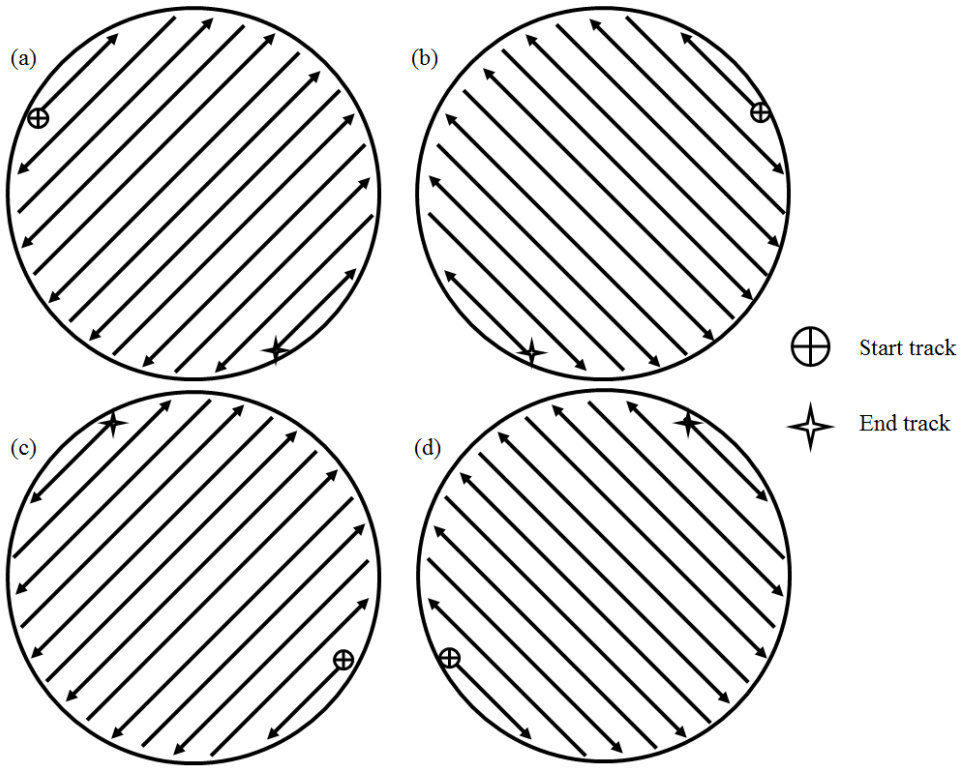

Figure 8.1 - Scan strategy for vertical sample for the first through fourth layers (a) to (d), respectively. Successive layers are a repeat of these four in the same order.

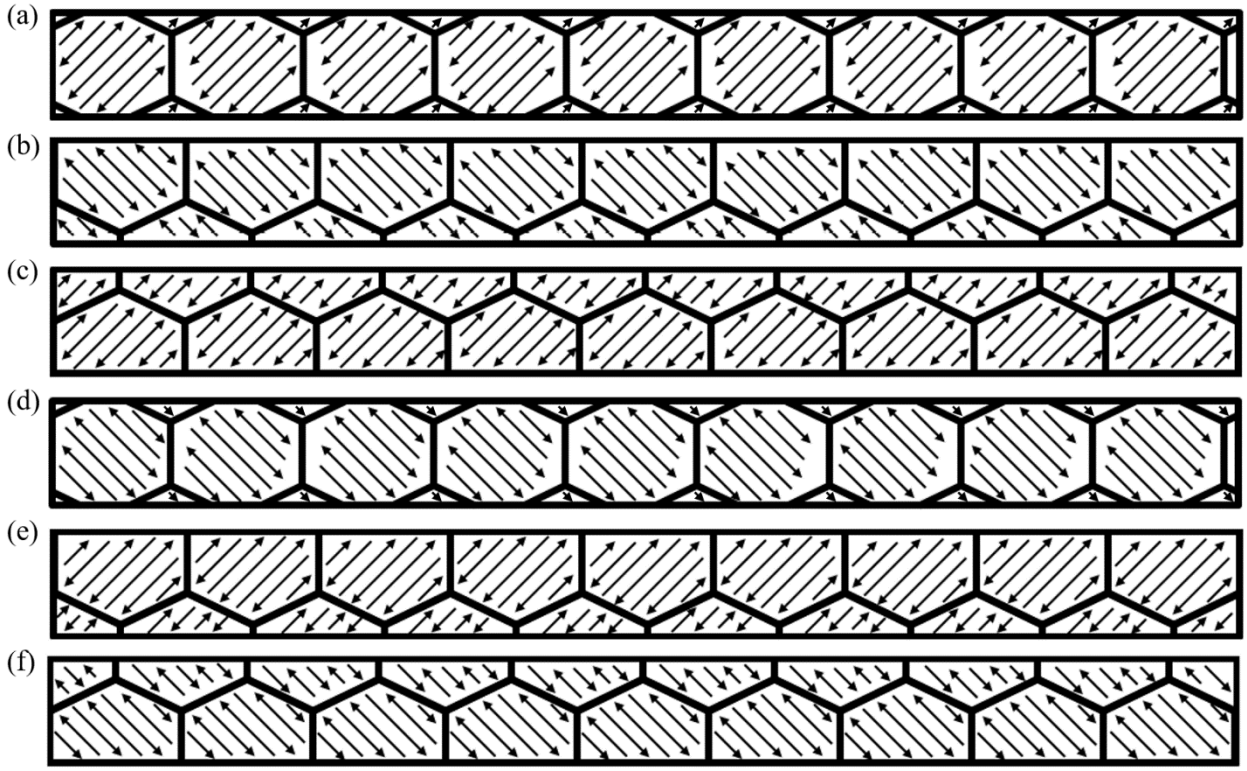

Figure 8.2 - Scan strategy for horizontal sample layers one through six, (a) to (f), respectively. Successive layer is a repeat of these six in the same order.

Electrical discharge machining (EDM) was employed to remove specimens from the substrate. Samples were not thermally stress relieved prior to their removal. In order to investigate the effect of heat treatment, one of the as-built rods underwent solution annealing (Condition A) followed by peak-aging (Condition H900) [129]. The final microstructures consisted of a mixture of ferrite and austenite. All specimen surfaces were cleaned of any loose powder.

Lattice strains (i.e. d-spacings) were measured along orthogonal directions at pre-selected 1 x 1 x 1 mm3 regions (i.e. gage volumes) of the specimens using the BT8 neutron diffractometer at NIST's CNR. Employed neutrons originated from a continuous, cold source. The BT8 residual stress diffractometer possessed three monochromators and a rotating drum (for inspecting multiple specimen orientations) to allow for wavelength variation between 0.8 to 3.2 Å and measurement of d-spacings between 0.56 to 2.26 Å. The neutron beam wavelength was set to 1.637 Å. An Ordela 1150 position sensitive neutron detector with an angular opening of approximately 8° was

employed. The adopted measurement method used several pole figures for each phase, which in this case was austenite and ferrite, to obtain an orientation average of the hkl-dependent peak intensity [130]. The techniques used herein are explained in detail elsewhere [131,132].

Residual stresses were calculated using Bragg's law with many of the coefficients provided in Columns J-W in the Excel worksheets. Due to the weak attenuation of neutrons, their penetration depth is higher than X-rays [131]. Diffraction from the {311} planes at $2\theta = 95.89°$ and {211} planes at $2\theta = 88.77°$ were used for analyzing the austenite and ferrite phases, respectively. It took approximately hour to collect neutron diffraction data per diffraction peak. Due to time constraints, it was not possible to perform the elastic constants measurements. Instead, the isotropic diffraction elastic constants were calculated using the Kröner model as described in [133]. Note that each gage volume consists of approximately 33 layers, thus residual stress measurements are spatially averaged.

The stress-free lattice spacing, d0, was calculated for each sample by utilizing near-surface measurements where the stress component normal to the surface can be presumed to be zero. In this case, radial stresses for cylindrical samples were presumed to be zero near the surface. This was done for each phase, and the weighted average was calculated. For the parallelepiped, d0 was estimated from measurements with locations close to surfaces in which either $\sigma xx = 0$ or $\sigma zz = 0$ was applicable, Figure 8.3 (b). Four different estimates for d0 were obtained, and the average was taken, thus obtaining a single d0 for each phase This is a common method for circumventing the d0 problem [134]. The d0 calculations for the parallelepiped have a dedicated tab in the Excel file: "S3 d0". The presence of a third phase due to precipitation hardening was not accounted for and therefore presents an unresolved uncertainty.

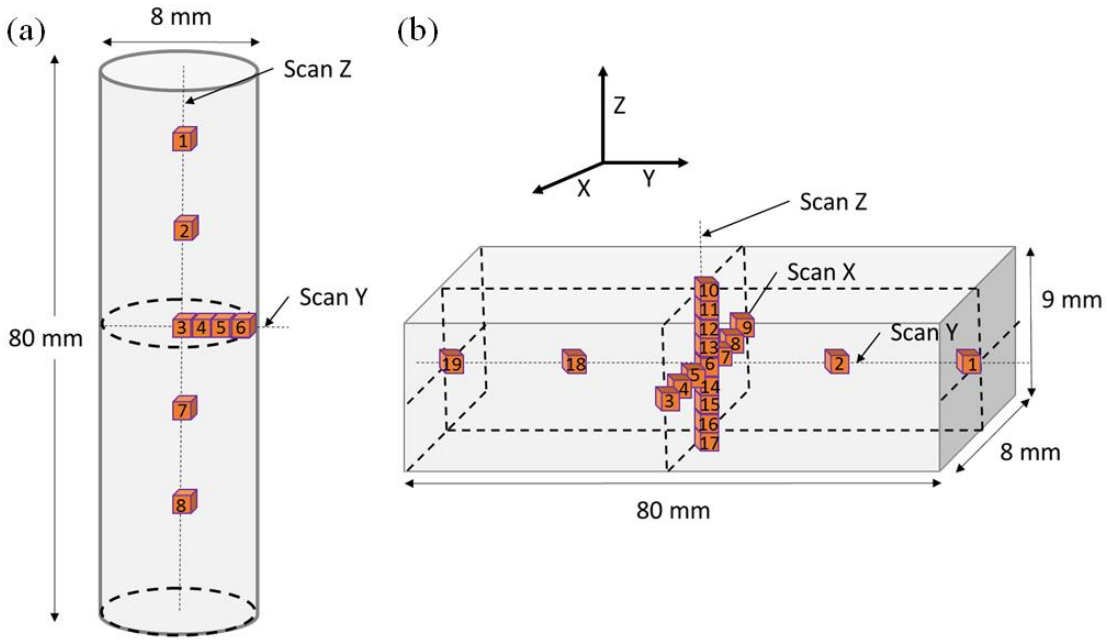

Figure 8.3 - Measurement locations for (a) as-built and heat-treated cylindrical specimens and (b) as-built horizontal parallelepiped specimen.

Measurement locations are presented in Figure 8.3. Gage volumes were distributed along the y (radial) and z (axial) axes for cylindrical samples to find residual stress trends in these directions. As shown in Figure 8.3(a), four measurement locations, #3, #4, #5 and #6 were distributed along the radial direction and five measurement locations were distributed along the axial direction, #1, #2, #3, #7 and #8. For the parallelepiped, 7, 5 and 9 measurement locations were distributed along the x, y and z directions, respectively. The gage volumes were evenly spaced in each direction. In Table 8.2 and Figure 8.4, the hoop and axial stress along with their uncertainty for the as-built rod are presented. In Table 8.3 and Figure 8.5, the residual stress for same points are presented for the heat-treated rod. Finally, the Cartesian component residual stresses for the as-is, horizontal parallelepiped at the aforementioned measurement locations are presented in Table 8.4 and Figure 8.6.

By comparing the residual stress data for the as-built and heat treated vertical samples, it is found that heat treatment relieves stress and that the residual stress magnitude will decrease.

Additionally, residual stress in the as-built horizontal samples are generally higher compared to vertical samples since temperature gradients are typically lower during processing. Lower temperature gradients will result in lower residual stress.

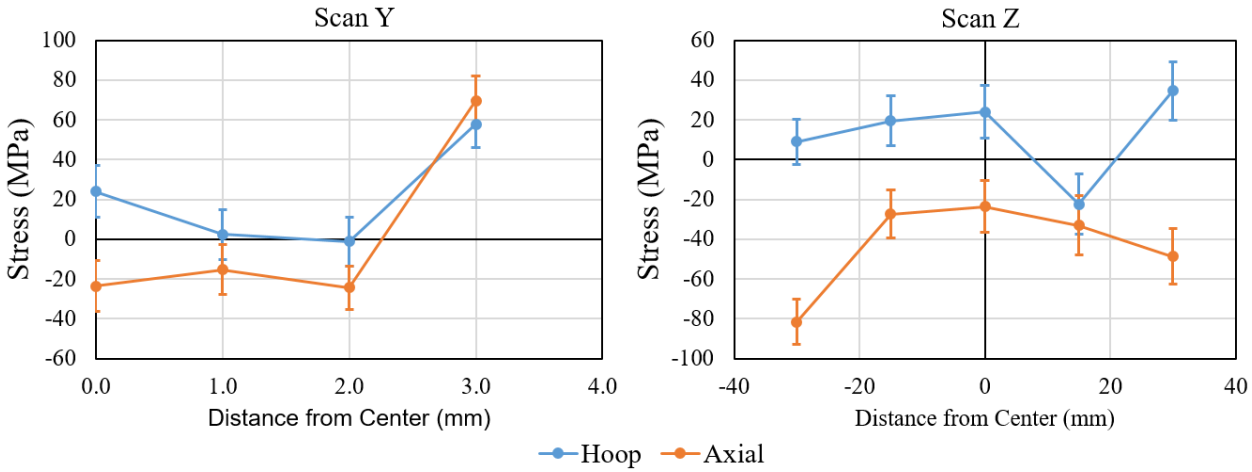

Figure 8.4 - Residual stress distribution for as-built SS 17-4 PH Vertical sample along Y and Z directions.

Table 8.2 - Residual stress and its uncertainty for vertical as-is sample

Point #	Average hoop (MPa)	Uncertainty (MPa)	Average axial (MPa)	Uncertainty (MPa)
1	37.8	15.2	-52.4	14.4
2	-23.3	16.0	-35.3	15.9
3	35.2	13.8	-14.1	13.7
4	-1.8	13.0	-16.7	13.3
5	-3.1	12.9	-26.8	11.3
6	52.6	12.5	59.8	13.4
7	16.0	13.1	-23.4	12.8
8	7.3	11.7	-84.7	11.8

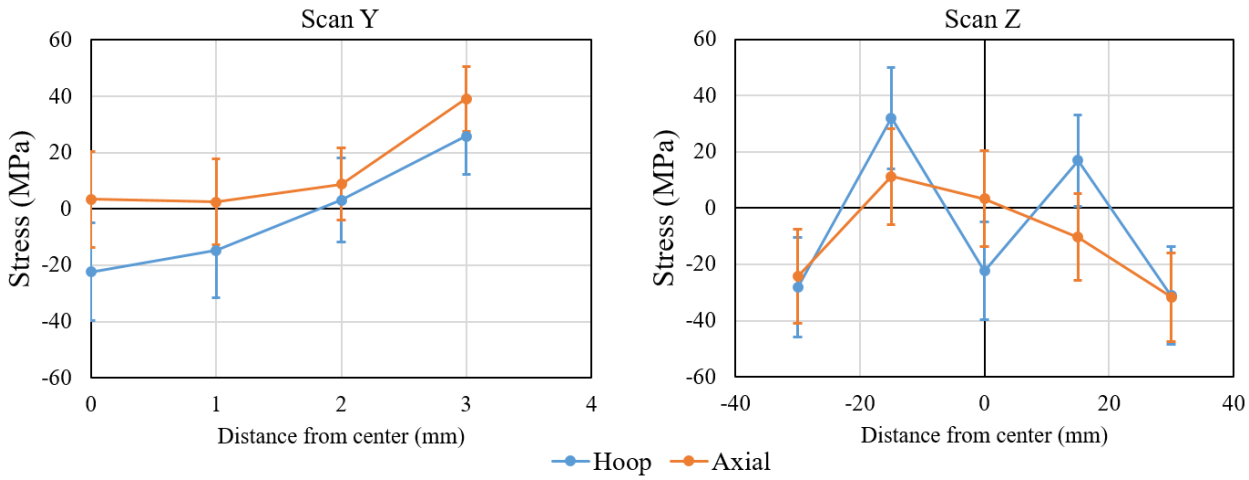

Figure 8.5 - Residual stress distribution for heat treated SS 17-4 PH Vertical sample along Y and Z directions.

Table 8.3 - Residual stress and its uncertainty for vertical heat-treated sample

Point #	Average hoop (MPa)	Uncertainty (MPa)	Average axial (MPa)	Uncertainty (MPa)
1	-38.4	18.8	-33.6	17.0
2	25.9	17.4	-5.8	16.4
3	-27.4	18.8	8.4	18.4
4	-9.7	18.1	4.4	16.5
5	-10.5	16.2	-2.4	13.6
6	24.2	14.9	39.7	12.5
7	38.5	19.3	8.6	18.5
8	-148.8	18.1	-22.0	17.9

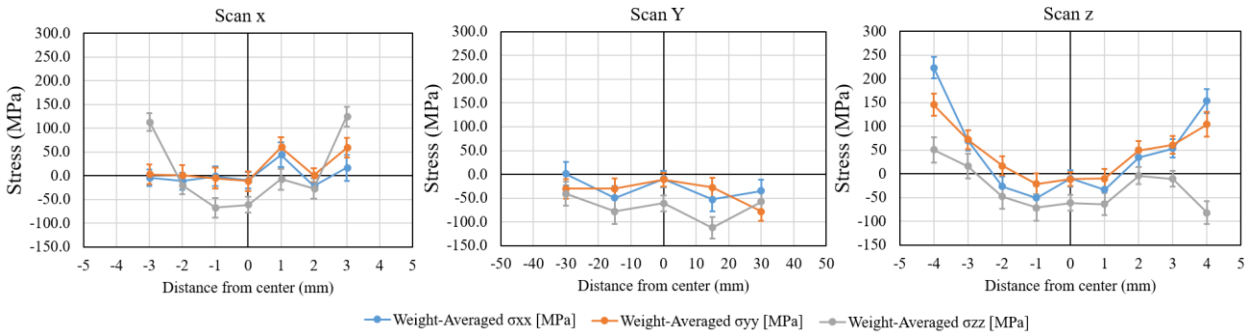

Figure 8.6 - Residual stress distribution for as-built SS 17-4 PH horizontal sample along X, Y, and Z directions.

Table 8.4 - Residual stress and its uncertainty for horizontal as-is sample

Point #	σ_{xx} (MPa)	Uncertainty (MPa)	σ_{yy} (MPa)	Uncertainty (MPa)	σ_{zz} (MPa)	Uncertainty (MPa)
1	-34.8	23.3	-78.3	20.0	-57.7	20.9
2	-53.1	24.8	-27.5	20.4	-112.5	22.7
3	16.6	27.6	58.9	21.9	124.4	20.8
4	-21.6	26.9	1.0	21.5	-27.2	21.2
5	44.1	26.0	60.2	20.8	-7.5	21.8
6	-9.8	17.1	-11.1	14.6	-61.2	16.3
7	-1.1	20.6	-5.4	20.3	-67.2	20.8
8	-11.4	17.6	0.8	18.6	-20.4	19.2
9	-4.6	17.5	2.7	20.1	112.7	18.2
10	153.3	25.2	104.3	25.5	-82.0	24.1
11	53.3	19.5	60.9	18.6	-10.3	16.5
12	34.7	20.3	49.7	18.8	-3.9	18.2
13	-33.2	25.4	-9.7	20.5	-64.0	23.1
14	-50.5	25.3	-21.3	21.8	-71.5	28.0
15	-26.8	21.8	16.9	20.5	-48.0	25.8
16	70.3	21.1	71.9	20.0	16.3	25.7
17	223.6	22.2	145.5	23.1	50.4	26.6
18	-49.8	24.6	-30.3	21.1	-78.5	25.7
19	1.3	24.4	-30.5	20.7	-41.1	25.2

8.3. Microstructure

To assess the impact of local convection heat transfer on L-PBF Ti-6Al-4V part microstructure, select manufacture-and-inspect experiments were performed. Two identical Ti-6Al-4V samples (10 x 10 x 5 mm^3) were fabricated using an EOS M290 L-PBF machine with the same process parameters, as presented in Table 4.4, and scan strategy, as presented in Figure 8.7. The only difference between the manufacturing of these two samples was the orientation of tracks (and thus, laser scan direction) relative to gas flow direction. Tracks for the first sample (Sample A) were perpendicular to the flow direction (Condition A), while tracks in second sample (Sample B) were parallel to the flow direction (Condition B). In both cases, the laser scan direction

alternated 180º between tracks. Once removed from the substrate, both samples were sectioned and prepared for microscopy using standard metallographic procedures.

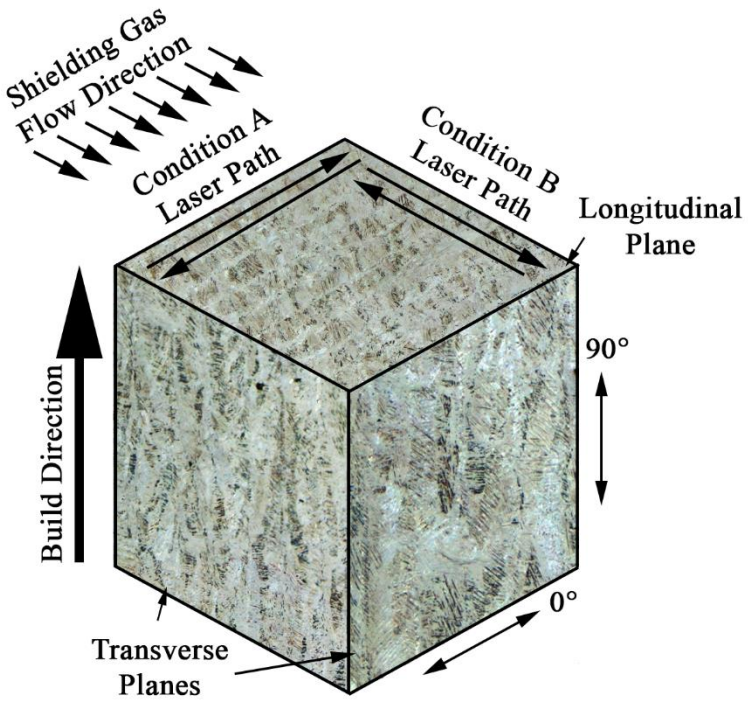

Figure 8.7 - Depiction of conditions A and B in terms of laser path direction and the longitudinal and transverse planes during L-PBF experiments.

The microstructure inherent to the L-PBF Ti-6Al-4V parts was revealed using Kroll's reagent in the longitudinal and transverse directions. As shown in Figure 8.8, very distinct columnar prior β grains were observed. It can be seen that grains develop in an epitaxial manner from each successive layer resulting in the columnar type prior β grains forming parallel to the build direction. In the longitudinal direction, grains appear to be influenced by the laser tracks from the build process similar to another study [135]. Within these prior β grains are acicular martensite, α'- needles which form as a result of the high cooling rate associated with the L-PBF process. Traditional, wrought Ti-6Al-4V is an α + β alloy which results in it having relatively good ductility as a result of the stabilized β phase at equilibrium. For the L-PBF process, cooling rates are sufficiently high that the α phase does not have time to diffuse from the β phase upon cooling.

Instead, the diffusionless β → α' phase occurs rapidly with the primary α' needles stretching across the entire prior β grain after which secondary, tertiary, etc. α' occur between preceding α' needles [135]. This process results in a randomly oriented α' phase as shown via the inverse pole figure map (for an L-PBF Ti-6Al-4V specimen) in Figure 8.8. The α' grain size was found to have an approximate width of 1.5 μm with an aspect ratio of approximately 0.55. No significant variation in α' grains was observed between samples A and B, and this is not surprising given the nature of the diffusionless transformation in which the shear type formation of the thin α' phase [135].

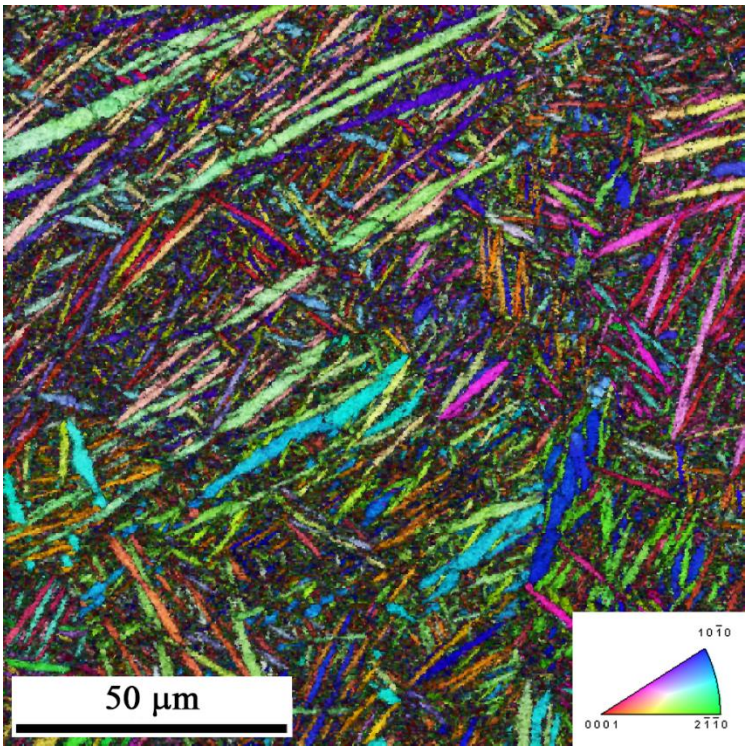

Figure 8.8 - Inverse pole figure map depicting the size and shape of the α' microstructure in the L-PBF Ti-6Al-4V.

There were observable differences in prior β grains between the two L-PBF samples. This is especially important when considering implications on mechanical properties of Ti-6Al-4V such as intergranular failure and ductility [136–138]. This difference is apparent when viewing the optical microscopy images of individual layers from Samples A and B. Comparing the prior β grains in the longitudinal (along the laser direction) and transverse (perpendicular to the laser

direction) direction in Figure 8.9, there is a clear difference in the size and shape of grains between the two paths. Sample A shows a less defined laser track path across its longitudinal layer, while Sample B has well defined tracks.

Prior β grain size analysis was conducted for each sample in accordance with ASTM E112. Measurements were taken in the longitudinal and transverse (perpendicular to laser direction) directions in accordance with ASTM E112. Due to the columnar type grain growth, the grain size in the transverse direction was measured at 0° from the horizontal axis (minor grain axis) and 90° from the horizontal axis (major grain axis) as detailed in Figure 8.7. Grain size analysis was not reliable in the transverse 90° direction (major axis) due to the small height of the samples and the large grain size in that direction; however, an approximate size was discerned as being between 300 – 500 μm. Measurements of the track sizes in the longitudinal direction are given in Table 8.5 and show that Sample B has slightly larger tracks widths of 101.40 μm as compared to Sample A at 99.42 μm (~2% difference). This variation in track width can be explained by the melt pool/HAZ profile depending slightly on laser/gas-flow configuration. As shown in Figure 6.2, scan/gas direction can alter the width and length of the melt pool (and HAZ) trailing edge leading to the differences in track appearance for Samples A and B.

The prior β grain size in the longitudinal direction is mostly related to the size of the focused laser beam and can be difficult to accurately measure. However, the diameter of the prior β grains in the longitudinal direction are closely related to the width of the prior β grains in the transverse 0° direction (minor axis). Comparing the transverse 0° direction for samples A and B, horizontal axis for the transverse direction in Figure 8.9, there is an approximate 10% increase in the prior β grain size of sample B compared to sample A. These changes in prior β grain size can be attributed to the decreased cooling rate when the shielding gas is along the same direction of

the laser. Comparing the grain size results to the numerical model, the effect of shielding gas flow direction, in relation to the laser path, can be visually observed. By preheating the powder, which occurs in the case when gas flow is in the direction of the laser, the cooling rate is slightly decreased. The lower cooling rate allows for a slight coarsening of the prior β grain structure before the diffusionless β → α' transformation occurs.

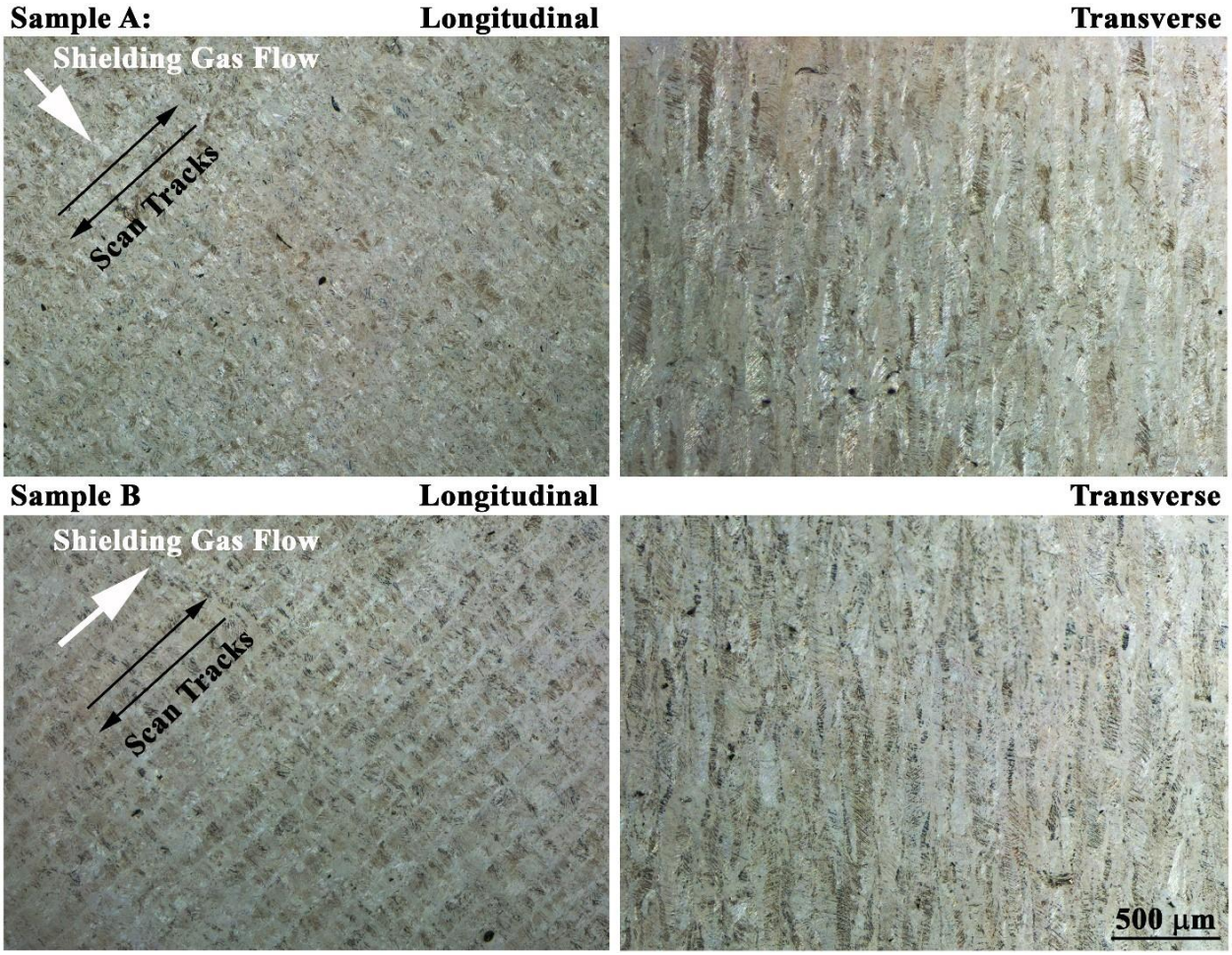

Figure 8.9 - Optical images detailing the size and changes in the track appearance for the longitudinal direction associated Samples A and B.

Table 8.5 - Prior β grain size measurements.

Direction	Sample A	Sample B	Standard Deviation
Transverse 0°	84.62 μm	94.15 μm	4.3 μm
Transverse 90°	300-500 μm	300-500 μm	N/A
Longitudinal	99.41 μm	101.40 μm	1.6 μm

With regard to Condition B (alternating laser directions collinear with gas flow) - due to solidification heat transfer being dominant during the as-processed track, any effects of preheating from the laser moving in the same direction as the gas flow should already be 'set' prior to the start of the opposite-to-flow scan. As the opposite-to-flow scan is in progress, the previously-fused track adjacent to the current track will mainly experience sensible heat transfer which should only contribute toward microstructure growth. Hence, any preheat effects inherent to similar-to-flow laser scans should not be removed by subsequently and adjacently scanning in the opposite direction. If the tracks were all built in the same direction as the gas, the effects of preheating should be amplified.

Experimental results suggest that the effects of gas flow direction can influence the mechanical properties of AM parts. It has been shown that L-PBF Ti-6Al-4V parts have a lower ductility relative to their wrought counterparts due to their martensitic microstructure with sizes governed by prior β grains [136,137]. In general, larger prior β grains can be susceptible to intergranular failure which can also affect part ductility [136–138], thus increasing the prior β grain size may lead to improved ductility since a lower volume fraction of grain boundaries would be present. These observations suggest that control of the prior β grain size, as accomplished through gas/laser direction planning, may lead to improved ductility of L-PBF Ti-6Al-4V parts.

CHAPTER 9

Conclusions

A continuum-based, numerical model was used to study the effects of scan strategy, shielding gas convection (and radiation) on total heat transfer, subsequent microstructure, and the heat transfer during single-laser and multi laser powder bed fusion of Ti-6Al-4V and SS 17-4 PH. The convective heat flux was calculated directly by modeling typical gas flow characteristics within the L-PBF chamber via CFD. Effects of various synchronous, orthogonal scan patterns, island division schemes (IDSs) and levels of island planning (LIP) on the temperature response during the fusion of the first and second layers of a multi-track Ti-6Al-V parallelepiped were investigated. The gas velocity and temperature boundary layers atop the powder bed and track were calculated. The combined melt pool/HAZ temperature distribution was found while either: (i) considering the gas-flow-coupled convective heat flux, (ii) neglecting convection/radiation transfer altogether, or (iii) considering a uniform heat transfer coefficient of h = 15 W/m^2·^{o}C (with thermal radiation). Dimensional numbers representative of the local L-PBF thermofluidics were presented and Ti-6Al-4V specimens were fabricated using various L-PBF scanning strategies for inspection of their microstructure (including type, size, orientation and more). The major findings from the study are summarized below:

1) The use of more lasers during PBF significantly decreases production times as the build rate per layer increases. As the number of lasers increases, the average powder bed temperature and total HAZ area increases, thus reducing local temperature gradients and cooling rates.

2) Peak melt pool temperatures are near-independent of the scan strategy and number of lasers used per layer. Melt pools were predicted to have peak temperatures around 2500 ºC; neighboring points within the layer immediately below were found to have temperatures just above liquidus for effective remelting and fusion.
3) Peak cooling rates are on the order of 10^6 ºC/s, and semi-continuous cooling rates are on-the-order of 10^3 ºC/s during the L-PBF process investigated. These rates are conducive for martensitic microstructure formation in Ti-6Al-4V. Microstructural anisotropy will be higher in parts fabricated via island-based ML-PBF.
4) Maximum temperature gradient magnitudes are on-the-order of 50 ºC/µm. Local temperature gradients are direction-dependent and consist of low track/scan-wise (X) and sweep-wise (Y) components and significantly higher layer/height-wise (Z) components.
5) The IDS, and thus track length with respect to a part's shortest edge, both have a significant influence on a layer's temperature response, cooling rate and temperature gradients. Employing IDSs that provide for a unit-row of islands sequenced along the longest edge of a part allows for shorter track lengths and reduced residual stress magnitudes. Using multi-laser scan strategies that provide for time-variant relative position between lasers will result in a more complex, anisotropic residual stress distribution along the layer of a part.
6) The LIP dictates the number of lasers employed and whether or not sub-islands exist for a given layer; LIP-0 corresponds to single-island/single-laser approaches, LIP-1 corresponds to multi-island/single-laser approaches, LIP-2 corresponds to single-pass ML-PBF (i.e. one island per laser) and LIP-3 corresponds to multi-island ML-PBF. The results indicate that the LIP will affect temperature gradients and cooling rates.

7) When the laser and gas move in the same direction, heated gas is pumped 'downstream', resulting in a temperature boundary layer that protrudes into the non-heated, yet-to-be-processed portion of the powder bed. This gaseous preheat increases convection heat transfer to the powder bed and leads to decreased temperature gradients ahead of the melt pool. Since lower temperature gradients within a solid have been shown to result in reduced residual stress [25,139,140], this localized preheating effect may result in lower residual stress formation along a given track.
8) The Richardson number is near zero indicating that although buoyancy effects are relatively more important near the HAZ, convection heat transfer is predominately dominated by advection inside the chamber. For the simulated chamber conditions, the velocity boundary layer was found to be completely laminar based on the Reynolds number. As the supply gas speed increases the importance of convection during L-PBF increases.
9) Convective heat transfer becomes relatively more important when the laser and gas move in the same direction, compared to the case when they moved in opposite and perpendicular directions.
10) Changing the speed or direction of shielding gas has only a minor effect on the maximum temperature of the melt pool, on the other hand it can greatly affect local temperature gradients in the HAZ. Increasing the gas speed or aligning the flow and laser in same direction can lower the temperature gradient.
11) Neglecting convection and radiation during L-PBF can affect the accuracy of predicted temperature, temperature gradient, and cooling rate. In all cases, the predicted results were higher when compared to CFD-predicted results. If gas flow is not modeled properly, effects of heated gas on the powder bed and part are not appropriately taken into account.

12) Convection preheating due to laser/gas relative motion has noticeable effects on cooling rates, and thus, the microstructure of Ti-6Al-4V – as demonstrated through experimentation and microscopic investigation of the grain structures. Lower cooling rates obtained when the gas flow is in the direction of the laser results in a coarsening of the prior β grain structure in Ti-6Al-4V. More distinct tracks are evidenced when the laser and gas move in similar directions.

As demonstrated through numerical simulation, the thermal history of additively manufactured parts can have noticeable effects on their microstructure. Employed scanning strategies can result in directional-dependent convection along the solidified track which can lead variations in microstructure, and ultimately, mechanical performance of the final part. For simulating the L-PBF process, the assumption of a uniform heat transfer coefficient (i.e. uniform convective flux) can lead to error in the predicted local heat transfer. For instance, the preheating accomplished by hotter argon due to upstream laser processing, is not captured when assuming a uniform convective boundary condition. Depending on the employed heat transfer coefficient, cooling rates and temperature gradients are also under- or over-estimated. Nusselt numbers are very high in areas of HAZ near the laser interaction and is direction-dependent. Thus, for simulation purposes, the convective heat transfer coefficient, should be considered as a function of gas velocity, laser scan direction and region of track (i.e. HAZ vs. non-HAZ, heating vs. cooling). The effects of convection and radiation become more prominent during the long process of building full-scale parts (many tracks and many layers); thus, these simulations can prove important when avoiding complete simulation of gas inside an L-PBF chamber.

References

[1] X. Wang, S. Xu, S. Zhou, W. Xu, M. Leary, P. Choong, M. Qian, M. Brandt, Y.M. Xie, Topological design and additive manufacturing of porous metals for bone scaffolds and orthopaedic implants: A review, Biomaterials. 83 (2016) 127–141. doi:10.1016/j.biomaterials.2016.01.012.

[2] W.E. Frazier, Metal additive manufacturing: A review, J. Mater. Eng. Perform. 23 (2014) 1917–1928. doi:10.1007/s11665-014-0958-z.

[3] S.M. Thompson, L. Bian, N. Shamsaei, A. Yadollahi, An overview of direct laser deposition for additive manufacturing; Part I: Transport phenomena, modeling and diagnostics, Addit. Manuf. 8 (2015) 36–62. doi:10.1016/j.addma.2015.07.001.

[4] N. Shamsaei, A. Yadollahi, L. Bian, S.M. Thompson, An overview of direct laser deposition for additive manufacturing; part II: mechanical behavior, process parameter optimization and control, Addit. Manuf. 8 (2015) 12–35. doi:10.1016/j.addma.2015.07.002.

[5] A. Yadollahi, N. Shamsaei, Additive manufacturing of fatigue resistant materials: challenges and opportunities, Int. J. Fatigue. 98 (2017) 14–31. doi:10.1016/j.ijfatigue.2017.01.001.

[6] C.R. Deckard, Method and apparatus for producing parts by selective sintering, (1989) US4863538 A.

[7] M. Masoomi, X. Gao, S.M. Thompson, N. Shamsaei, L. Bian, A. Elwany, Modeling, simulation and experimental validation of heat transfer during selective laser melting, in:

ASME, Houston, Texas, USA, 2015. doi:10.1115/IMECE2015-52165.

[8] E.R. Denlinger, V. Jagdale, G. V Srinivasan, T. El-Wardany, P. Michaleris, Thermal modeling of Inconel 718 processed with powder bed fusion and experimental validation using in situ measurements, Addit. Manuf. 11 (2016) 7–15. doi:10.1016/j.addma.2016.03.003.

[9] F. Verhaeghe, T. Craeghs, J. Heulens, L. Pandelaers, A pragmatic model for selective laser melting with evaporation, Acta Mater. 57 (2009) 6006–6012. doi:10.1016/j.actamat.2009.08.027.

[10] R.S. Khmyrov, S.N. Grigoriev, A.A. Okunkova, A.V. Gusarov, On the possibility of selective laser melting of quartz glass, Phys. Procedia. 56 (2014) 345–356. doi:10.1016/j.phpro.2014.08.117.

[11] S.A. Khairallah, A.T. Anderson, A. Rubenchik, W.E. King, Laser powder-bed fusion additive manufacturing: Physics of complex melt flow and formation mechanisms of pores, spatter, and denudation zones, Acta Mater. 108 (2016) 36–45. doi:10.1016/j.actamat.2016.02.014.

[12] D. Gu, P. Yuan, Thermal evolution behavior and fluid dynamics during laser additive manufacturing of Al-based nanocomposites: Underlying role of reinforcement weight fraction, J. Appl. Phys. 118 (2015) 233109. doi:10.1063/1.4937905.

[13] C. Weingarten, D. Buchbinder, N. Pirch, W. Meiners, K. Wissenbach, R. Poprawe, Formation and reduction of hydrogen porosity during selective laser melting of AlSi10Mg, J. Mater. Process. Technol. 221 (2015) 112–120. doi:10.1016/j.jmatprotec.2015.02.013.

[14] A.M. Khorasani, I. Gibson, M. Goldberg, G. Littlefair, A survey on mechanisms and critical parameters on solidification of selective laser melting during fabrication of Ti-6Al-4V

prosthetic acetabular cup, Mater. Des. 103 (2016) 348–355. doi:10.1016/j.matdes.2016.04.074.

[15] S.M. Thompson, Z.S.. Aspin, N.. Shamsaei, A.. Elwany, L. Bian, Additive manufacturing of heat exchangers: A case study on a multi-layered Ti-6Al-4V oscillating heat pipe, Submitt. to Addit. Manuf. (2015). doi:10.1016/j.addma.2015.09.003.

[16] J. Parthasarathy, B. Starly, S. Raman, A design for the additive manufacture of functionally graded porous structures with tailored mechanical properties for biomedical applications, J. Manuf. Process. 13 (2011) 160–170. doi:10.1016/J.JMAPRO.2011.01.004.

[17] N. Sudarmadji, J.Y. Tan, K.F. Leong, C.K. Chua, Y.T. Loh, Investigation of the mechanical properties and porosity relationships in selective laser-sintered polyhedral for functionally graded scaffolds, Acta Biomater. 7 (2011) 530–537. doi:10.1016/J.ACTBIO.2010.09.024.

[18] A. Emelogu, M. Marufuzzaman, S.M. Thompson, N. Shamsaei, L. Bian, Additive manufacturing of biomedical implants: A feasibility assessment via supply-chain cost analysis, Addit. Manuf. 11 (2016) 97–113. doi:10.1016/J.ADDMA.2016.04.006.

[19] I. Yadroitsev, P. Krakhmalev, I. Yadroitsava, Selective laser melting of Ti6Al4V alloy for biomedical applications: Temperature monitoring and microstructural evolution, J. Alloys Compd. 583 (2014) 404–409. doi:10.1016/j.jallcom.2013.08.183.

[20] R. Wauthle, J. van der Stok, S. Amin Yavari, J. Van Humbeeck, J.-P. Kruth, A.A. Zadpoor, H. Weinans, M. Mulier, J. Schrooten, Additively manufactured porous tantalum implants, Acta Biomater. 14 (2015) 217–225. doi:10.1016/j.actbio.2014.12.003.

[21] S. Ly, A.M. Rubenchik, S.A. Khairallah, G. Guss, M.J. Matthews, Metal vapor micro-jet controls material redistribution in laser powder bed fusion additive manufacturing, Sci. Rep. 7 (2017) 4085. doi:10.1038/s41598-017-04237-z.

[22] H. Wang, Y. Shi, S. Gong, A. Duan, Effect of assist gas flow on the gas shielding during laser deep penetration welding, J. Mater. Process. Technol. 184 (2007) 379–385. doi:10.1016/j.jmatprotec.2006.12.014.

[23] A.M. Philo, C.J. Sutcliffe, S. Sillars, J. Sienz, S.G.R. Brown, N.P. Lavery, A Study into the Effects of Gas Flow Inlet Design in a Renishaw AM250 Laser Powder Bed Fusion Machine Using Computational Modelling, Solid Free. Fabr. (2017).

[24] P. Kah, J. Martikainen, Influence of shielding gases in the welding of metals, Int. J. Adv. Manuf. Technol. 64 (2013) 1411–1421. doi:10.1007/s00170-012-4111-6.

[25] P. Mercelis, J.-P.J. Kruth, Residual stresses in selective laser sintering and selective laser melting, Rapid Prototyp. J. 12 (2006) 254–265. doi:10.1108/13552540610707013.

[26] M.F. Zaeh, G. Branner, Investigations on residual stresses and deformations in selective laser melting, Prod. Eng. 4 (2010) 35–45. doi:10.1007/s11740-009-0192-y.

[27] I. Yadroitsava, S. Grewar, D. Hattingh, I. Yadroitsev, Residual Stress in SLM Ti6Al4V Alloy Specimens, Mater. Sci. Forum. 828–829 (2015) 305–310. doi:10.4028/www.scientific.net/MSF.828-829.305.

[28] C. Li, C.H. Fu, Y.B. Guo, F.Z. Fang, A multiscale modeling approach for fast prediction of part distortion in selective laser melting, J. Mater. Process. Technol. 229 (2016) 703–712. doi:10.1016/j.jmatprotec.2015.10.022.

[29] P. Vora, K. Mumtaz, I. Todd, N. Hopkinson, AlSi12 in-situ alloy formation and residual stress reduction using anchorless selective laser melting, Addit. Manuf. 7 (2015) 12–19. doi:10.1016/j.addma.2015.06.003.

[30] P. Prabhakar, W.J. Sames, R. Dehoff, S.S. Babu, Computational modeling of residual stress formation during the electron beam melting process for Inconel 718, Addit. Manuf. 7 (2015)

83–91. doi:10.1016/j.addma.2015.03.003.

[31] L. Parry, I.A. Ashcroft, R.D. Wildman, Understanding the effect of laser scan strategy on residual stress in selective laser melting through thermo-mechanical simulation, Addit. Manuf. 12 (2016) 1–15. doi:10.1016/j.addma.2016.05.014.

[32] B. Vrancken, R. Wauthle, J. Kruth, J. Van Humbeeck, Study of the Influence of Material Properties on Residual Stress in Selective Laser Melting, Proc. 24th Int. Solid Free. Fabr. Symp. (2013) 393–407.

[33] J.C. Heigel, P. Michaleris, E.W. Reutzel, Thermo-mechanical model development and validation of directed energy deposition additive manufacturing of Ti–6Al–4V, Addit. Manuf. 5 (2015) 9–19. doi:10.1016/j.addma.2014.10.003.

[34] A. Hussein, L. Hao, C. Yan, R. Everson, Finite element simulation of the temperature and stress fields in single layers built without-support in selective laser melting, Mater. Des. 52 (2013) 638–647. doi:10.1016/j.matdes.2013.05.070.

[35] A.H. Nickel, D.M. Barnett, F.B. Prinz, Thermal stresses and deposition patterns in layered manufacturing, Mater. Sci. Eng. A. 317 (2001) 59–64. doi:10.1016/S0921-5093(01)01179-0.

[36] B. Cheng, S. Shrestha, K. Chou, Stress and deformation evaluations of scanning strategy effect in selective laser melting, Addit. Manuf. (2016). doi:10.1016/j.addma.2016.05.007.

[37] J.-P. Kruth, J. Deckers, E. Yasa, R. Wauthlé, R. Wauthle, Assessing and comparing influencing factors of residual stresses in selective laser melting using a novel analysis method, Proc. Inst. Mech. Eng. Part B J. Eng. Manuf. 226 (2012) 980–991. doi:10.1177/0954405412437085.

[38] J.P. Kruth, L. Froyen, J. Van Vaerenbergh, P. Mercelis, M. Rombouts, B. Lauwers,

Selective laser melting of iron-based powder, J. Mater. Process. Technol. 149 (2004) 616–622. doi:10.1016/j.jmatprotec.2003.11.051.

[39] L. Thijs, K. Kempen, J.-P. Kruth, J. Van Humbeeck, Fine-structured aluminium products with controllable texture by selective laser melting of pre-alloyed AlSi10Mg powder, Acta Mater. 61 (2013) 1809–1819. doi:10.1016/j.actamat.2012.11.052.

[40] Y. Lu, S. Wu, Y. Gan, T. Huang, C. Yang, L. Junjie, J. Lin, Study on the microstructure, mechanical property and residual stress of SLM Inconel-718 alloy manufactured by differing island scanning strategy, Opt. Laser Technol. 75 (2015) 197–206. doi:10.1016/j.optlastec.2015.07.009.

[41] Q. Bo, S. Yu-sheng, W. Qing-song, W. Hai-bo, The helix scan strategy applied to the selective laser melting, Int. J. Adv. Manuf. Technol. 63 (2012) 631–640. doi:10.1007/s00170-012-3922-9.

[42] M.A. Khan, R.L. Williams, D.F. Williams, The corrosion behaviour of Ti–6Al–4V, Ti–6Al–7Nb and Ti–13Nb–13Zr in protein solutions, Biomaterials. 20 (1999) 631–637. doi:10.1016/S0142-9612(98)00217-8.

[43] L. Thijs, F. Verhaeghe, T. Craeghs, J. Van Humbeeck, J.-P. Kruth, A study of the microstructural evolution during selective laser melting of Ti–6Al–4V, Acta Mater. 58 (2010) 3303–3312. doi:10.1016/j.actamat.2010.02.004.

[44] C. Qiu, C. Panwisawas, M. Ward, H.C. Basoalto, J.W. Brooks, M.M. Attallah, On the role of melt flow into the surface structure and porosity development during selective laser melting, Acta Mater. 96 (2015) 72–79. doi:10.1016/j.actamat.2015.06.004.

[45] M. Masoomi, S.M. Thompson, N. Shamsaei, Quality part production via multi-laser additive manufacturing, Manuf. Lett. 13 (2017). doi:10.1016/j.mfglet.2017.05.003.

[46] L.E. Murr, E. Martinez, J. Hernandez, S. Collins, K.N. Amato, S.M. Gaytan, P.W. Shindo, Microstructures and Properties of 17-4 PH Stainless Steel Fabricated by Selective Laser Melting, J. Mater. Res. Technol. 1 (2012) 167–177. doi:10.1016/S2238-7854(12)70029-7.

[47] T. Lebrun, K. Tanigaki, K. Horikawa, H. Kobayashi, Strain rate sensitivity and mechanical anisotropy of selective laser melted 17-4 PH stainless steel, Mech. Eng. J. 1 (2014) SMM0049–SMM0049. doi:10.1299/mej.2014smm0049.

[48] L. Facchini, N. Vicente, I. Lonardelli, E. Magalini, P. Robotti, A. Molinari, Metastable Austenite in 17-4 Precipitation-Hardening Stainless Steel Produced by Selective Laser Melting, Adv. Eng. Mater. 12 (2010) 184–188. doi:10.1002/adem.200900259.

[49] L.E.L.E. Murr, S.M.S.M. Gaytan, D.A.D. a. Ramirez, E. Martinez, J. Hernandez, K.N. Amato, P.W. Shindo, F.R. Medina, R.B. Wicker, Metal Fabrication by Additive Manufacturing Using Laser and Electron Beam Melting Technologies, J. Mater. Sci. Technol. 28 (2012) 1–14. doi:10.1016/S1005-0302(12)60016-4.

[50] A. Yadollahi, N. Shamsaei, S.M. Thompson, A. Elwany, L. Bian, N. Shamsaei, S.M. Thompson, A. Elwany, L. Bian, M.S. Thompson, A. Elwany, L. Bian, Effects of Building orientation and Heat Treatment on Fatigue Behavior of Selective Laser Melted 17-4 PH Stainless Steel, Int. J. Fatigue. 94 (2017) 218–235. doi:10.1016/j.ijfatigue.2016.03.014.

[51] M. Mahmoudi, A. Elwany, A. Yadollahi, S.M. Thompson, L. Bian, N. Shamsaei, Mechanical properties and microstructural characterization of selective laser melted 17-4 PH stainless steel, Rapid Prototyp. J. 23 (2017) 280–294. doi:10.1108/RPJ-12-2015-0192.

[52] Y. Huang, L.J. Yang, X.Z. Du, Y.P. Yang, Finite element analysis of thermal behavior of metal powder during selective laser melting, Int. J. Therm. Sci. 104 (2016) 146–157. doi:10.1016/j.ijthermalsci.2016.01.007.

[53] Y. Li, D. Gu, Parametric analysis of thermal behavior during selective laser melting additive manufacturing of aluminum alloy powder, Mater. Des. 63 (2014) 856–867. doi:10.1016/j.matdes.2014.07.006.

[54] D. Riedlbauer, M. Drexler, D. Drummer, P. Steinmann, J. Mergheim, Modelling, simulation and experimental validation of heat transfer in selective laser melting of the polymeric material PA12, Comput. Mater. Sci. 93 (2014) 239–248. doi:10.1016/j.commatsci.2014.06.046.

[55] P. Michaleris, Modeling metal deposition in heat transfer analyses of additive manufacturing processes, Finite Elem. Anal. Des. 86 (2014) 51–60. doi:10.1016/j.finel.2014.04.003.

[56] Y. Li, D. Gu, Thermal behavior during selective laser melting of commercially pure titanium powder: Numerical simulation and experimental study, Addit. Manuf. 1–4 (2014) 99–109. doi:10.1016/j.addma.2014.09.001.

[57] H.-W. Mindt, M. Megahed, N.P. Lavery, A. Giordimaina, S.G.R. Brown, Verification of numerically calculated cooling rates of powder bed additive manufacturing, in: TMS 2016 145 Th Annu. Meet. Exhib. Suppl. Proc., John Wiley & Sons, Inc., Hoboken, NJ, USA, 2016: pp. 205–212. doi:10.1002/9781119274896.ch26.

[58] L.E. Lindgren, E. Hedblom, Modelling of addition of filler material in large deformation analysis of multipass welding, Commun. Numer. Methods Eng. 17 (1999) 647–657.

[59] L.E. Lindgren, H. Runnemalm, M.O. Nasstrom, Simulation of multipass welding of a thick plate, Int. J. Numer. Methods Eng. 44 (1999) 1301–1316.

[60] L. Dong, a. Makradi, S. Ahzi, Y. Remond, Three-dimensional transient finite element analysis of the selective laser sintering process, J. Mater. Process. Technol. 209 (2009) 700–

706. doi:10.1016/j.jmatprotec.2008.02.040.

[61] T. Mukherjee, V. Manvatkar, A. De, T. DebRoy, Dimensionless numbers in additive manufacturing, J. Appl. Phys. 121 (2017) 64904. doi:10.1063/1.4976006.

[62] D.M. Keicher, W.D. Miller, Multiple beams and nozzles to increase deposition rate, US 5993554 A, 2001.

[63] J.J. Keremes, J.D. Haynes, Y. Gao, D.E. Matejczyk, Laser configuration for additive manufacturing, US 20130112672 A1, 2013.

[64] T.J. Rockstroh, D.C. Gray, M.A. Cheverton, V.P. Ostroverkhov, Selective laser melting additive manufacturing method with simultaneous multiple melting lasers beams and apparatus therefor, WO 2015191257 A1, 2015.

[65] M. Fockele, Device for manufacture of objects by layer-wise constructing from powder-form material has sub-systems of irradiating unit allocated to respective sections of building field on base arrangement, EP1839781 A3, 2006.

[66] Y. Lu, S. Wu, Y. Gan, J. Li, C. Zhao, D. Zhuo, J. Lin, Investigation on the microstructure, mechanical property and corrosion behavior of the selective laser melted CoCrW alloy for dental application, Mater. Sci. Eng. C. 49 (2015) 517–525. doi:10.1016/j.msec.2015.01.023.

[67] H. Chung, S. Das, Numerical modeling of scanning laser-induced melting, vaporization and resolidification in metals subjected to step heat flux input, Int. J. Heat Mass Transf. 47 (2004) 4153–4164. doi:10.1016/j.ijheatmasstransfer.2004.05.003.

[68] M. Badrossamay, T.H.C. Childs, Further studies in selective laser melting of stainless and tool steel powders, Int. J. Mach. Tools Manuf. 47 (2007) 779–784. doi:10.1016/j.ijmachtools.2006.09.013.

[69] R. Paul, S. Anand, F. Gerner, Effect of thermal deformation on part errors in metal powder based additive manufacturing processes, J. Manuf. Sci. Eng. 136 (2014) 31009. doi:10.1115/1.4026524.

[70] P. Peyre, P. Aubry, R. Fabbro, R. Neveu, A. Longuet, Analytical and numerical modelling of the direct metal deposition laser process, J. Phys. D. Appl. Phys. 41 (2008) 25403. doi:10.1088/0022-3727/41/2/025403.

[71] F. a. España, V.K. Balla, A. Bandyopadhyay, Laser surface modification of AISI 410 stainless steel with brass for enhanced thermal properties, Surf. Coatings Technol. 204 (2010) 2510–2517. doi:10.1016/j.surfcoat.2010.01.029.

[72] S. Zekovic, R. Dwivedi, R. Kovacevic, Thermo-structural finite element analysis of direct laser metal deposited thin-walled structures, in: Proc. Solid Free. Fabr. Symp., University of Texas at Austin (freeform), Austin, TX, 2005: pp. 338–355.

[73] S. Bannour, K. Abderrazak, H. Mhiri, G. Le Palec, Effects of temperature-dependent material properties and shielding gas on molten pool formation during continuous laser welding of AZ91 magnesium alloy, Opt. Laser Technol. 44 (2012) 2459–2468. doi:10.1016/j.optlastec.2012.03.034.

[74] R. Martukanitz, P. Michaleris, T. Palmer, T. DebRoy, Z.-K. Liu, R. Otis, T.W. Heo, L.-Q. Chen, Toward an integrated computational system for describing the additive manufacturing process for metallic materials, Addit. Manuf. 1–4 (2014) 52–63. doi:10.1016/J.ADDMA.2014.09.002.

[75] T.M. Rodgers, J.D. Madison, V. Tikare, M.C. Maguire, Predicting Mesoscale Microstructural Evolution in Electron Beam Welding, JOM. 68 (2016) 1419–1426. doi:10.1007/s11837-016-1863-8.

[76] T.P. Moran, P. Li, D.H. Warner, N. Phan, Utility of Superposition-Based Finite Element Approach for Part-Scale Thermal Simulation in Additive Manufacturing, Addit. Manuf. (2018). doi:10.1016/j.addma.2018.02.015.

[77] A. V Gusarov, I. Yadroitsev, P. Bertrand, I. Smurov, Model of Radiation and Heat Transfer in Laser - Powder Interaction Zone at Selective Laser Melting, 131 (7) (2009). doi:10.1115/1.3109245.

[78] Y. Xiong, W.H. Hofmeister, Z. Cheng, J.E. Smugeresky, E.J. Lavernia, J.M. Schoenung, In situ thermal imaging and three-dimensional finite element modeling of tungsten carbide–cobalt during laser deposition, Acta Mater. 57 (2009) 5419–5429. doi:10.1016/j.actamat.2009.07.038.

[79] R. Ye, J.E. Smugeresky, B. Zheng, Y. Zhou, E.J. Lavernia, Numerical modeling of the thermal behavior during the LENS process, Mater. Sci. Eng. A. 428 (2006) 47–53. doi:10.1016/j.msea.2006.04.079.

[80] M.L. Griffith, M.E. Schlienger, L.D. Harwell, M.S. Oliver, M.D. Baldwin, M.T. Ensz, M. Essien, J. Brooks, C. V Robino, J.E. Smugeresky, W.H. Hofmeister, M.J. Wert, D. V Nelson, Understanding thermal behavior in the LENS process, Mater. Des. 20 (1999) 107–113. doi:10.1016/S0261-3069(99)00016-3.

[81] I. V Shishkovsky, V.I. Scherbakov, Y.G. Morozov, M. V Kuznetsov, I.P. Parkin, Surface laser sintering of exothermic powder compositions: A thermal and SEM/EDX study., 91 (2008) 427–436. doi:DOI 10.1007/s10973-007-8353-8.

[82] C.M. Taylor, Direct laser sintering of stainless steel : thermal experiments and numerical modelling, (2004). http://etheses.whiterose.ac.uk/378/.

[83] K. Zeng, D. Pal, H.J. Gong, N. Patil, B. Stucker, Comparison of 3DSIM thermal modelling

of selective laser melting using new dynamic meshing method to ANSYS, Mater. Sci. Technol. 31 (2015) 945–956. doi:10.1179/1743284714Y.0000000703.

[84] N. Guo, M.C. Leu, Additive manufacturing: technology, applications and research needs, Front. Mech. Eng. 8 (2013) 215–243. doi:10.1007/s11465-013-0248-8.

[85] T.D. Ngo, A. Kashani, G. Imbalzano, K.T.Q. Nguyen, D. Hui, Additive manufacturing (3D printing): A review of materials, methods, applications and challenges, Compos. Part B Eng. 143 (2018) 172–196. doi:10.1016/J.COMPOSITESB.2018.02.012.

[86] A. Wiesner, D. Schwarze, Multi-Laser selective laser melting, in: 8th Int. Conf. Photonic Technol., Fürth, Germany, 2014.

[87] N.F. Williams, Endoprosthesis having multiple laser welded junctions method and procedure, (1998).

[88] Y. Hu, W.F. Hehmann, Multi-laser beam welding high strength superalloys, US 6972390 B2, 2005.

[89] J.A. Benda, A. Parasco, Apparatus for multiple beam laser sintering, (1996).

[90] I. Gurrappa, Characterization of titanium alloy Ti-6Al-4V for chemical, marine and industrial applications, Mater. Charact. 51 (2003) 131–139. doi:10.1016/j.matchar.2003.10.006.

[91] L.E. Murr, S.A. Quinones, S.M. Gaytan, M.I. Lopez, A. Rodela, E.Y. Martinez, D.H. Hernandez, E. Martinez, F. Medina, R.B. Wicker, Microstructure and mechanical behavior of Ti-6Al-4V produced by rapid-layer manufacturing, for biomedical applications., J. Mech. Behav. Biomed. Mater. 2 (2009) 20–32. doi:10.1016/j.jmbbm.2008.05.004.

[92] S.S. Al-Bermani, M.L. Blackmore, W. Zhang, I. Todd, The origin of microstructural diversity, texture, and mechanical properties in electron beam melted Ti-6Al-4V, Metall.

Mater. Trans. A. 41 (2010) 3422–3434. doi:10.1007/s11661-010-0397-x.

[93] Saad A. Khairallah Andrew T. Anderson Alexander Rubenchik, Laser powder-bed fusion additive manufacturing: physics of complex melt flow and formation mechanisms of pores, spatter and denudation zone Saad, Igarss 2014. 108 (2014) 1–5. doi:10.1007/s13398-014-0173-7.2.

[94] B. Valsecchi, B. Previtali, E. Gariboldi, A. Liu, Characterisation of the thermal damage in a martensitic steel substrate consequent to laser cladding process, Procedia Eng. 10 (2011) 2851–2856. doi:10.1016/j.proeng.2011.04.474.

[95] C.M. Taylor, P.T.H.C. Childs, Thermal experiments in direct metal laser sintering, in: Proc. Euro RP, 2001.

[96] Bert Huis in 't Veld, L. Overmeyer, M. Schmidt, K. Wegener, A. Malshe, P. Bartolo, Micro additive manufacturing using ultra short laser pulses, CIRP Ann. - Manuf. Technol. 64 (2015) 701–724. doi:10.1016/j.cirp.2015.05.007.

[97] S.M. Thompson, H.B. Ma, Thermal spreading analysis of rectangular heat spreader, J. Heat Transfer. 136 (2014) 64503. doi:10.1115/1.4026558.

[98] S.S. Sih, J.W. Barlow, S. Sumin Sih, J.W. Barlow, S.S. Sih, J.W. Barlow, S. Sumin Sih, J.W. Barlow, The prediction of the emissivity and thermal conductivity of powder beds, Part. Sci. Technol. 22 (2004) 291–304. doi:10.1080/02726350490501682a.

[99] Y.P. Lei, H. Murakawa, Y.W. Shi, X.Y. Li, Numerical analysis of the competitive influence of Marangoni flow and evaporation on heat surface temperature and molten pool shape in laser surface remelting, Comput. Mater. Sci. 21 (2001) 276–290. doi:10.1016/S0927-0256(01)00143-4.

[100] H. Yin, S.D. Felicelli, L. Wang, Fluid flow, heat and mass transfer in the molten pool of the

LENS process, in: TMS Annu. Meet., New Orleans, 2008: pp. 261–270.

[101] M. Darbouli, C. Métivier, J.-M. Piau, A. Magnin, A. Abdelali, Rayleigh-Bénard convection for viscoplastic fluids, Phys. Fluids. 25 (2013) 23101. doi:10.1063/1.4790521.

[102] B.A. Younglove, Thermophysical properties of fluids. I. Argon, ethylene, parahydrogen, nitrogen, nitrogen trifluoride, and oxygen, 1982.

[103] A. Neira Arce, Thermal modeling and simulation of electron beam melting for rapid prototyping on Ti6Al4V alloys, North Carolina State University, 2012.

[104] A. Neale, D. Derome, B. Blocken, J. Carmeliet, Determination of surface convective heat transfer coefficients by CFD, in: 11th Can. Conf. Build. Sci. Technol., Banff, Alberta, 2007.

[105] O. Turgut, N. Onur, An experimental and three-dimensional numerical study of natural convection heat transfer between two horizontal parallel plates, Int. Commun. Heat Mass Transf. 34 (2007) 644–652. doi:10.1016/j.icheatmasstransfer.2007.02.001.

[106] L.E. Criales, Y.M. Arısoy, B. Lane, S. Moylan, A. Donmez, T. Özel, Laser powder bed fusion of nickel alloy 625: Experimental investigations of effects of process parameters on melt pool size and shape with spatter analysis, Int. J. Mach. Tools Manuf. 121 (2017) 22–36. doi:10.1016/J.IJMACHTOOLS.2017.03.004.

[107] Y.S. Lee, W. Zhang, Modeling of heat transfer, fluid flow and solidification microstructure of nickel-base superalloy fabricated by laser powder bed fusion, Addit. Manuf. 12 (2016) 178–188. doi:10.1016/J.ADDMA.2016.05.003.

[108] IAEA, Thermophysical Properties of Materials for Nuclear Engineering: A Tutorial and Collection of Data, 2008. doi:http://dx.doi.org/10.1002/cbdv.200490137.

[109] N.K. Tolochko, T. Laoui, Y. V Khlopkov, S.E. Mozzharov, V.I. Titov, M.B. Ignatiev, Absorptance of powder materials suitable for laser sintering, Rapid Prototyp. J. 6 (2000)

155–160. doi:Doi 10.1108/13552540010337029.

[110] P. Fischer, V. Romano, H.P. Weber, N.P. Karapatis, E. Boillat, R. Glardon, Sintering of commercially pure titanium powder with a Nd:YAG laser source, Acta Mater. 51 (2003) 1651–1662. doi:10.1016/S1359-6454(02)00567-0.

[111] M. Boivineau, C. Cagran, D. Doytier, V. Eyraud, M.H. Nadal, B. Wilthan, G. Pottlacher, Thermophysical properties of solid and liquid Ti-6Al-4V (TA6V) alloy, Int. J. Thermophys. 27 (2006) 507–529. doi:10.1007/s10765-005-0001-6.

[112] Y. Zhong, L. Liu, S. Wikman, D. Cui, Z. Shen, Intragranular cellular segregation network structure strengthening 316L stainless steel prepared by selective laser melting, J. Nucl. Mater. 470 (2016) 170–178. doi:10.1016/j.jnucmat.2015.12.034.

[113] T. Vilaro, C. Colin, J.D. Bartout, As-fabricated and heat-treated microstructures of the Ti-6Al-4V alloy processed by selective laser melting, Metall. Mater. Trans. A. 42 (2011) 3190–3199. doi:10.1007/s11661-011-0731-y.

[114] W.E. King, A.T. Anderson, R.M. Ferencz, N.E. Hodge, C. Kamath, S.A. Khairallah, A.M. Rubenchik, Laser powder bed fusion additive manufacturing of metals; physics, computational, and materials challenges, Appl. Phys. Rev. 2 (2015) 41304. doi:10.1063/1.4937809.

[115] G. Kasperovich, J. Haubrich, J. Gussone, G. Requena, Correlation between porosity and processing parameters in TiAl6V4 produced by selective laser melting, Mater. Des. 105 (2016) 160–170. doi:10.1016/j.matdes.2016.05.070.

[116] M. Khanzadehdaghalian, L. Bian, N. Shamsaei, S.M. Thompson, Porosity Detection of Laser Based Additive Manufacturing Using Melt Pool Morphology Clustering, in: Solid Free. Fabr. 2016 Proc. 26th Annu. Int., Austin, 2016: pp. 1487–1494.

[117] C.Y. Ho, M.Y. Wen, Distribution of the intensity absorbed by the keyhole wall in laser processing, J. Mater. Process. Technol. 145 (2004) 303–310. doi:10.1016/j.jmatprotec.2003.07.009.

[118] A.J. Sterling, B. Torries, N. Shamsaei, S.M. Thompson, D.W. Seely, Fatigue behavior and failure mechanisms of direct laser deposited Ti-6Al-4V, Mater. Sci. Eng. A. 655 (2016) 100–112. doi:10.1016/j.msea.2015.12.026.

[119] B. Torries, A.J. Sterling, N. Shamsaei, S.M. Thompson, S.R. Daniewicz, Utilization of a Microstructure Sensitive Fatigue Model for Additively Manufactured Ti-6Al-4V, Rapid Prototyp. (2016). doi:10.1108/RPJ-11-2015-0168.

[120] B. Torries, S. Shao, N. Shamsaei, S.M. Thompson, Effect of Inter-Layer Time Interval on the Mechanical Behavior of Direct Laser Deposited Ti-6Al-4V, in: Solid Free. Fabr. 2016 Proc. 26th Annu. Int., Austin, 2016: pp. 175–184.

[121] H. Galarraga, D.A. Lados, R.R. Dehoff, M.M. Kirka, P. Nandwana, Effects of the microstructure and porosity on properties of Ti-6Al-4V ELI alloy fabricated by electron beam melting (EBM), Addit. Manuf. 10 (2016) 47–57. doi:10.1016/j.addma.2016.02.003.

[122] W. Xu, E.W. Lui, A. Pateras, M. Qian, M. Brandt, In situ tailoring microstructure in additively manufactured Ti-6Al-4V for superior mechanical performance, Acta Mater. 125 (2017) 390–400. doi:10.1016/j.actamat.2016.12.027.

[123] B. Song, S. Dong, B. Zhang, H. Liao, C. Coddet, Effects of processing parameters on microstructure and mechanical property of selective laser melted Ti6Al4V, Mater. Des. 35 (2012) 120–125. doi:10.1016/j.matdes.2011.09.051.

[124] S.M. Kelly, S.L. Kampe, Microstructural evolution in laser-deposited multilayer Ti-6Al-4V builds: Part II. Thermal modeling, Metall. Mater. Trans. A. 35 (2004) 1861–1867.

doi:10.1007/s11661-004-0094-8.

[125] P. Edwards, M. Ramulu, Fatigue performance evaluation of selective laser melted Ti-6Al-4V, Mater. Sci. Eng. A. 598 (2014) 327–337. doi:10.1016/j.msea.2014.01.041.

[126] J. Gockel, J. Beuth, K. Taminger, Integrated control of solidification microstructure and melt pool dimensions in electron beam wire feed additive manufacturing of Ti-6Al-4V, Addit. Manuf. 1–4 (2014) 119–126. doi:10.1016/J.ADDMA.2014.09.004.

[127] A.J. Dunbar, E.R. Denlinger, M.F. Gouge, T.W. Simpson, P. Michaleris, Comparisons of laser powder bed fusion additive manufacturing builds through experimental in situ distortion and temperature measurements, Addit. Manuf. 15 (2017) 57–65. doi:10.1016/J.ADDMA.2017.03.003.

[128] A.M. Aboutaleb, L. Bian, A. Elwany, N. Shamsaei, S.M. Thompson, G. Tapia, Accelerated process optimization for laser-based additive manufacturing by leveraging similar prior studies, IISE Trans. 49 (2017) 31–44. doi:10.1080/0740817X.2016.1189629.

[129] A.S.M. Handbook, Heat treating, vol. 4, ASM Int. Mater. Park. OH. (1991).

[130] T. Gnäupel-Herold, A. Creuziger, Diffraction study of the retained austenite content in TRIP steels, Mater. Sci. Eng. A. 528 (2011) 3594–3600. doi:10.1016/j.msea.2011.01.030.

[131] P.J. Withers, H.K.D.H. Bhadeshia, Residual stress. Part 1 – Measurement techniques, Mater. Sci. Technol. 17 (2001) 355–365. doi:10.1179/026708301101509980.

[132] A.J. Allen, M.T. Hutchings, C.G. Windsor, C. Andreani, Neutron diffraction methods for the study of residual stress fields, Adv. Phys. 34 (1985) 445–473. doi:10.1080/00018738500101791.

[133] T. Gnäupel-Herold, IUCr, R.A. D., W. H.-R., ISODEC: software for calculating diffraction elastic constants, J. Appl. Crystallogr. 45 (2012) 573–574.

doi:10.1107/S0021889812014252.

[134] P.J. Withers, M. Preuss, A. Steuwer, J.W.L. Pang, W.P. J., W.P. J., Methods for obtaining the strain-free lattice parameter when using diffraction to determine residual stress, J. Appl. Crystallogr. 40 (2007) 891–904. doi:10.1107/S0021889807030269.

[135] J. Yang, H. Yu, J. Yin, M. Gao, Z. Wang, X. Zeng, Formation and control of martensite in Ti-6Al-4V alloy produced by selective laser melting, Mater. Des. 108 (2016) 308–318. doi:10.1016/J.MATDES.2016.06.117.

[136] B.E. Carroll, T.A. Palmer, A.M. Beese, Anisotropic tensile behavior of Ti–6Al–4V components fabricated with directed energy deposition additive manufacturing, Acta Mater. 87 (2015) 309–320. doi:10.1016/J.ACTAMAT.2014.12.054.

[137] B. Baufeld, O. Van der Biest, R. Gault, Additive manufacturing of Ti–6Al–4V components by shaped metal deposition: Microstructure and mechanical properties, Mater. Des. 31 (2010) S106–S111. doi:10.1016/J.MATDES.2009.11.032.

[138] W. Xu, M. Brandt, S. Sun, J. Elambasseril, Q. Liu, K. Latham, K. Xia, M. Qian, Additive manufacturing of strong and ductile Ti–6Al–4V by selective laser melting via in situ martensite decomposition, Acta Mater. 85 (2015) 74–84. doi:10.1016/J.ACTAMAT.2014.11.028.

[139] H. Ali, L. Ma, H. Ghadbeigi, K. Mumtaz, In-situ residual stress reduction, martensitic decomposition and mechanical properties enhancement through high temperature powder bed pre-heating of Selective Laser Melted Ti6Al4V, Mater. Sci. Eng. A. 695 (2017) 211–220. doi:10.1016/J.MSEA.2017.04.033.

[140] O. Fergani, F. Berto, T. Welo, S.Y. Liang, Analytical modelling of residual stress in additive manufacturing, Fatigue Fract. Eng. Mater. Struct. 40 (2017) 971–978.

doi:10.1111/ffe.12560.

Appendices

Table A1 - Maximum cooling rates (with average and standard deviation) at locations P1-P16 following scan patterns described per S1-S13 during fabrication of first layer; units in 10^6 °C/s

	S1	**S2**	**S3**	**S4**	**S5**	**S6**	**S7**	**S8**	**S9**	**S10**	**S11**	**S12**	**S13**
Point 1	6.39	5.94	5.91	5.49	5.13	5.55	5.28	5.31	4.53	4.26	5.91	5.52	4.53
Point 2	6.33	5.61	5.46	5.01	5.01	5.55	4.98	4.83	4.05	4.23	5.61	4.89	4.17
Point 3	6.33	5.55	5.61	5.31	4.95	5.49	5.22	5.31	4.44	4.14	5.13	4.98	4.41
Point 4	6.24	5.46	5.52	5.19	4.77	5.43	5.01	4.98	4.11	4.08	4.95	4.74	4.11
Point 5	6.30	5.49	5.43	5.13	5.07	5.91	5.43	5.46	4.77	4.35	5.49	5.16	4.05
Point 6	6.18	5.31	5.13	4.92	5.07	5.58	5.22	5.13	4.29	4.29	5.31	4.71	4.44
Point 7	6.15	5.46	5.31	5.04	4.92	5.52	5.34	5.49	4.59	4.26	5.25	5.13	4.11
Point 8	6.15	5.25	5.19	4.95	4.83	5.52	5.16	5.13	4.59	4.17	5.19	5.07	4.38
Point 9	6.12	5.73	5.52	5.52	5.07	6.03	5.13	4.89	4.59	4.44	5.61	5.31	4.56
Point 10	6.03	5.61	5.37	4.83	4.89	5.64	5.01	4.71	3.96	4.53	5.52	5.61	4.08
Point 11	6.00	5.61	5.49	5.40	4.83	5.61	5.28	4.92	4.29	4.35	5.19	5.13	4.41
Point 12	6.00	5.49	5.31	5.13	4.89	5.61	4.89	4.86	3.93	4.38	4.98	5.01	4.17
Point 13	6.21	5.52	5.31	5.01	5.01	6.06	5.40	5.43	4.68	4.59	5.49	4.89	4.05
Point 14	6.21	5.28	5.19	4.89	5.07	5.79	5.13	5.28	4.53	4.53	5.31	5.13	4.38
Point 15	6.15	5.4	5.37	5.07	4.98	5.73	5.37	5.49	4.41	4.5	5.28	4.98	4.14
Point 16	6.06	5.19	5.04	4.98	5.01	5.64	5.04	5.01	4.17	4.47	5.13	4.98	4.35
Average	6.18	5.49	5.38	5.12	4.97	5.67	5.18	5.14	4.37	4.35	5.33	5.08	4.27
Standard deviation	0.12	0.19	0.21	0.21	0.11	0.19	0.16	0.26	0.26	0.15	0.26	0.25	0.18

Table A2 - Maximum cooling rates (with average and standard deviation) at locations P1-P16 following scan patterns described per S1-S13 during fabrication of second layer; units in 10^6 °C/s

	S1	**S2**	**S3**	**S4**	**S5**	**S6**	**S7**	**S8**	**S9**	**S10**	**S11**	**S12**	**S13**
Point 1	1.08	1.05	1.05	0.94	0.87	0.96	0.88	0.89	0.75	0.66	1.08	0.93	0.72
Point 2	0.93	0.95	0.91	0.85	0.86	0.99	0.71	0.89	0.65	0.65	0.96	0.85	0.69
Point 3	1.07	0.93	0.94	0.86	0.82	0.94	0.84	0.89	0.71	0.65	0.84	0.86	0.71
Point 4	1.07	0.92	0.95	0.93	0.89	0.86	0.85	0.86	0.69	0.61	0.85	0.77	0.62
Point 5	1.08	0.94	0.86	0.86	0.84	1.05	0.86	0.99	0.74	0.78	0.94	0.81	0.68
Point 6	1.09	0.89	0.85	0.86	0.84	0.93	0.84	0.84	0.67	0.66	0.89	0.77	0.78
Point 7	1.07	0.97	0.86	0.86	0.82	0.95	0.87	0.94	0.79	0.66	0.85	0.84	0.62
Point 8	1.07	0.86	0.93	0.77	0.71	0.94	0.89	0.84	0.75	0.65	0.88	0.84	0.74
Point 9	1.07	0.99	0.95	0.95	0.84	1.00	0.85	0.71	0.79	0.71	0.91	0.89	0.78
Point 10	1.05	0.93	0.81	0.74	0.82	0.98	0.85	0.71	0.64	0.75	0.91	0.95	0.64
Point 11	1.05	0.91	0.94	0.85	0.74	0.94	0.82	0.89	0.69	0.71	0.88	0.85	0.71
Point 12	1.02	0.94	0.86	0.85	0.86	0.92	0.82	0.85	0.63	0.77	0.86	0.83	0.69
Point 13	1.08	0.93	0.86	0.85	0.85	1.02	0.85	0.10	0.71	0.75	0.94	0.85	0.65
Point 14	1.08	0.89	0.93	0.82	0.86	0.95	0.85	0.82	0.75	0.75	0.89	0.84	0.74
Point 15	0.93	0.91	0.81	0.84	0.89	0.97	0.81	0.85	0.75	0.75	0.82	0.86	0.69
Point 16	0.93	0.89	0.86	0.89	0.86	0.98	0.86	0.83	0.65	0.78	0.85	0.86	0.75
Average	1.04	0.93	0.90	0.86	0.83	0.96	0.84	0.81	0.71	0.70	0.90	0.85	0.70
Standard deviation	0.06	0.05	0.06	0.06	0.05	0.04	0.04	0.20	0.05	0.06	0.06	0.05	0.05

Table A3 - Maximum temperature gradient magnitudes (with average and standard deviation) at locations P1-P16 following scan patterns described per S1-S13 during fabrication of first layer; units in °C/μm

	S1	**S2**	**S3**	**S4**	**S5**	**S6**	**S7**	**S8**	**S9**	**S10**	**S11**	**S12**	**S13**
Point 1	103.9	98.1	100.5	94.3	93.4	95.2	91.2	90.5	88.5	83.4	100.6	93.8	83.3
Point 2	103.9	96.5	93.9	87.1	91.2	95.2	86.7	84.5	81.7	79.9	96.2	85.3	78.6
Point 3	104.0	95.2	95.5	91.6	90.3	94.3	90.3	91.5	87.6	78.6	88.5	86.7	83.1
Point 4	102.8	93.9	94.8	89.8	87.1	93.4	87.2	86.7	82.6	77.7	86.5	83.1	77.7
Point 5	103.3	95.3	93.5	88.9	92.1	96.6	93.5	93.9	92.5	81.7	94.5	89.4	76.3
Point 6	102.1	92.5	88.5	85.8	91.1	95.7	90.3	88.5	85.3	80.8	91.5	82.6	83.5
Point 7	101.2	94.9	90.5	87.6	89.8	94.8	92.1	94.5	89.8	80.4	90.7	88.9	77.7
Point 8	101.7	91.5	89.9	86.2	88.5	94.8	89.4	88.5	89.8	79.5	89.8	88.0	82.6
Point 9	101.1	97.0	94.8	94.8	92.5	98.5	88.5	85.5	89.8	83.1	96.1	91.6	85.8
Point 10	100.3	95.5	92.5	85.5	89.8	93.6	87.1	82.6	80.4	84.4	94.8	96.1	76.8
Point 11	100.4	96.1	94.5	91.2	88.0	93.2	91.2	85.8	85.3	81.7	89.8	88.9	83.1
Point 12	100.5	94.5	92.0	88.9	88.9	93.2	85.5	84.9	79.9	82.2	86.7	87.1	78.6
Point 13	101.1	94.8	91.5	87.1	91.6	99.9	93.0	93.4	91.2	85.3	94.5	85.3	76.3
Point 14	101.1	91.2	89.8	85.3	92.1	95.9	88.9	91.2	88.9	84.4	91.5	88.9	82.6
Point 15	101.2	93.0	91.5	88.0	90.7	95.0	92.5	94.3	87.1	83.3	91.2	86.7	78.1
Point 16	99.9	89.5	87.6	86.7	88.9	93.6	87.6	87.1	83.5	83.5	88.9	86.7	81.7
Average	101.8	94.3	92.6	88.7	90.4	95.2	89.7	88.9	86.5	81.9	92.0	88.1	80.4
Standard deviation	1.38	2.29	3.17	2.97	1.78	1.88	2.45	3.87	3.94	2.22	3.84	3.56	3.12

Table A4 - Maximum temperature gradient magnitudes (with average and standard deviation) at locations P1-P16 following scan patterns described per S1-S13 during fabrication of second layer; units in °C/μm

	S1	**S2**	**S3**	**S4**	**S5**	**S6**	**S7**	**S8**	**S9**	**S10**	**S11**	**S12**	**S13**
Point 1	29.5	28.3	28.0	26.5	24.7	26.8	24.4	25.6	24.3	20.1	28.6	27.1	21.3
Point 2	29.6	26.5	26.1	23.8	24.4	26.5	22.8	23.5	22.0	20.5	26.5	23.5	19.6
Point 3	29.4	26.5	26.5	25.0	24.9	26.5	24.7	25.0	23.2	21.0	25.0	23.7	20.7
Point 4	29.1	26.1	27.1	25.2	23.5	24.7	23.5	23.7	22.0	19.9	23.5	22.6	19.3
Point 5	30.1	25.8	25.6	25.3	25.5	28.6	25.0	26.1	25.2	21.0	26.5	25.3	19.0
Point 6	28.8	25.0	25.0	24.1	25.2	26.7	24.9	25.5	23.5	20.8	25.0	22.0	20.8
Point 7	28.5	26.1	25.5	23.2	25.0	27.1	25.5	26.5	25.0	20.1	25.0	24.3	19.3
Point 8	28.5	25.5	25.0	23.5	24.1	25.9	25.3	25.5	24.6	20.5	25.0	23.8	20.7
Point 9	28.6	26.8	27.1	27.1	25.3	27.7	25.0	23.5	25.3	21.4	26.5	25.0	21.4
Point 10	28.2	26.5	25.0	23.4	25.0	26.5	23.5	22.0	22.4	22.4	27.1	26.4	19.5
Point 11	28.0	25.8	26.5	25.0	23.5	26.5	24.4	24.1	23.6	20.3	25.0	25.4	20.7
Point 12	28.5	26.5	25.6	25.0	24.3	27.1	23.5	23.1	21.7	21.1	22.8	23.8	19.6
Point 13	29.5	27.1	25.0	23.6	25.0	27.6	25.5	25.2	24.4	22.9	25.9	23.5	19.5
Point 14	28.9	24.3	25.0	23.7	25.5	26.5	25.0	24.4	24.3	22.7	25.5	25.8	20.7
Point 15	28.5	25.5	25.5	23.6	24.9	26.5	25.0	26.5	23.5	21.7	24.4	23.7	19.5
Point 16	28.3	25.0	23.2	23.7	25.7	26.2	23.2	23.5	22.8	22.9	25.5	23.7	20.4
Average	28.9	26.1	25.7	24.5	24.8	26.7	24.4	24.6	23.6	21.2	25.5	24.4	20.1
Standard deviation	0.59	0.95	1.14	1.16	0.66	0.85	0.87	1.33	1.18	1.03	1.39	1.37	0.78